UNIVERSITÀ DEGLI STUDI DI PADOVA

SCUOLA DI MEDICINA E CHIRURGIA
Corso di Laurea Magistrale in Medicina e Chirurgia

Dipartimento di Scienze Cardiache, Toraciche, Vascolari e Sanità Pubblica
Direttore: *Ch.mo Prof. Federico Rea*

U.O.C. Cardiochirurgia Pediatrica e Cardiopatie Congenite
Direttore: *Ch.mo Prof. Vladimiro Vida*

TESI DI LAUREA

3D PRINTING OF CARDIAC VALVES FROM MULTIMODAL IMAGING FOR SIMULATION AND PLANNING OF CARDIAC SURGERY PROCEDURES

Relatore: Ch.mo Prof. Vladimiro Vida

Correlatore: Dr. Alvise Guariento

Laureando: Fabio Gaccione

Anno Accademico 2023-2024

TABLE OF CONTENTS

ABSTRACT

Background. More than 250,000 artificial heart valves are implanted worldwide each year. In industrialized countries, the prevalence of valvular heart disease is estimated at 2.5%. The prevalence of valvular heart disease increases significantly after the age of 65, particularly aortic stenosis and mitral regurgitation, which account for 75% of valvular heart disease cases. In developing countries, however, rheumatic heart disease remains the leading cause of valvular heart disease.

Purpose. The aims of the study were: (A) to create aortic valve models with characteristics as similar as possible to real aortic valves; (B) to create a stenotic aortic valve model to allow young surgeons to familiarize themselves with surgical interventions involving this valve. Given the high prevalence of valve replacement surgeries in the population, young cardiac surgeons will be faced with valve replacement surgeries from the beginning of their career, for this reason it is essential that they are well prepared to perform this type of procedure and a textbook alone is certainly not enough. Furthermore, a model that presents a consistency similar to that of the real valve allows for better preoperative planning, allowing more experienced surgeons to test in advance an innovative procedure with results that, with a good approximation, reflect those that should be obtained in vivo.

Materials and methods. We created several 3D digital models of aortic valves using CT images from different patients to standardize the anatomy as much as possible. We processed and printed several 3D models of aortic valve using various resins and, finally, we used an innovative technique to create the first 3D silicone model of the University of Padua.

Results. We successfully built the models and used them during internal exercises involving specialists, receiving very positive feedback about the quality of the models. In addition, we also received extremely positive feedback from pediatric cardiac surgeons from all over the world during the Hands-On in Pediatric and Congenital Cardiac Surgery (3D Simulation) held during the World Summit for Pediatric and Congenital Heart Surgery 2024. The models will also be presented at

the 38th EACTS (European Association for Cardio-Thoracic Surgery) Annual Congress in Lisbon, Portugal, from 09/10/2024 to 12/10/2024.

Conclusions. In conclusion, we believe that 3D technology-based educational tools, such as heart valve models, can facilitate learning and skill development in young surgeons and improve the general understanding of anatomical anomalies even in more experienced surgeons. Furthermore, we believe that increasingly realistic models can significantly contribute to reducing potential intraoperative errors, allowing very complex procedures to be tested in advance in order to analyze their possible critical points.

RIASSUNTO

Presupposti dello studio: Ogni anno vengono impiantate più di 250.000 valvole cardiache artificiali in tutto il mondo. Nei paesi industrializzati, la prevalenza della malattia valvolare cardiaca è stimata al 2,5%. La prevalenza della malattia valvolare aumenta notevolmente dopo i 65 anni, in particolare per quanto riguarda la stenosi aortica e l'insufficienza mitralica, che rappresentano il 75% dei casi di malattia valvolare. Nei paesi in via di sviluppo, invece, la malattia cardiaca reumatica rimane la causa principale di malattia valvolare.

Scopo. Gli obiettivo dello studio erano: (A) creare modelli di valvole aortiche con caratteristiche quanto più simili alle valvole aortiche reali; (B) creare un modello di valvola aortica stenotica al fine di permettere ai giovani chirurghi di prendere confidenza con gli interventi chirurgici che riguardano questa valvola. Data l'alta prevalenza nella popolazione degli interventi di sostituzione valvolare, i giovani cardiochirurghi si troveranno ad affrontare interventi di sostituzione valvolare fin dall'inizio della loro carriera, per questo motivo, è essenziale che siano ben preparati ad eseguire questo tipo di procedure ed un libro di testo da solo non è certamente sufficiente. Inoltre, un modello che presenta una consistenza simile a quella della valvola reale permette di migliorare la pianificazione preoperatoria, consentendo ai chirurghi più esperti di testare in anteprima procedure innovative con risultati che, con buona approssimazione, rispecchiano quelli che si avrebbero in vivo.

Materiali e Metodi. Abbiamo creato diversi modelli digitali 3D di valvole aortiche utilizzando immagini TC provenienti da diversi pazienti per standardizzare quanto possibile l'anatomia. Abbiamo processato e stampato diversi modelli 3D di valvola aortica utilizzando varie resine e, infine, abbiamo utilizzato una tecnica innovativa per creare il primo modello 3D in silicone dell'Università degli Studi di Padova.

Risultati. Abbiamo costruito con successo i modelli e li abbiamo utilizzati durante le esercitazioni interne che vedono coinvolti gli specializzandi, ricevendo feedback molto positivi circa la qualità dei modelli. Inoltre, abbiamo anche ricevuto feedback estremamente positivi da cardiochirurghi pediatrici proveniente da tutto il mondo durante l'Hands-On in Pediatric And Congenital Cardiac Surgery (3D Simulation) che si è tenuto durante il World Summit for Pediatric and Congenital Heart Surgery

2024. I modelli saranno presentati anche al 38° Congresso Annuale della EACTS (European Association for Cardio-Thoracic Surgery) in programma a Lisbona, Portogallo, dal 09/10/2024 al 12/10/2024.

Conclusioni. In conclusione, crediamo che gli strumenti didattici basati sulla tecnologia 3D, come ad esempio i modelli di valvole cardiache, possano agevolare l'apprendimento e lo sviluppo delle competenze nei giovani chirurghi e migliorare la comprensione generale delle anomalie anatomiche anche nei chirurghi più esperti. Inoltre, crediamo che modelli sempre più realistici possano contribuire significativamente a ridurre potenziali errori intraoperatori, permettendo di testare in anteprima procedure molto complesse al fine di analizzarne i possibili punti critici.

I. INTRODUCTION

1. Anatomy of the heart

1.1 Premises

The heart is the central organ of the cardiovascular system. It is located inside the thoracic cavity, in the space between the two lungs (mediastinum), surrounded by a fibroserous sac (pericardium). At the bottom it rests on the diaphragmatic dome that separates it from the abdominal viscera, at the front it is protected by the sternum and the costal cartilages (3rd-6th), at the back it corresponds to the thoracic vertebrae from the 5th to the 8th (Giacomini cardiac vertebrae) and at the top it extends towards the upper opening of the thorax by means of the vascular pedicle, made up of the large vessels that originate or end in the heart (ascending aorta, pulmonary trunk and superior vena cava)[1].

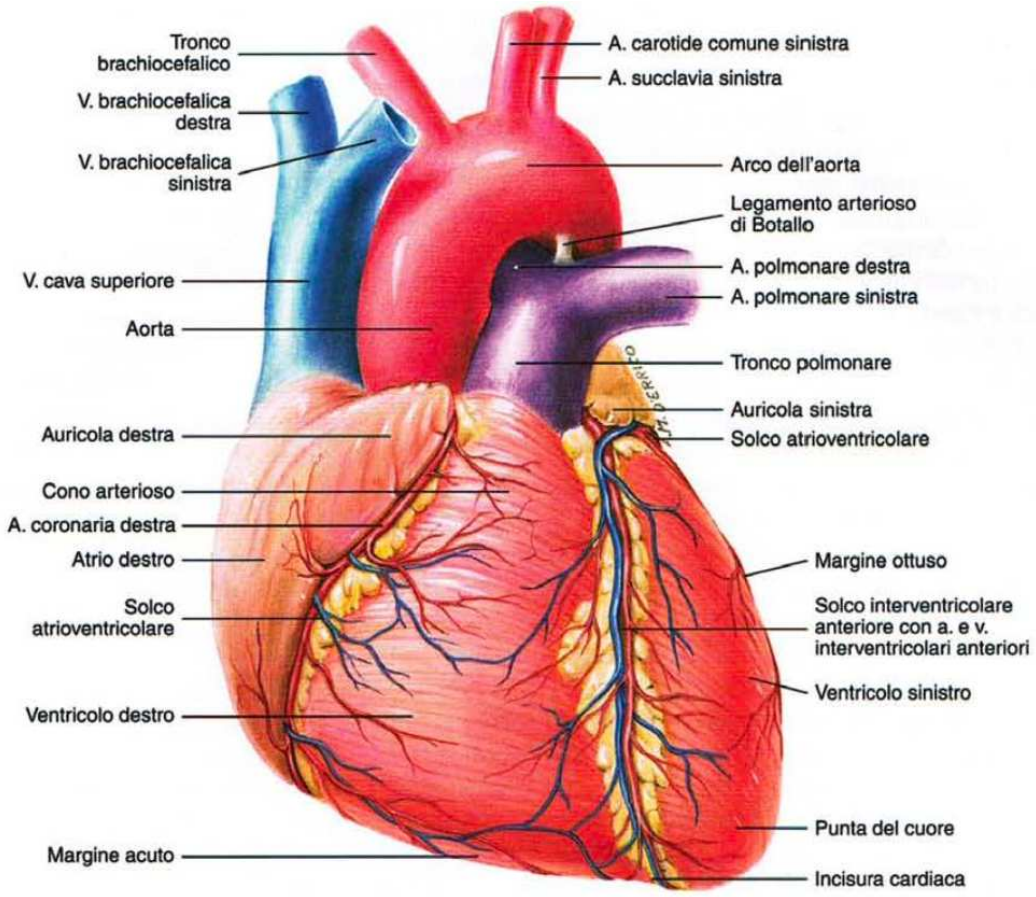

Figure 1 | *Sternocostal surface of the heart.*

Inside the heart there are four cavities: two atria (right and left atrium) and two ventricles (right and left ventricle). The four cardiac cavities are separated respectively by the interatrial septum and the interventricular septum. Both the two atria and the two ventricles have a common basic structural organization, even though there are substantial differences between the right and left cavities[1].

There are two groups of heart valves: the atrioventricular valves (mitral and tricuspid), which separate the atria from the ventricles, and the semilunar valves (aortic and pulmonary), which separate the ventricles from the large arteries. Although the function of each group of valves is similar, their anatomies are different. The atrioventricular valves consist of two leaflets (mitral) or three leaflets (tricuspid), with supporting external chordae tendineae that connect the leaflets to the papillary muscles within the ventricles[2]. In contrast, the semilunar valves, located at the base of the aorta and pulmonary trunk, consist of three cusps, and do not have chordae tendineae or external papillary muscles, although a particular internal support structure has been described[3].

1.2 Anatomy of the cardiac atria

In the atria, the internal surface appears smooth and regular in the region between the openings of the large veins, while laterally and anteriorly it takes on a trabeculated appearance. The wall has an average thickness of 1 mm. On the floor, there is the atrioventricular orifice, which is equipped with a valve that allows each atrium to communicate with the underlying ventricle[1].

1.3 Anatomy of the cardiac ventricles

The two ventricles share a similar structural organization, with a conical shape, a posterosuperior base, and an anteroinferior apex. Each ventricle has three distinct parts: the inflow portion, including the atrioventricular valve and its support system; the central-apical portion, characterized by a finely trabeculated surface; and the outflow portion, located beneath the semilunar valve.

At the base of each ventricle are two valve-equipped orifices: the atrioventricular orifice, positioned posteriorly, for blood inflow, and the arterial orifice, located anteriorly, for outflow. The central-apical portion is marked by ridges called trabeculae carneae, formed by myocardial bundles. Papillary muscles, a first-order trabeculae, are anchored to the ventricular wall and project into the cavity. Chordae tendineae, thin tendons of dense fibrous tissue, connect the papillary muscles to the atrioventricular valves. Together, the papillary muscles and chordae tendineae form the tension or anchoring apparatus of the valve, which prevents the prolapse of the valve leaflets into the atrial cavity during ventricular systole[1].

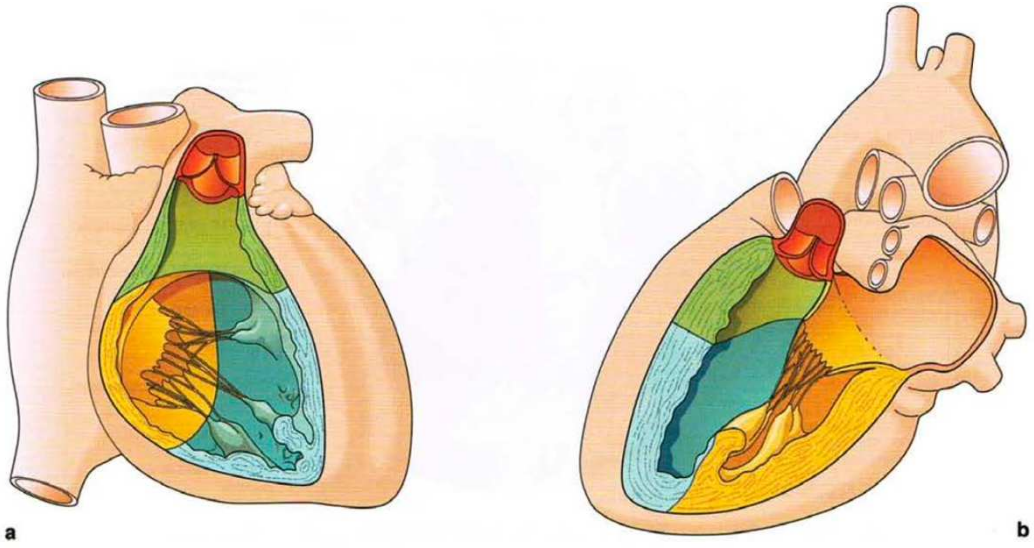

Figure 2 | *Representation of the ventricular cavities: (a) right ventricle; (b) left ventricle. In yellow, inflow portion; in green, outflow portion; in blue, trabeculated portion; in red, initial section of the large arteries with valves.*

The right ventricle has a wall thickness of about 3 mm and a crescent-shaped cavity, positioned around the left ventricle. A muscular ridge called the supraventricular crest separates the inflow from the outflow portion and connects to the septomarginal trabecula (Leonardo da Vinci's moderator band). In contrast, the left ventricle has a thicker wall, about 9-10 mm, thinning towards the apex, and a nearly circular cavity in cross-section. Unlike the right ventricle, the left ventricle has no distinct anatomical separation between the inflow and outflow portions; the anterior leaflet of the mitral valve serves as the partition.

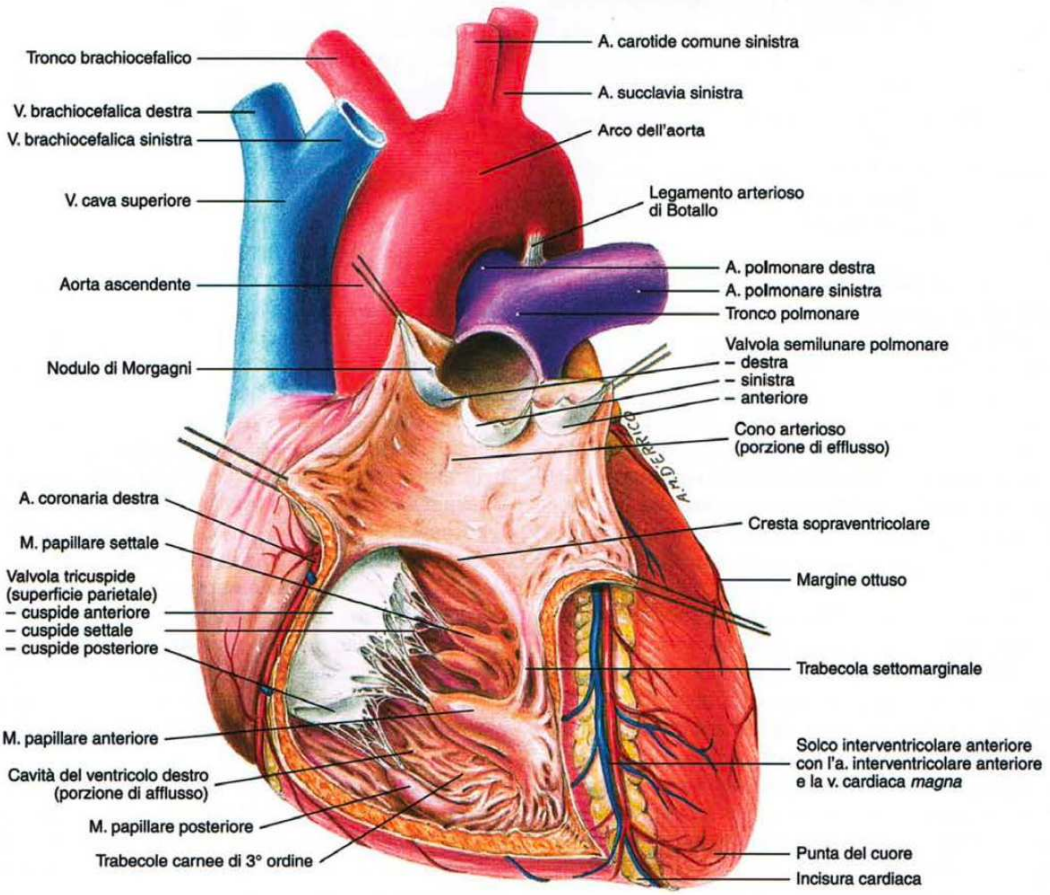
Tronco brachiocefalico
V. brachiocefalica destra
V. brachiocefalica sinistra
V. cava superiore
Aorta ascendente
Nodulo di Morgagni
A. coronaria destra
M. papillare settale
Valvola tricuspide
(superficie parietale)
– cuspide anteriore
– cuspide settale
– cuspide posteriore
M. papillare anteriore
Cavità del ventricolo destro
(porzione di afflusso)
M. papillare posteriore
Trabecole carnee di 3° ordine
A. carotide comune sinistra
A. succlavia sinistra
Arco dell'aorta
Legamento arterioso
di Botallo
A. polmonare destra
A. polmonare sinistra
Tronco polmonare
Valvola semilunare polmonare
– destra
– sinistra
– anteriore
Cono arterioso
(porzione di efflusso)
A. INTERVENTRICOLARE ANTERIORE
Cresta sopraventricolare
Margine ottuso
Trabecola settomarginale
Solco interventricolare anteriore
con l'a. interventricolare anteriore
e la v. cardiaca *magna*
Punta del cuore
Incisura cardiaca

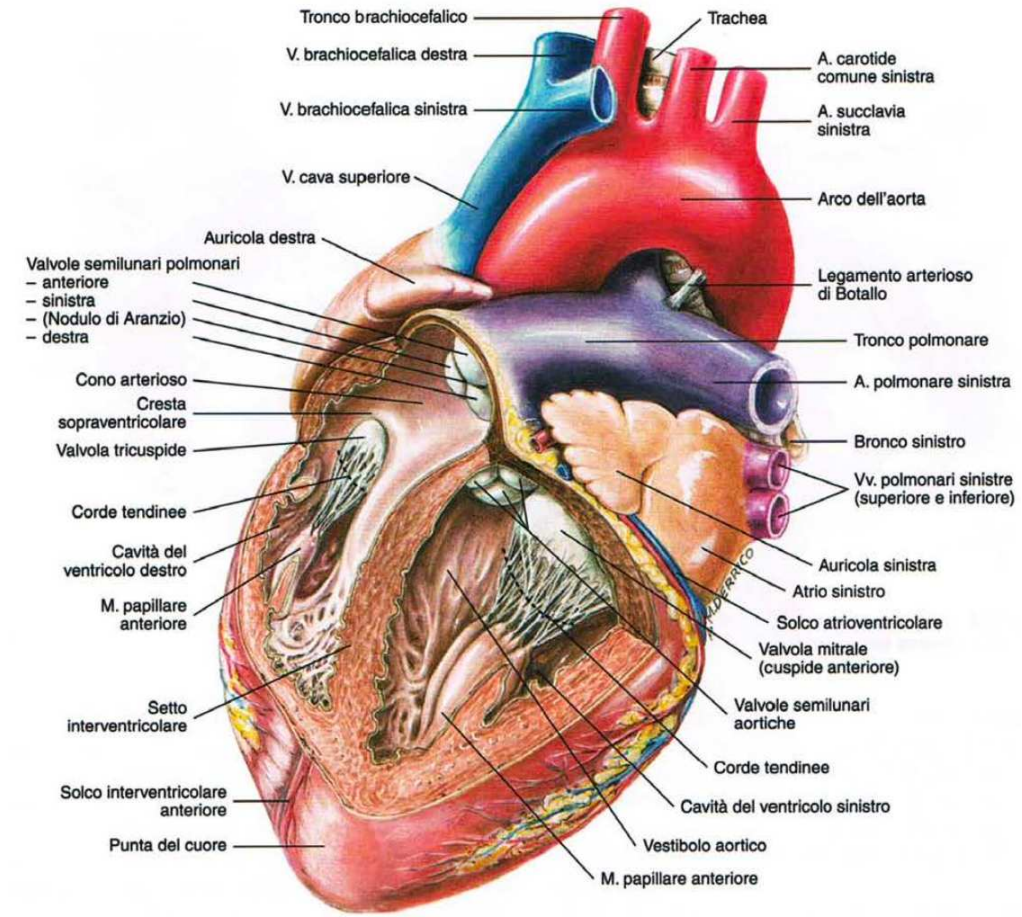
Tronco brachiocefalico
V. brachiocefalica destra
V. brachiocefalica sinistra
V. cava superiore
Auricola destra
Valvole semilunari polmonari
– anteriore
– sinistra
– (Nodulo di Aranzio)
– destra
Cono arterioso
Cresta
sopraventricolare
Valvola tricuspide
Corde tendinee
Cavità del
ventricolo destro
M. papillare
anteriore
Setto
interventricolare
Solco interventricolare
anteriore
Punta del cuore
Trachea
A. carotide
comune sinistra
A. succlavia
sinistra
Arco dell'aorta
Legamento arterioso
di Botallo
Tronco polmonare
A. polmonare sinistra
Bronco sinistro
Vv. polmonari sinistre
(superiore e inferiore)
Auricola sinistra
Atrio sinistro
Solco atrioventricolare
Valvola mitrale
(cuspide anteriore)
Valvole semilunari
aortiche
Corde tendinee
Cavità del ventricolo sinistro
Vestibolo aortico
M. papillare anteriore

Figure 3 | *Cavities of the ventricles, seen from the front and from the left, after wide resection and removal of their anterior wall and of the interventricular septum.*

1.4 Plan of the heart valve

The four heart valves are located approximately on the same plane, oblique from left to right and top to bottom, known as the valvular plane, which corresponds to the atrioventricular junction. A slight misalignment between the floors of the two atria causes a thin upper strip of the interventricular septum to separate the left ventricle from the right atrium (atrioventricular septum).

The fibrous skeleton of the heart, located at the valvular plane, is a robust connective tissue structure that anchors the muscle bundles and provides support for the heart valves. It also separates the atrial and ventricular muscles. The fibrous skeleton, made of dense connective tissue with few elastic fibers, includes: the fibrous rings at the atrioventricular orifices and at the base of the major arteries, as well as the right and left fibrous trigones, and the membranous part of the interventricular septum[1].

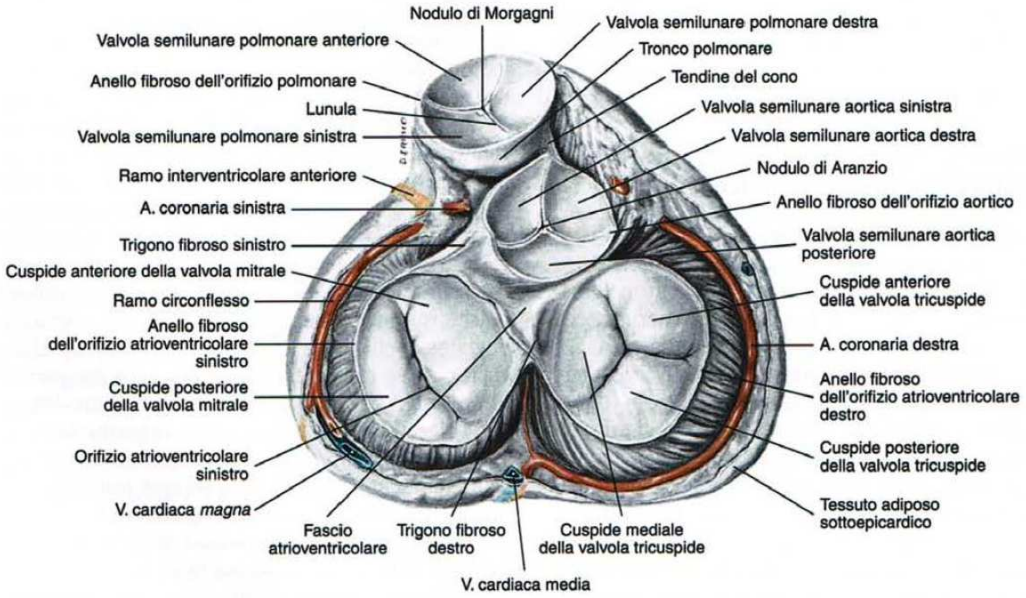

Figure 4 | *Base of the ventricles seen from above after removal of the atria, aorta and pulmonary trunk: section performed at the level of the valve plane.*

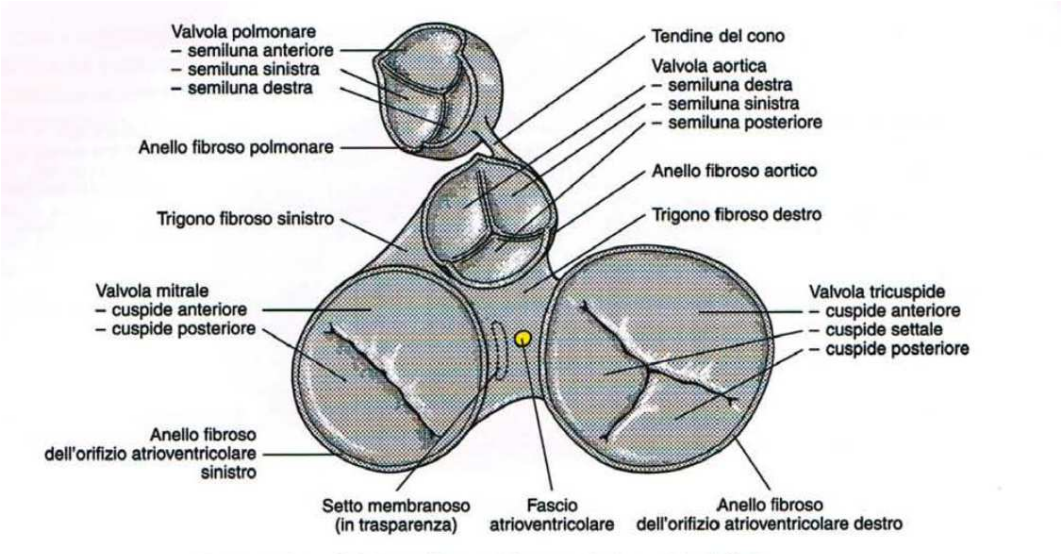

Figure 5 | *Fibrous skeleton of the heart, isolated, seen in profile and posteriorly.*

1.5 Anatomy of the atrioventricular valves

The atrioventricular and arterial orifices are equipped with valves that ensure unidirectional blood flow. The atrioventricular orifices have an oval shape, with a circumference of about 12 cm. The right atrioventricular valve (tricuspid) consists of three leaflets, while the left atrioventricular valve (mitral) has two. These leaflets are made of a fibrous lamina covered by endocardium and anchored by chordae tendineae, which are connected to papillary muscles. The papillary muscles and chordae tendineae prevent valve prolapse during ventricular systole. The cusps are not vascularized and are nourished by diffusion directly from the blood in which they are immersed. When ventricular pressure increases during ventricular systole, the cusps rise, approaching each other until the respective orifice closes. The closure of the valve occurs along a "closure line" on the leaflet's axial face a few millimeters away from the free margin. The right tricuspid valve's three leaflets (anterior, posterior, and septal) are supported by corresponding papillary muscles, while the left mitral valve's two leaflets (anterior and posterior) are supported by two papillary muscles (anterolateral and posteromedial). Each papillary muscle sends chordae tendineae to both leaflets, ensuring effective valve function.

The anterior leaflet of the mitral valve assumes close relationships of contiguity with the aortic valve, in particular with the posterior crescent, due to the welding

existing in this location between the fibrous ring of the atrioventricular orifice and that of the aortic orifice[1].

1.6 Anatomy of the semilunar valves

The arterial valves, known as semilunar valves, are simpler than the atrioventricular valves. Both the aortic and pulmonary orifices are circular, with a circumference of about 7 cm. Each valve consists of three pocket-shaped membranous folds (half-moons) at the junction between the ventricular outflow portion and the origin of the corresponding artery, surrounded by a fibrous ring. The pockets have an adherent margin attached to the fibrous ring and a free margin that extends into the vessel lumen. Their structure includes a fibrous layer covered by endocardium on both sides, with a nodular thickening at the free margin (Morgagni's nodule for the pulmonary valve and Aranzio's nodule for the aortic valve). These nodules help the valve close completely during diastole, preventing blood from flowing back into the ventricle. Like atrioventricular valves, semilunar valves lack vascularization, and their structural strength ensures they open during systole and close during diastole without needing additional anchoring structures.

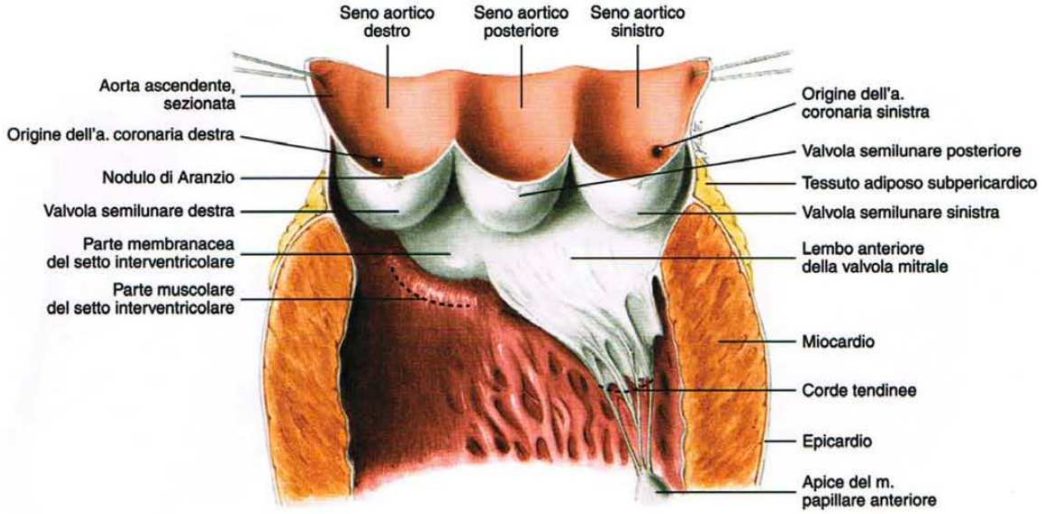

Figure 6 | *Aortic semilunar valve, frontal view.*

The pulmonary valve is composed of three equal-sized pockets: one anteriorly (the anterior crescent) and two posteriorly (the right and left crescents). Each crescent, at the midpoint of the free margin, features a small swelling called Morgagni's nodule.

The aortic valve also has three semilunar pockets: two anteriorly (the right and left crescents) and one posteriorly (the posterior crescent). The right and left crescents, which interface with the corresponding crescents of the pulmonary valve, are also referred to as coronary crescents because the right and left coronary arteries originate from the respective aortic sinuses of Valsalva, located in the ascending aorta. For this reason, the posterior crescent is also called the non-coronary crescent. At the midpoint of the free margin, each crescent has a nodular thickening known as Aranzio's nodule[1].

1.7 Structural composition of heart valves

The biomechanical function of valves is attributed to a highly organized network of extracellular matrix (ECM) components[5]. In addition to supporting the structure of valves, the ECM facilitates many biological processes because it contains molecules essential for cell signaling[6].

In healthy valves, the extracellular matrix (ECM) consists of three layers (possibly four in humans) arranged according to blood flow[7]:

- Fibrous layer: located near the outflow surface, it is made of densely packed collagen fibers and provides valve strength. After dissection, the thickness of the fibrosa layer was 317.14 ± 30.57 μm.
- Ventricularis layer: located on the inflow surface, it is rich in elastin and aids in stretching and retraction during the cardiac cycle. After dissection, the thickness of the ventricularis layer was 158.21 ± 21.24 μm.
- Spongiosum layer: located between the other two, this central layer contains loose connective tissue, proteoglycans (PGs), and glycosaminoglycans (GAGs), allowing the adjacent layers to move smoothly.

We observed that the fibrosa makes up 41% and the ventricularis 29% of the total thickness. This is important for calculating actual layer stresses, as the proper thickness of the fibrosa and ventricularis should be used. The spongiosa, with its high GAG content, is assumed to contribute minimally to tensile load-bearing[4].

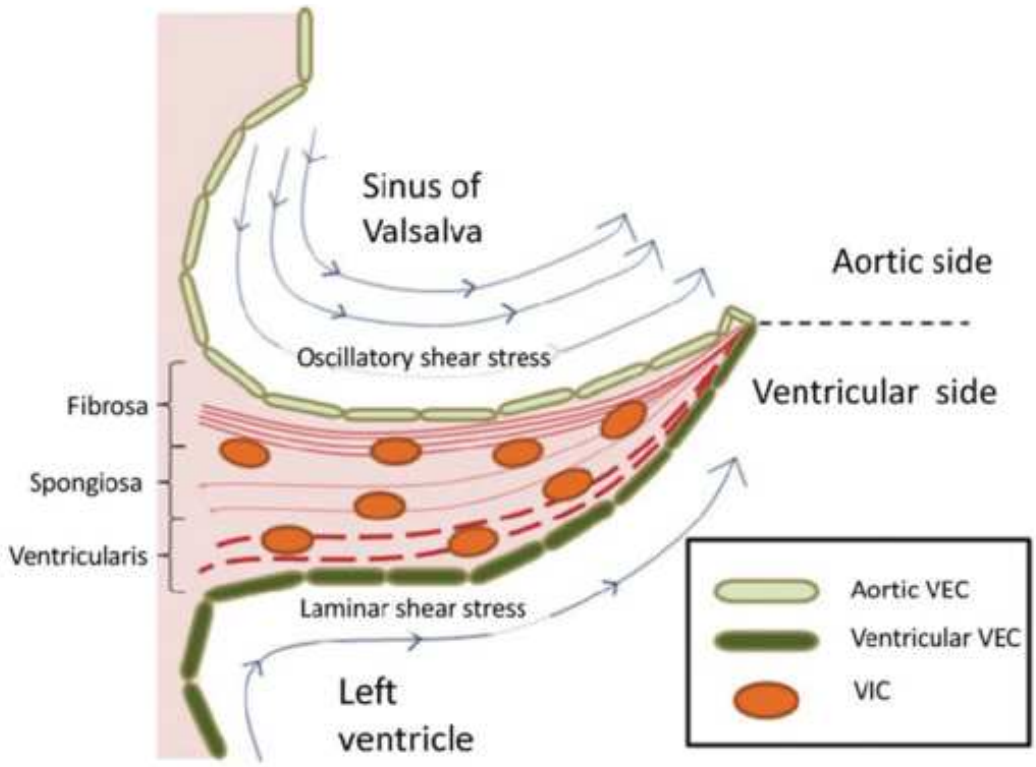

Figure 7 | *The three layers that form the extracellular matrix (ECM)*[8].

The extracellular matrix (ECM) in heart valves is composed of valvular interstitial cells (VICs) and lined by a single layer of valvular endothelial cells (VECs). Since the ECM is crucial for the valve's biomechanical function, the quantity, quality, and arrangement of its components (collagen, elastin, and PG-GAG) determine the valve's long-term durability. Recent studies show that the ECM layers are tightly coupled and do not slide against each other[9]. Despite each layer being histologically distinct, they function as a single unit with properties that change across the leaflet. The structure of the ECM also varies between different leaflets and within the same leaflet. Research suggests that this organization is conserved across many species, particularly in larger animals[10].

The ECM is essential for valve function, and imbalances in its components can be harmful. VICs, which resemble fibroblasts in healthy adults, regulate ECM homeostasis by managing wear and tear through enzymes like matrix metalloproteinases (MMPs) and their inhibitors (TIMPs)[11,12]. VICs play a key role in maintaining valve structure and function. Additionally, the VECs form a protective barrier between the blood and the valve tissue, preventing damage and excessive inflammation[13,14]. VECs also communicate with VICs to regulate their

behavior. These molecular interactions demonstrate that cardiac valves are complex and dynamic structures with a highly sophisticated architecture.

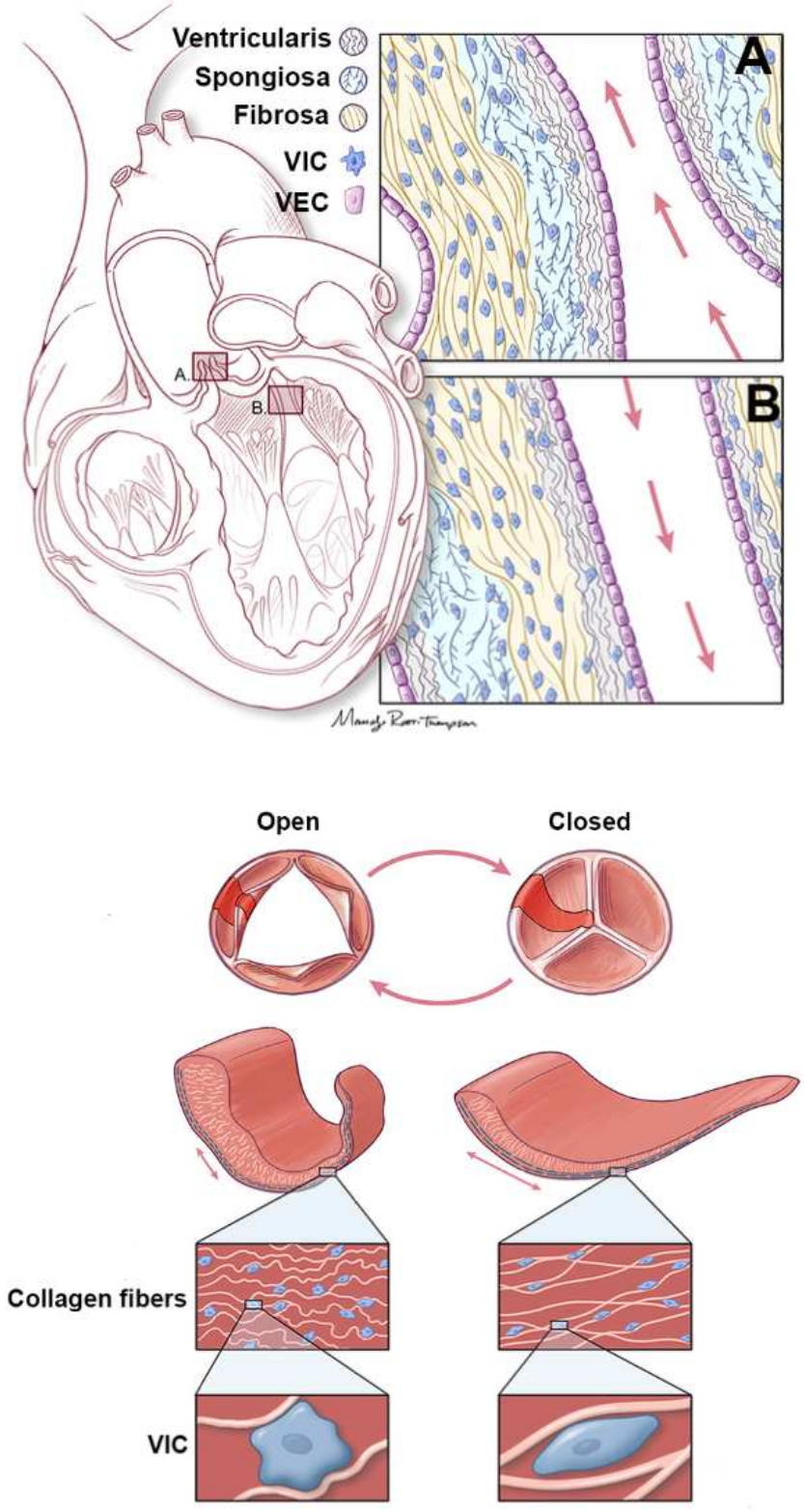

Figure 8 | *Representation of the structure of the aortic and mitral valves. The first image shows the organization of the three ECM layers, including the ventricularis (elastin-rich*

layer), spongiosum (proteoglycan and glycosaminoglycan-rich layer), and fibrosus (collagen-rich layer). Each layer is arranged according to blood flow, as indicated by the red arrows (the ventricularis/atrialis is the layer closest to the blood flow). Above the valve leaflets (mitral) or cusps (aortic) is a single layer of valve endothelial cells (VECs, colored purple), while a population of valve interstitial cells (VICs, colored blue) is embedded within the valve nucleus. In the second image, the ECM fibers of the aortic valve are represented. Attention is paid to their reorganization and the elongation of the VICs cells during systole (valve open) and diastole (valve closed).

1.8 ECM and valvular disease

Valvular diseases occur when the normal structure-function relationship of the valve is disrupted. These diseases are caused by a combination of genetic, mechanical, environmental, and inflammatory/immunological factors, which abnormally affect valvular endothelial cells (VECs), valvular interstitial cells (VICs), and the ECM.

Valvular diseases can be congenital, such as bicuspid aortic valve, with structural malformations present at birth. Advances in genome sequencing have helped identify the genetic causes behind these congenital defects during fetal development.

Alternatively, valvular diseases can be acquired, such as calcification and myxomatous degeneration[15]. These conditions are often linked to age-related degeneration, prolonged exposure to risk factors like male sex, hypertension, and smoking, which put wear-and-tear stress on the valve leaflets[16]. Inflammation also plays an increasing role in the development of these diseases.

Although some cases remain idiopathic, emerging evidence suggests that acquired valvular diseases may originate during embryonic development, with the phenotype manifesting later in life due to additional risk factors.

2. Valvular heart disease (VHD)

2.1 Epidemiology

Valvular heart disease (VHD) is one of the major causes of cardiovascular morbidity and mortality worldwide. The epidemiology of VHD is difficult to study because, in most cases, it is a chronic and often asymptomatic condition. Post-mortem analyses have revealed that the true prevalence of VHD is significantly higher than what is clinically detected[17]. In fact, data are typically collected only when the disease is moderate or clinically relevant, as patients usually undergo diagnostic tests due to symptoms or clinical indications. Moreover, the specific causes of VHD may be misclassified, particularly in areas where rheumatic heart disease (RHD) is endemic, leading to potential errors in classification[18].

Echocardiography is the gold standard for diagnosing VHD; thus, accurately assessing its prevalence would require performing echocardiographic examinations on a population that is as representative as possible[19]. However, limited access to echocardiography and microbiological testing contributes to the underestimation of VHD, especially in developing countries. Although heart murmurs are an important sign of VHD, they lack sensitivity and specificity[20].

There are significant differences in the epidemiology of VHD between high- and low-income countries. Most of the morbidity and mortality attributable to VHD globally is due to RHD, which is more common in low-income countries and affects approximately 41 million people worldwide. In contrast, high-income countries show a higher prevalence of degenerative VHD, particularly calcific aortic stenosis and degenerative mitral valve disease, affecting around 9 and 24 million people, respectively[21]. Other causes of VHD include infective endocarditis (IE), inflammatory diseases, and congenital conditions. Radiation- and drug-induced VHD have been characterized more recently, and their prevalence may be underestimated[22,23].

It is estimated that approximately 250000 prosthetic heart valves are implanted annually worldwide[24].

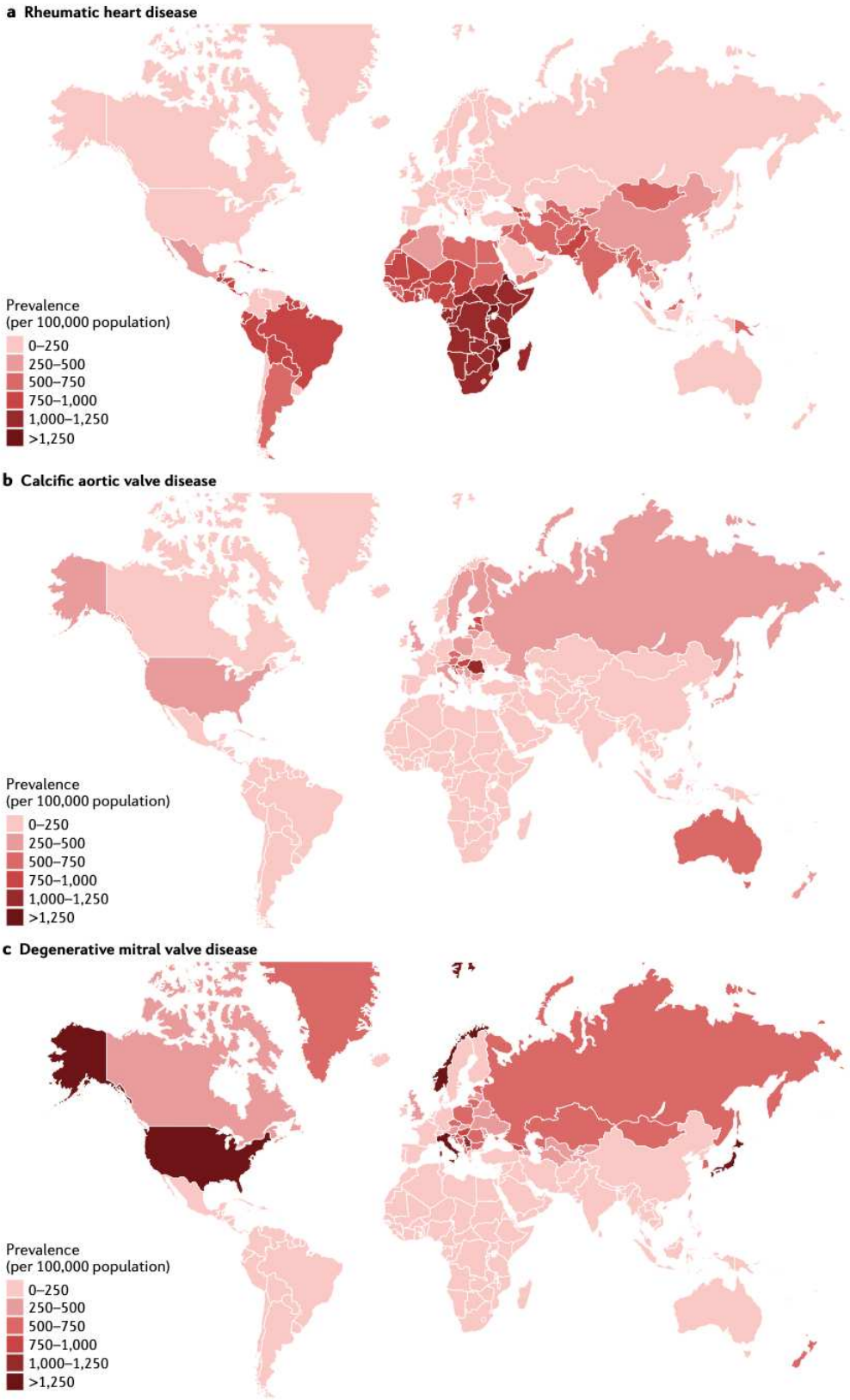

Figure 9 | *Global prevalence of the three main forms of valvular heart disease. The maps show the global prevalence, standardized by age, per 100,000 inhabitants of rheumatic heart disease (part a), calcific aortic valve disease (part b) and degenerative mitral valve disease (part c).*

2.1.1 Epidemiology in industrialized countries

In industrialized countries, degenerative etiology is the leading cause of valvular disease, affecting 63% of patients across all European regions. Rheumatic heart disease is the second most common cause, accounting for 22% of cases. Other etiologies, such as infective endocarditis (IE), inflammatory diseases, and congenital conditions, represent 15% of all cases (Figure 10). In Europe, the Euro Heart Survey on valvular heart disease included 5001 patients[25]. According to this study, aortic stenosis (AS) was the most frequent valvular disease (43%), followed by mitral regurgitation (MR) (32%), aortic regurgitation (AR) (13%), and mitral stenosis (MS) (12%) (Figure 11).

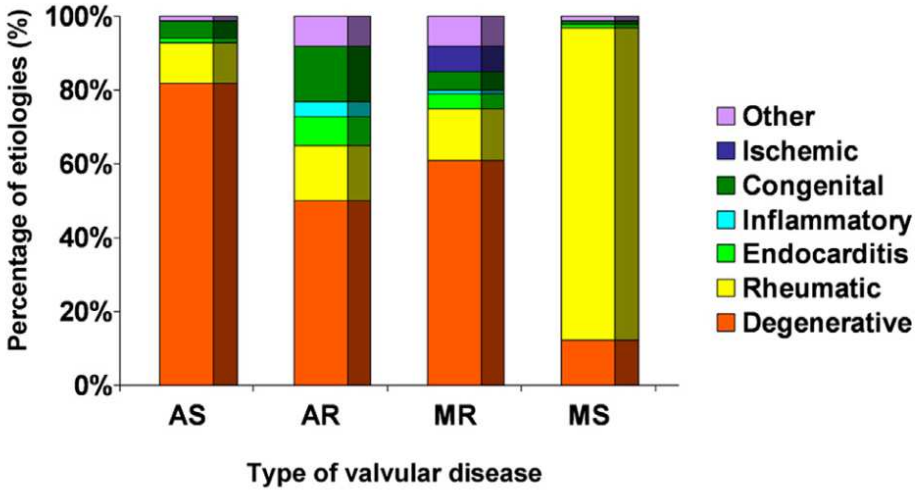

Figure 10 | *Distribution of etiologies according to the type of valvular heart disease in a European subpopulation (Euro Heart Survey on valvular disease)*[26].

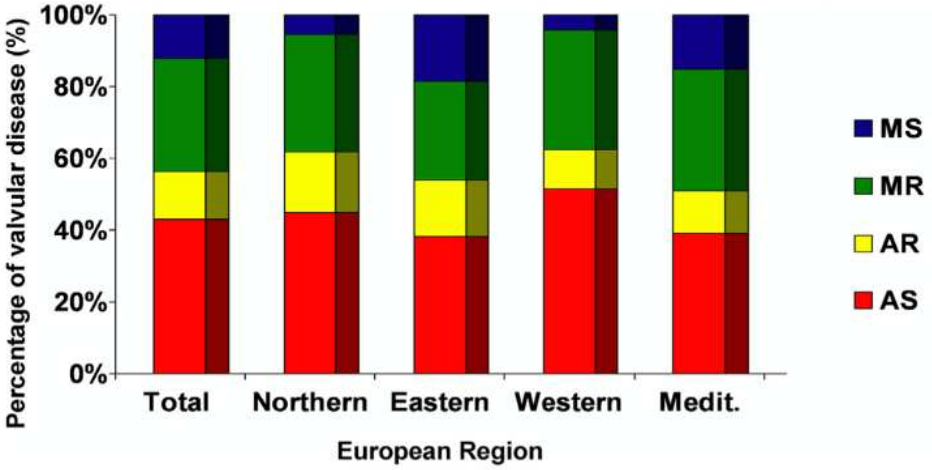

Figure 11 | *Distribution of VHD etiologies in the 4 European region[25]. AR, aortic regurgitation; AS, aortic stenosis; MR, mitral regurgitation; MS, mitral stenosis.*

A U.S. study involving 11911 subjects undergoing echocardiography showed that the prevalence of valvular heart disease increases significantly with age: it is less than 2% before the age of 65 but rises to 13.2% after the age of 75[27]. This increase in prevalence reflects the predominance of degenerative valvular heart disease in industrialized countries, where advancing age is directly related to higher life expectancy.

Heart valves open and close more than 100,000 times a day, 40 million times a year, and over 3 billion times during a 75-year lifespan to maintain unidirectional blood flow during the cardiac cycle. During diastole, the papillary muscles relax, and high atrial pressure causes the mitral (left) and tricuspid (right) valve leaflets to open, allowing blood to flow into the ventricles. As ventricular pressure increases, the chordae tendineae pull the atrioventricular valve leaflets closed, preventing them from inverting toward the atria. During ventricular contraction, blood flows through the now-open semilunar valves, and the ventricles relax to restart the cycle.

Throughout the cardiac cycle, heart valves are subjected to continuous changes in hemodynamic forces due to pressure differences between systole and diastole. These forces exert mechanical stresses on the valves, including: (1) tension when the valve is closed, (2) bending during opening and closing movements, and (3) shear from blood flow when the valve is open[28]. Healthy heart valves withstand these stresses by constantly maintaining and adapting their complex, highly organized connective tissue structures[29].

2.1.2 Epidemiology in developing countries

Rheumatic heart disease (RHD) is the leading cause of primary valvular heart disease in developing countries and globally. In 2019, RHD was estimated to affect approximately 41 million people (95% CI 32.1-50.1), with an incidence of 2.8 million new cases per year. Data from the REMEDY registry indicate that most patients with RHD who visit hospitals have moderate to severe forms of the disease, suggesting that the actual prevalence is likely much higher than reported.

Rheumatic valvular disease primarily affects the mitral and aortic valves and predominantly impacts young adults. This condition is a direct result of the ongoing incidence of acute rheumatic fever, estimated at 5 to 50 cases per 100,000 people annually in developing countries[30]. Risk factors for RHD are largely linked to socioeconomic status, as evidenced by high rates of malnutrition and overcrowding in these regions[31].

Degenerative valve diseases are less common in these areas due to shorter life expectancy. Most epidemiological studies on chronic rheumatic heart disease rely on systematic clinical screening (including patient history and auscultation) of school-age children, often confirmed by echocardiography. These studies report prevalence rates of rheumatic valvular disease ranging from 1 to 7 cases per 1,000 people[32].

2.2 Valvular stenosis and valvular insufficiency

From a physiopathological point of view, valvular diseases are divided into stenosis and valvular insufficiency:

- Stenosis is the narrowing of the valvular orifice, reducing its area significantly below normal values. This creates a pressure gradient between the cavities upstream and downstream of the valve, leading to relative hypertrophy of the upstream cavity. Valvular stenosis is always a chronic process and never acute.
- Insufficiency, on the other hand, involves the regurgitation of a certain amount of blood: during systole for mitral and tricuspid insufficiency, and during diastole for aortic insufficiency. The ventricle must handle both the antegrade portion of blood and the retrograde portion that regurgitates, which means it must increase its overall systolic output. This results in an increase in the volume of the ventricle due to eccentric remodeling. Insufficiency can be either an acute or chronic process, and the pathophysiology of the two forms is distinctly different.

In adult patients, the valves most frequently affected by acquired pathologies are the mitral and aortic valves. The tricuspid valve is usually affected secondarily to

diseases of the first two. The pulmonary valve, on the other hand, is primarily affected by congenital pathologies. As discussed in the epidemiology section, until a few decades ago, the predominant etiology was almost exclusively rheumatic; today, however, with increased life expectancy, degenerative conditions have also become significant, leading to stenosis and/or aortic or mitral insufficiency, while mitral stenosis remains rare[33].

2.3 Valvular aortic stenosis (AS)

Aortic stenosis is the narrowing of the aortic valve. Normally, the aortic valve has an opening of 3.5-4 cm^2. In aortic stenosis, this opening decrease to below 2 cm^2, and in severe cases, it can drop below 1 cm^2. There are also supravalvular and subvalvular aortic stenoses, which are congenital conditions that affect the area around the valve rather than the valve itself. Supravalvular stenosis involves a fibrous band above the valve, while subvalvular stenosis is due to a fibromuscular membrane or spur below the valve. During systole, blood flows rapidly through the narrowed valve, striking the aortic wall and promoting its growth. This leads to dilation and lengthening of the ascending aorta, which not only affects blood flow but can also result in an aneurysm[33].

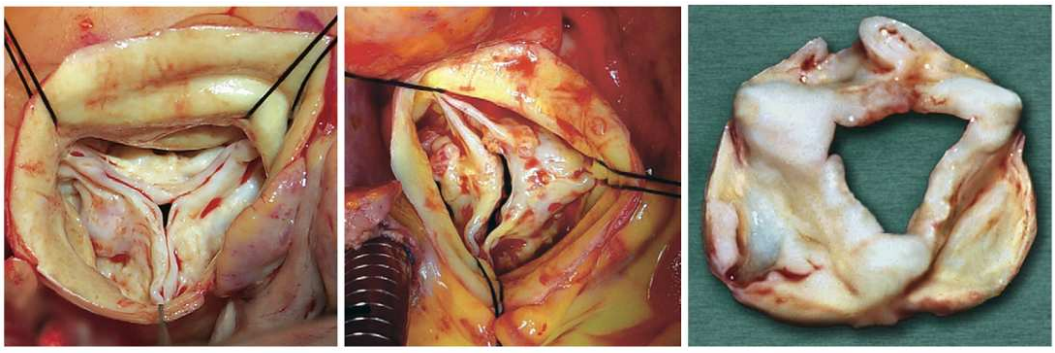

A **B** **C**

Figure 12 | *Operative images of aortic valve stenosis[37]. **(A)** Aortic valve stenosis, degenerative type. Normal three-leaflet architecture is maintained. Commissures are not fused. Leaflets are held in a closed position due to diffuse, nodular calcific deposits. This morphology is presumed to be atheromatous. **(B)** Aortic valve stenosis, congenital type. The valve is bicuspid, with fusion of the commissure between the left and right coronary leaflets. There is heavy dystrophic calcification of the leaflets. The valve orifice is eccentric and slit-like. **(C)** Aortic valve stenosis and regurgitation, rheumatic type. Normal three-*

leaflet structure is retained. There is scarring and shortening of the leaflets with rolling of the free edges, resulting in central regurgitation due to a lack of leaflet coaptation. The thickened leaflets also obstruct left ventricular outflow (aortic valve stenosis).

2.3.1 Etiology

In most cases, aortic stenosis is caused by senile calcific degeneration of the valve. However, younger patients with a bicuspid aortic valve can also experience calcific degeneration, as this congenital anomaly leads to abnormal blood flow that wears out the valve prematurely. Typically, degeneration occurs in the tricuspid valve in elderly patients. This wear and tear, accompanied by inflammatory and calcification processes, resembles but is not identical to atherosclerosis. As a result, the valve cusps stiffen and thicken, becoming less mobile and with reduced opening due to calcium deposits. Importantly, the commissures remain unfused, and theoretically, the valve can still open to a normal area if forced[34].

The risk factors for atherosclerosis (such as hypertension, smoking, diabetes, family history, and dyslipidemia) are also associated with degenerative aortic stenosis. Because of this, there has been interest in using atherosclerosis medications, particularly statins, to prevent or reverse aortic stenosis, although this hypothesis has not yet been confirmed experimentally.

In about 10% of cases, the etiology is rheumatic. In this scenario, the commissures are fused, and the cusps are thickened and deformed. However, isolated rheumatic aortic stenosis is rare; the mitral valve is almost always involved (a condition known as mitro-aortic defect).

2.3.2 Pathophysiology

The essence of aortic stenosis is the presence of a transvalvular aortic gradient, which causes the acceleration of blood through the narrowed valve.

$$Gradient = \Delta P = 4 \times v^2.$$

The speed of blood flow through the aortic valve depends on several factors: the systolic output (and thus cardiac output), the aortic valve area, and the duration of systole. In aortic stenosis, systole is somewhat prolonged, although it varies little with heart rate[33].

Echocardiography is essential for confirming the diagnosis of aortic stenosis. Current international guidelines for echocardiographic evaluation focus on three key measurements: the transaortic gradient (the most reliable parameter), the peak transvalvular velocity (Vmax), and the valve area. While valve area is the ideal measurement for assessing severity, there are several technical limitations to consider[35].

	Frazione di eiezione	Gradiente medio	Area (cm^2)
Lieve	Normale	< 25	> 1,5
Media	Normale	25 - 50	1 - 1,5
Grave	Normale	> 40	< 1
"Low flow low gradient"	Normale o ridotta	< 40	< 1

Figure 13 | *Classification of aortic stenosis according to the level of severity*[36].

As regards the valve area, referring to the following Figure 14, it is clear why the area value of 1 cm^2 constitutes the watershed between medium and severe forms. Above this value, valve resistance decreases significantly and is practically normal for values of approximately 1.5 cm^2, while for lower values, it increases.

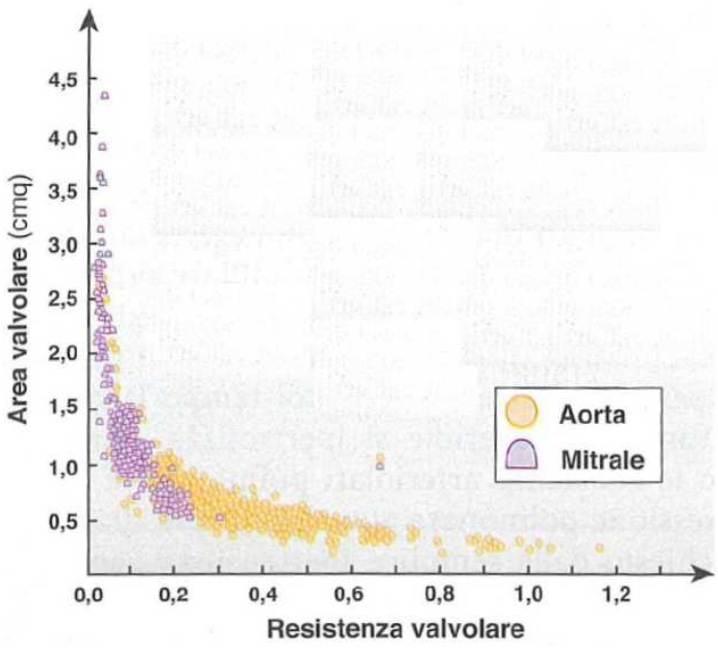

Figure 14 | *Relationship between valve area and valve resistance in mitral stenosis and aortic stenosis[33]. Resistance is a parameter obtained by dividing the gradient by the transvalvular flow. It can be observed that valve resistance is not high until the area falls below 1 cm^2.*

The term "transaortic gradient" refers to the increase in systolic pressure in the left ventricle. The physiological response to this increase is concentric hypertrophy, which involves an increase in the number of sarcomeres arranged in parallel. This leads to a thicker ventricular wall without changing the volume of the chamber. This normalization of wall stress (afterload) allows the left ventricle to maintain normal systolic function even with significantly increased pressure.

However, the same cannot be said for diastolic function. The increase in muscle mass reduces the rate of relaxation, and the thicker walls decrease the chamber's distensibility. Moreover, this "pathological" hypertrophy includes not just an increase in contractile muscle mass but also in fibrous tissue, making the ventricle less distensible overall. Consequently, with normal end-diastolic volumes, end-diastolic pressure tends to rise early.

Coronary flow is also affected. The coronary perfusion gradient is the difference between aortic diastolic pressure and left ventricular end-diastolic pressure, meaning coronary flow tends to decrease in aortic stenosis. Additionally, hypertrophy increases metabolic demands for blood flow, which are usually met by coronary reserve at rest. However, this reliance on coronary reserve leads to its reduction, increasing the risk of inducible ischemia[33].

2.3.3 Natural history

Valvular aortic stenosis is progressive, with variable speed: on average the area reduces by 0.05 cm^2/year while the gradient increases by 5-10 mmHg/year. Ventricular function also deteriorates over time, due to subtle ischemic damage and the gradual increase in the fibrous component. Systolic dysfunction then appears, the ventricle dilates, and the clinical picture rapidly worsens with signs of severe heart failure.

Aortic stenosis, even if severe, is asymptomatic as long as the adaptive mechanisms work, that is, for many years. But when it becomes symptomatic the risk of death

increases rapidly: it is almost 50% per year if it manifests with heart failure, 30% if it manifests with syncope, 20% per year if it manifests with angina[37].

2.3.4 Treatment

There is no specific medical treatment for aortic stenosis. Today, the treatment of aortic stenosis is mainly surgical. Aortic stenosis is the most common primary valve lesion requiring surgery or transcatheter intervention in Europe and North America[38]. The surgical indications are:

- **Severe aortic stenosis and symptomatic patient**. This is an indisputable indication, because the improvement in survival and quality of life after surgery is always very clear. Even if left ventricular function is depressed, surgery should be considered, albeit with obviously increased risk, because a reduction in afterload and therefore an improvement in pump function should be expected.
- **Severe aortic stenosis and asymptomatic patient**. This is a controversial indication. First, it is good to really ascertain the absence of symptoms. If truly asymptomatic, surgery can be considered in the presence of serious coronary alterations or certain signs of rapid progression of the stenosis (for example, severe calcifications). Of course, LV dysfunction is also an indication, but it is unlikely that in this case the patient is asymptomatic. In the absence of adverse prognostic features, watchful waiting has generally been recommended with prompt intervention at symptom onset.
- **Medium-severe aortic stenosis**. It may be an indication in the presence of symptoms attributable to aortic stenosis, or if another cardiac surgery is necessary on another valve or on the coronary arteries, or if there is left ventricular systolic dysfunction.

2.4 Aortic valve regurgitation (AR)

Aortic valve insufficiency is a failure of the aortic valve cusps to coapt during diastole, resulting in blood regurgitation into the left ventricle.

2.4.1 Etiology

Aortic insufficiency can be classified into two types: organic and functional. Organic aortic insufficiency is due to primary disease of the valve leaflets, while functional aortic insufficiency arises from dilation of the aortic root, which prevents proper closure of the cusps during diastole.

In terms of organic aortic insufficiency, rheumatic disease is now less common in the Western world as a standalone cause, but it remains epidemiologically significant globally. More often, rheumatic disease leads to aortic steno-insufficiency, which also involves the mitral valve. In elderly patients, sclero-calcific degeneration is an important cause and can affect both bicuspid and tricuspid valves. Additionally, bacterial endocarditis and systemic diseases like rheumatoid arthritis, scleroderma, and Takayasu arteritis are also notable causes of aortic insufficiency[33].

Functional aortic insufficiency is primarily due to dilation of the valve ring. Annular-valvular ectasia can occur in various conditions, including Marfan syndrome, cystic medial necrosis, and occasionally from hypertension or the use of anorectic drugs in the past. Lastly, type I aortic dissection is a significant cause of acute aortic insufficiency.

2.4.2 Pathophysiology

In aortic valve insufficiency, some of the blood pumped into the aorta re-enters the left ventricle during diastole and is then pumped back into the aorta during the next systole. The left ventricle adapts to this regurgitation differently in acute versus chronic cases.

In acute aortic insufficiency, the backflow of blood reduces the forward ejection of blood and causes the left ventricle to exceed its normal filling capacity. While the volume of the ventricle increases slightly, the filling pressure rises significantly, reaching 40-50 mmHg. This can lead to pulmonary edema and low cardiac output, resulting in cardiogenic shock. The main adaptive response in this case is sympathetic stimulation, leading to tachycardia and increased contractility.

In chronic aortic insufficiency, the left ventricle adapts by increasing its overall stroke volume. This allows the forward ejection to remain normal or nearly normal despite significant regurgitation. The adaptation involves eccentric hypertrophy, which means an increase in myofibrils and sarcomeres arranged in series. This increases the cavity volume without overly stretching the fibers, so filling pressure and ejection fraction remain normal for a time.

The overall stroke volume increases because it includes both the forward and backward flow. As a result, systolic pressure rises while diastolic pressure decreases, which increases afterload and may compromise coronary blood flow. The wall thickness also increases to maintain a constant mass-to-volume ratio. Eventually, the ventricle can reach extremely large volumes, known as "*cor bovinum*".

Although hemodynamics initially remains well compensated, the coronary blood supply to the hypertrophied ventricle becomes inadequate, particularly due to lower aortic diastolic pressures. Over time, this can lead to ischemic areas and fibrous tissue replacement, reducing the left ventricle's contractile function. The ventricle dilates, the mass-to-volume ratio decreases, and filling pressure rises significantly. Consequently, this can lead to left-sided heart failure and eventually congestive heart failure.

2.4.3 Treatment

In aortic insufficiency, medical therapy has a certain rationale, although it is not curative. The underlying theory is that vasodilators (ACE inhibitors and dihydropyridine calcium antagonists) promote antegrade flow and reduce regurgitation. Their usefulness in acute insufficiency is certain; their usefulness in chronic insufficiency is more controversial. However, medical treatment with vasodilators should be limited to patients with even significant aortic insufficiency, but who are asymptomatic and have normal left ventricular function. Otherwise, medical treatment may be worsening[33].

Surgical indication is given in the following cases[39]:

- Aortic insufficiency must be significant. Significance is documented by echocardiographic data (PHT, regurgitation fraction, vena contracta diameter).
- The patient must be symptomatic. Any symptom is important and should be evaluated because it is usually a sign of an initial depression of left ventricular function (even if not measurable).
- Left ventricular function is indifferent, although obviously the risk is increased when the ejection fraction is reduced. However, there do not appear to be any contraindications if the ejection fraction is less than 30%, although the surgical risk becomes very high. The left ventricular end-systolic volume seems to be more sensitive: if > 100 ml/m2 the surgical risk increases exponentially.
- In asymptomatic patients, the indication is given if there is an (even) initial reduction in left ventricular function: if the ejection fraction < 50% or the end-systolic volume increases or the mass/volume ratio is reduced. In general, the intervention should not be late, because otherwise the left ventricle does not recover function, nor should it be too early because it exposes the patient to the risk of a second intervention.

2.5 Mitral valve stenosis (MS)

Mitral valve stenosis is a narrowing of the mitral valve orifice. Normally the mitral valve has an area of 4-5 cm^2 when open. In mitral stenosis the mitral area drops below 2 cm^2, in the narrow forms even below 1 cm^2.

2.5.1 Etiology

The main cause of acquired mitral stenosis is rheumatic disease. Rheumatic disease causes thickening of the leaflets and edema, and subsequently, after years, fusion of the commissures. The disease can extend to the subvalvular apparatus, with thickening of the chordae tendineae and papillary muscles, causing a further obstacle to ventricular filling. This is called the "subvalvular component" of mitral stenosis. Today, in industrialized countries, the degenerative etiology is emerging,

namely, calcific fibrosclerosis. This generally affects only the mitral annulus, and not the leaflets, and causes insufficiency due to dilation of the annulus[33].

2.5.2 Pathophysiology

The mitral valve area typically measures 4-5 cm². Under resting conditions, blood flows through the valve at a low speed of about 0.3 m/s. When the valve area is reduced, the speed of blood flow increases. This is because flow (in this case, diastolic flow) is equal to the product of the valve area (A) and the speed (v):

$$Diastolic\ flow = A \times v$$

If the mitral valve area (A) decreases, diastolic flow is maintained by increasing the velocity (v). However, this increase in velocity can only occur if there's an increase in pressure in the left atrium, creating a pressure gradient (ΔP) between the atrium and the left ventricle during diastole. The measurement of this gradient (in mmHg) is equal to four times the square of the velocity (expressed in m/s):

$$\Delta P = 4 \times v^2$$

The core issue of mitral stenosis is the increased pressure in the left atrium, which creates a transmitral gradient that accelerates blood flow through the narrowed valve. The speed of this flow, and thus the gradient, depends on the valve area and the overall flow. This flow is influenced by cardiac output and the duration of diastole. At higher heart rates, diastole shortens more than systole, leading to a higher gradient for the same cardiac output.

As pressure in the left atrium rises, it causes left atrial enlargement, which impacts the pulmonary veins, capillaries, and pulmonary artery. Initially, pulmonary arterial hypertension results from venous hypertension, but over time, the muscular walls of the arterioles thicken, increasing pulmonary arteriolar resistance and further elevating pulmonary pressure. This can overload the right ventricle, leading to dilation and tricuspid insufficiency, contributing to congestive heart failure. This is the condition of so-called "tricuspidized mitral stenosis".

A common complication of left atrial enlargement is atrial fibrillation. This condition results in the loss of mechanical function in the atrium, which can decrease cardiac output by up to 20%. More importantly, it leads to increased blood

stasis within the atrium, raising the risk of thrombus formation and subsequent systemic embolization[40].

2.5.3 Classification

The severity of mitral valve stenosis depends on the valve area[41].

- Mild stenosis if 1.5 $cm^2 \leq$ Area $\leq$ 2 cm^2.
- Moderate stenosis if 1 cm^2 < Area < 1.5 cm^2.
- Severe stenosis if Area < 1 cm^2.

This is a classification based on clinical experience, but a physiopathological justification can also be given by observing Figure 14. Resistance is practically zero when Area > 2 cm^2 and increases slowly until Area > 1 cm^2. The increase in resistance is instead precipitous for Area < 1 cm^2, thus justifying the adjective "Severe". Naturally, it is also good to evaluate other parameters that justify the severity of mitral stenosis: the pressure in the pulmonary artery, the function of the ventricles, in particular the right ventricle, and the continence of the tricuspid valve.

2.5.4 Natural history

Mitral stenosis is a progressive disease. The natural history is largely related to the progression of the stenosis, partly to the progression of pulmonary hypertension and the resulting right ventricular damage. Mortality was once due to episodes of pulmonary edema, cerebral embolism or congestive heart failure. Today it is possible to correct the stenosis before irreversible damage occurs[33,40].

2.5.5 Treatment

Patients with mitral stenosis should reduce physical activity and avoid stress that may trigger tachycardia. Women of childbearing age are advised to postpone pregnancy until after the stenosis is treated. The goal of medical therapy is to lower the trans-mitral gradient and reduce left atrial hypertension.

Typically, the threshold for surgery is lower than for percutaneous interventions. Surgery is indicated for severe mitral stenosis (valve area < 1 cm^2) if the patient is symptomatic and percutaneous options are not feasible. Surgical options include conservative and replacement procedures. Conservative intervention, such as mitral valvulotomy, is preferred but requires favorable anatomical conditions. Replacement involves implanting a prosthetic valve, which can be biological or mechanical. This procedure is usually performed when the disease is advanced, often necessitating concurrent treatment for tricuspid insufficiency[33,40].

2.6 Mitral valve regurgitation (MR)

Mitral valve insufficiency occurs when the mitral valve leaflets fail to close properly during systole, leading to blood regurgitation from the left ventricle back into the left atrium. This condition is increasingly common due to an aging population and a rise in secondary forms. Mitral insufficiency can be classified into two types based on its onset: acute and chronic[33,42].

2.6.1 Etiology

Mitral insufficiency can be categorized into two types: primary (or organic) and secondary (or functional).

Once upon a time, the main cause of organic mitral insufficiency was rheumatic disease, but this is now rare in the Western world. Current primary causes include degenerative conditions like myxomatous degeneration, calcification of the valve ring, chronic radiation damage, traumatic rupture of chordae tendineae, rupture of papillary muscles, and infective endocarditis. In these cases, anatomical changes in the valvular apparatus lead to regurgitation. The valve ring may dilate, losing its ability to function properly, and alterations can occur in the leaflets, chordae tendineae, and papillary muscles.

In secondary or functional mitral insufficiency, the valvular apparatus is normal. However, the left ventricle is abnormal, appearing dilated and hypofunctional. This dilation affects the relationships among the valve structures, causing the valve ring to stretch and the chordae tendineae to become taut, preventing proper coaptation

of the leaflets. Secondary mitral insufficiency can be further divided into ischemic and non-ischemic types, depending on the underlying cause of ventricular dysfunction. From a therapeutic perspective, distinguishing between these types of dysfunctions is crucial, particularly based on the relationship between the mitral leaflets and the plane of the valve annulus, as outlined in the Carpentier classification:

- Type I insufficiency: the leaflets move normally and remain properly positioned below the valve plane.
- Type II insufficiency: one or both leaflets exhibit excessive movement and are positioned above the valve plane. This is commonly seen in degenerative conditions.
- Type III insufficiency: the leaflets have restricted movement and remain stretched downward, failing to approach the valve plane. This type is typical in secondary forms associated with significant left ventricular dilation.

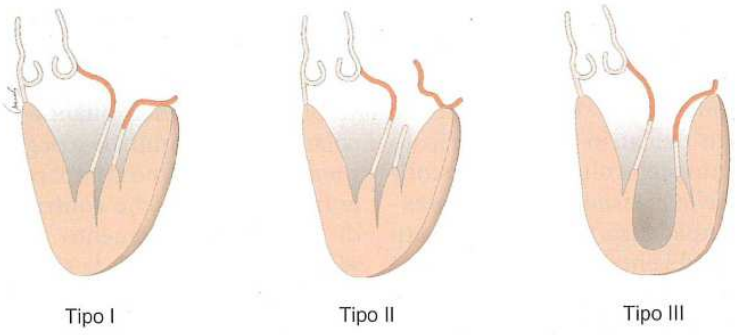

Figure 15 | *Functional classification of mitral regurgitation.*

2.6.2 Pathophysiology

The pathophysiology of mitral insufficiency varies based on its cause (either organic or functional) and its onset (acute or chronic). In organic cases, some blood is ejected into the left atrium during systole and re-enters the ventricle in diastole. This regurgitation (known as "*caput mortuum*") depends on the pressure gradient between the ventricles and the size of the regurgitant orifice. The ventricle responds differently in acute and chronic forms.

In acute mitral insufficiency, the main response is sympathetic stimulation, leading to tachycardia and increased ejection fraction. The pressure in the left atrium rises

due to the volume of regurgitated blood and the atrium's compliance. Since the left atrium is often small in acute cases, it has reduced compliance, which can cause pressure to exceed 60 mmHg. This results in decreased forward blood flow, often leading to low cardiac output and pulmonary edema, or cardiogenic shock.

In chronic mitral insufficiency, the body compensates through eccentric hypertrophy, where the heart muscle thickens to accommodate increased blood volume without raising filling pressures. However, as the ventricle empties more easily, wall thickness doesn't increase proportionately, reducing the mass-to-volume ratio. Over time, the heart's contractility declines, although the ejection fraction remains normal initially. Eventually, end-diastolic volume increases to match regurgitation, while end-systolic volume remains normal or slightly elevated. The myocardium deteriorates due to fibrosis, leading to reduced pumping capacity, increased filling pressures, and ultimately congestive heart failure[43].

In functional forms of mitral insufficiency, the condition arises in an already dilated ventricle, leading to immediate heart failure symptoms, including reduced ejection fraction and pulmonary hypertension. Mitral insufficiency exacerbates the underlying heart disease. When assessing the severity of mitral regurgitation, key parameters include the effective orifice area (EROA), regurgitant volume, and regurgitant fraction. For functional-ischemic causes, an EROA of 0.2 cm^2 and a regurgitant volume of 40 cc indicate severe regurgitation. Other important signs include increased left ventricular and atrial volumes, elevated pulmonary artery pressures, and evidence of regurgitation in the pulmonary veins[33].

	Lieve	Moderata	Moderata/Severa	Severa
Vena contracta (mm)	< 3	3 - 4,9	5 - 6,9	> 7
Area orifizio di rigurgito (cm^2)	< 0,2	02 - 0,29	0,3 - 0,39	> 0,4
Volume di rigurgito (ml)	< 30	30 - 44	45 - 59	> 60
Frazione di rigurgito (%)	< 30	30 - 39	40 - 49	> 50

Figure 16 | *Grades of mitral regurgitation based on echocardiographic parameters*.

2.6.3 Natural history

The natural history of organic mitral insufficiency is long and stable until symptoms appear. Once heart failure has set in, the clinical picture rapidly worsens. Secondary mitral insufficiency starts from a heart that is already failing, and therefore has a generally unfavorable outcome[33].

2.6.4 Treatment

There is essentially no pharmacological treatment for chronic mitral insufficiency. In acute cases, standard heart failure treatments and vasodilators can be beneficial, but in chronic forms, the already low impedance to left ventricular outflow makes further reduction inappropriate[44].

Surgical intervention is indicated when mitral insufficiency is both significant and symptomatic. "Significant" typically means an effective orifice area EROA ≥ 40 mm^2, accompanied by increased left atrial and ventricular dimensions[45]. "Symptomatic" includes any symptoms, especially those related to left atrial hypertension. A functional mitral insufficiency is considered significant if EROA ≥ 20 mm2. However, mitral insufficiency is often asymptomatic. In this case, the indication for surgery is given if there is:

- Left ventricular systolic dysfunction, defined as ejection fraction < 60% and/or end-systolic volume > 45-50 cc/m2.
- Pulmonary hypertension.
- Atrial fibrillation (this is a dubious criterion).

If the ejection fraction < 30% the surgical risk is very high and the surgical choice must be discussed in the heart team and above all with the patient[33].

3. Aortic valve replacement

In this section, we will discuss the types of valves that are implanted and the most performed interventions in patients with aortic valve stenosis, mainly caused by age-related calcific degeneration.

3.1 Type of valves

There are currently several types of valve prostheses, which can be divided into two main groups: mechanical and biological.

3.1.1 Mechanical valve prostheses

All mechanical valves have a similar structure composed of three components:

- Occluder: generally made up of one or more rigid and mobile parts, for example: a ball (in Starr-Edwards prostheses), a disk (in Bjork-Shiley prostheses) or a circular or semicircular "hinged flywheel" (in Medtronic-Hall or St. Jude Medical prostheses). It must be able to open and close without interfering with blood flow and to adapt to pressure differences.
- Housing: where the occluder is inserted.
- Suture ring: this is the base or body of the prosthesis. It is made of a suture ring made of metal or graphite coated with pyrolytic carbon. It represents the connection point of the prosthesis with the recipient's tissues.

The titanium joints that in safety tests guarantee billions of heartbeats, therefore, it is a valve that once implanted potentially lasts a lifetime, unless the organism needs to grow. In reality, fibrotic tissue, called fibrotic pannus, often forms under the valve, which decreases the excursion of the discs (this represents a typical failure mechanism of a mechanical valve). Other times, the prosthesis can coagulate and, therefore, it is important to maintain a certain coagulation index: during the post-operative period the index is maintained through the administration of low molecular weight heparin or through antagonists of the intrinsic pathway, while at home it is maintained through the oral administration of Warfarin (which is nothing more than a poison used for mice that has anticoagulant properties).

Currently 90% of mechanical valves implanted are of the double disk or bileaflet model that allows a hemodynamic profile more similar to the physiological one.

3.1.2 Biological valve prostheses

The biological valve prostheses are classified based on the biological tissue they are made of:

- Autografts: heart valve taken from the patient himself.
- Homografts (or allografts): human heart valve removed postmortem.
- Hetergrafts (or xenografts): heart valve taken from non-human species (bovine or porcine).

The valve prostheses that are implanted in a semilunar or atrioventricular position have the same characteristics in terms of both shape and space: they have 3 valve commissures and 3 cusps that make up the valve flaps. They do not last as long as mechanical prostheses, but on the other hand they do not require the intake of anticoagulant drugs. Generally, foreign tissue causes rejection, however, since the tissue is acellular, rejection will not occur in this type of valve replacement. However, chronic rejection will occur, which consists of calcific degeneration. The biological prosthesis is usually implanted in elderly people. Above 65 years of age it is the ideal prosthesis because the average life of a valve prosthesis is inversely proportional to calcium metabolism which, in turn, is inversely proportional to age (the lower the age, the higher the calcium metabolism).

A B

Figure 17 | *(A) Medtronic Avalus™ biological aortic valve, in bovine pericardium; (B) LivaNova Carbomedics™ mechanical aortic valve, in pyrolytic carbon.*

3.2 Valve Excision and Débridement

The surgery is performed with the patient on cardiopulmonary bypass using a single venous cannula, allowing oxygenated blood to be returned to the ascending aorta. The aorta is occluded, and a hypothermic cardioplegic solution protects the heart muscle from ischemic injury. Retrograde perfusion via a catheter in the coronary sinus is the preferred method, but the coronary arteries can also be perfused antegrade through a cannula in the aorta, either to perfuse the aortic root or, in cases of aortic valve regurgitation, directly into the coronary ostia using specific coronary perfusion cannulae[46].

A transverse incision is made in the ascending aorta, extending into the noncoronary sinus of Valsalva. This is the standard incision for aortic valve surgeries. An alternative incision can facilitate the implantation of aortic valve bioprostheses or aortic homografts in the aortic root (Figure 18 A).

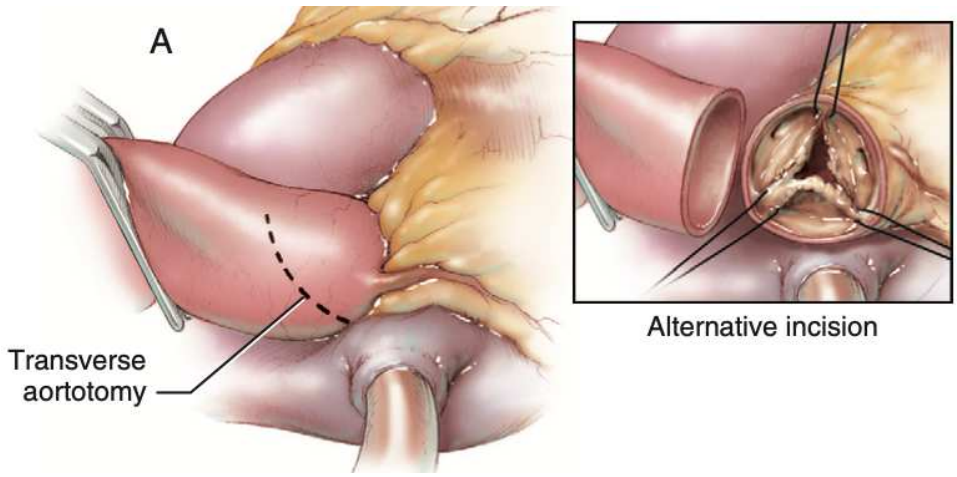

Figure 18 | *Transverse incision is made in the ascending aorta.*

The aorta is completely cut above the sinotubular junction, while leaving the noncoronary sinus intact. To improve exposure of the aortic root, traction sutures are placed at the apex of each commissure of the aortic valve. These sutures help rotate the aortic root downwards, providing excellent visibility. Although this approach requires reattaching the aorta after the valve replacement, the suture line is more secure than making incisions deep into the noncoronary sinus.

The excision of the aortic valve starts at the commissure between the right and noncoronary sinuses. This commissure is removed from the aortic wall, and the

right coronary cusp is excised at the annulus. Careful excision of the valve cusp is important, especially to remove any calcification (Figure 19 B).

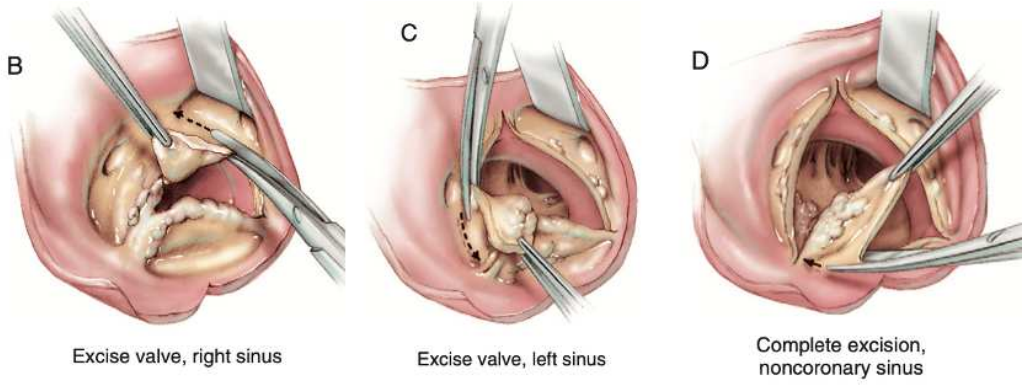

Figure 19 | *Excision of the aortic valve.*

The commissure between the left and right coronary cusps is removed from the aortic wall, and the left coronary cusp is excised (Figure 19 C). The noncoronary cusp is then excised towards the commissure between the left and noncoronary cusps, completing the excision posteriorly (Figure 19 D). Any remaining calcium deposits on the aortic annulus are carefully removed. A vascular forceps is used to grasp and twist away the calcium pieces, preserving the connective tissue of the aortic annulus and preventing excessive removal or perforation of the aorta. During this part of the procedure, a small piece of gauze is placed in the left ventricular outflow tract below the aortic annulus to catch any calcium fragments that may fall during cleaning. With patience, all calcium deposits can be removed to ensure better seating and healing of the valve prosthesis (Figure 20 E). Traction stitches are placed at the sinotubular junction above each commissure and pulled tightly to maximize exposure of the aortic annulus. The annulus is then calibrated, and an appropriately sized prosthesis is selected for valve replacement (Figure 20 F).

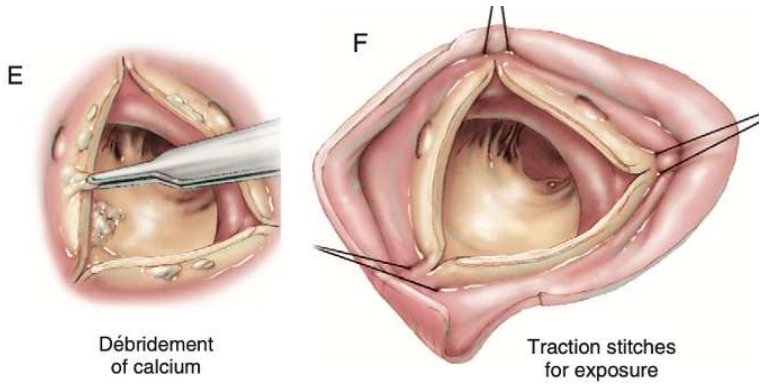

Figure 20 | *Débridement the aortic valve and traction stitches.*

3.3 Continuous Suture Technique

The continuous suture technique for aortic valve replacement offers several advantages over the standard pledget-reinforced mattress suture technique. It allows for a larger prosthesis to fit in the aortic outflow tract since the tissues are not compressed, as they are with mattress sutures. This technique also enables uniform tension on each suture and reduces the number of knots, which can be potential sites for clot formation. Retraction stitches are placed just above the commissures, dividing the aortic annulus into three segments[46].

During the procedure, the annulus is further divided at the midpoint between the commissures, creating six subsegments. An initial mattress stitch is placed at the center of the sinus of Valsalva, through the aortic annulus, and brought through the sewing ring of the prosthesis. The prosthetic valve is held away from the annulus. Three additional stitches are then placed between the initial stitch and the commissure on each side of the sinus. The final stitch at each end is secured to the drapes with a hemostat (Figure 21 A).

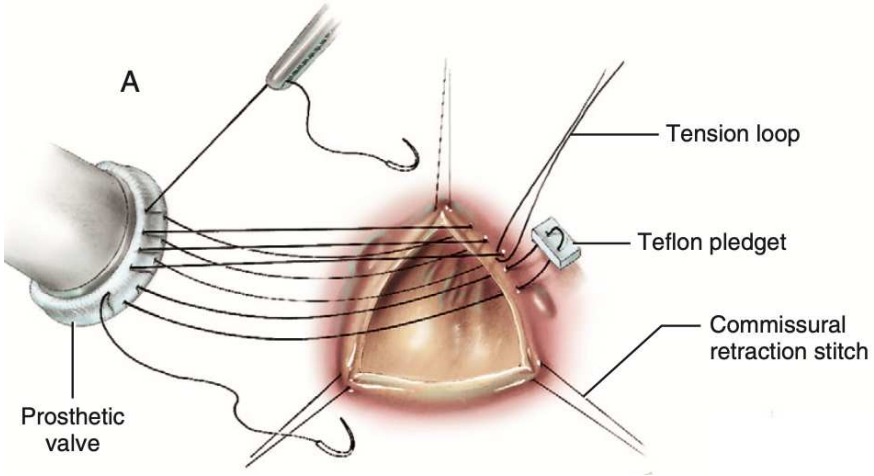

Figure 21 | *Continuous stitches connect the prosthetic valve with the aortic annulus.*

Sutures in the right coronary annulus are placed from the center toward the commissures in the first and second subsegments. The initial stitch in the left coronary sinus passes through the sewing ring of the prosthesis, positioned opposite the last stitch of the second subsegment. The surgeon then works from the center to the commissures in the left coronary sinus, attaching the third and fourth subsegments to the prosthesis. Last sutures are placed in the fifth and sixth subsegments of the noncoronary sinus (Figure 22 B).

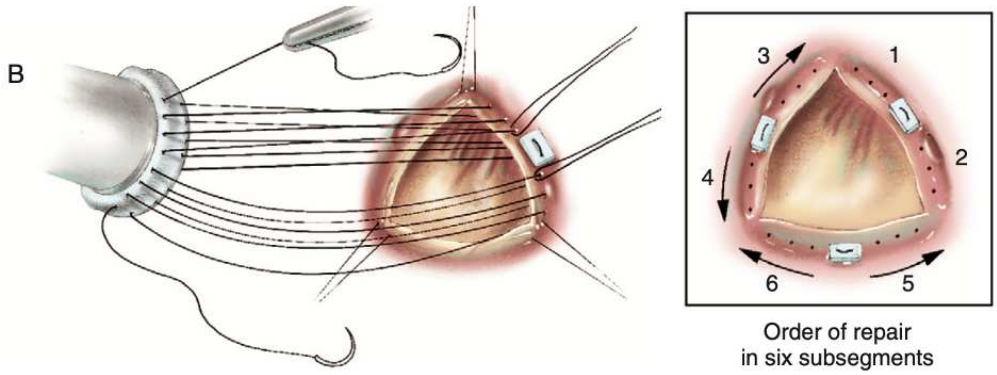

Figure 22 | *Order in which the stitches are placed.*

Traction is applied to secure the prosthesis into the aortic valve annulus. This is done by pulling on the loop sutures near the pledget to seat it firmly (Figure 23 C). The silk traction suture loops are removed one by one, and the surgeon ensures there are no loose sutures beneath the aortic prosthesis in the left ventricle's outflow tract. This traction technique, developed by Dr. Russell M. Nelson, simplifies the process of positioning the prosthesis and tightening the continuous sutures (Figure 23 D).

A final check confirms that the sewing ring of the aortic prosthesis is properly aligned with the annulus. Special attention is given to the pledget's placement, ensuring it is positioned above the annulus where stress is greatest, deep in the center of the sinus of Valsalva. The suture ends are then joined by a knot at the three commissures (Figure 23 E).

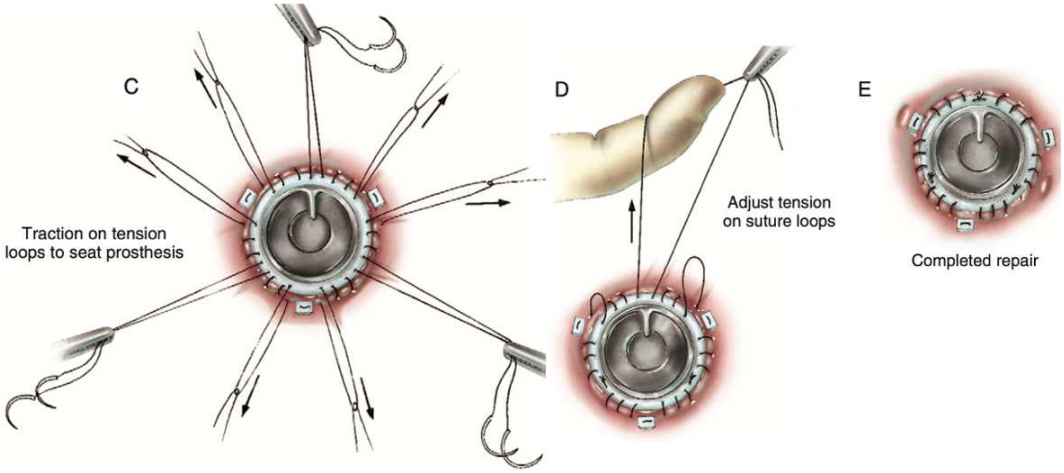

Figure 23 | *Implantation and suturing of the prosthetic aortic valve.*

3.4 Interrupted Suture Technique

The interrupted suture technique is the standard method for aortic valve replacement. It provides strong attachment of the prosthetic valve and minimizes the risk of perivalvular leaks[46].

A double-needle suture made of synthetic material, with a compressed Teflon pledget in the center, is used for the procedure. Using sutures in two different colors (green or blue and white) helps the surgical team identify the pairs easily, allowing them to group the sutures for each annulus repair under the sinuses of Valsalva.

The surgeon begins placing mattress stitches through the aortic valve annulus at the commissure between the left and right coronary cusps. Stitches are then inserted into the right coronary annulus in a clockwise direction, moving toward the commissure between the right and noncoronary sinuses. The stitches are placed closely together, ensuring that the space along the aortic annulus is filled beneath the pledget of each mattress stitch (Figure 24 A).

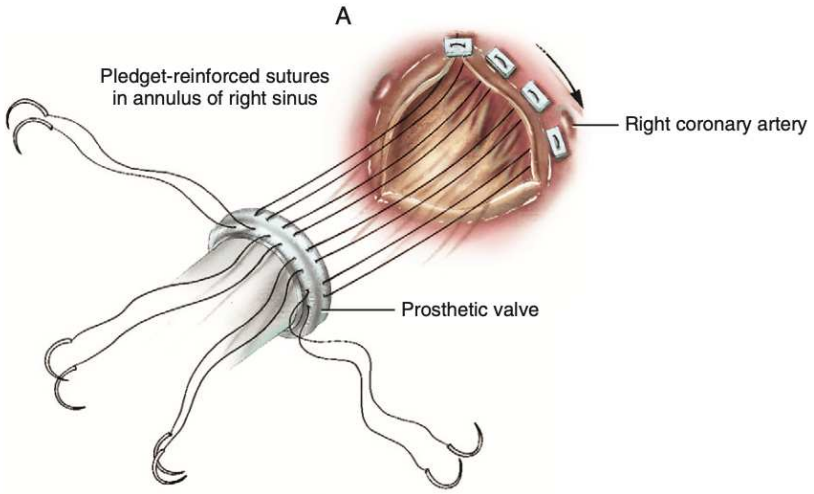

Figure 24 | *Interrupted stitches connect the prosthetic valve with the aortic annulus.*

The annulus of the left coronary sinus of Valsalva is brought together with the aortic valve prosthesis, using sutures placed in a counterclockwise direction, starting at the commissure between the left and right coronary cusps (Figure 25 B). Next, the annulus of the noncoronary sinus of Valsalva is connected to the valve prosthesis by working clockwise from the commissure between the right and noncoronary cusps to the commissure between the left and noncoronary cusps. The needles are passed through the annulus. Finally, the three groups of sutures are pulled tightly,

allowing the prosthesis to be smoothly positioned over the suture loops into the aortic annulus (Figure 25 C).

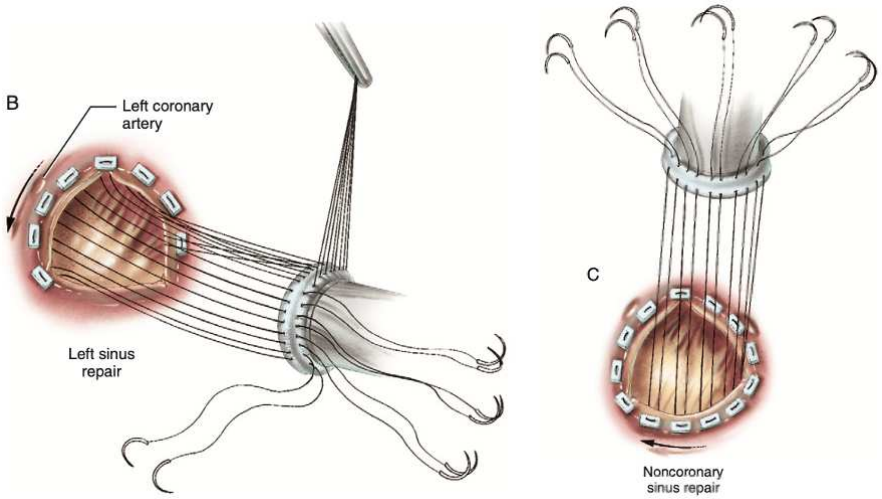

Figure 25 | *Implantation of the prosthetic aortic valve.*

The sutures are organized and tied in a specific sequence. First, the sutures in the noncoronary sinus are tied in a counterclockwise direction. The first suture in the left coronary sinus, located nearest to the commissure with the right coronary cusp, is tied directly across from the noncoronary sutures to ensure a secure fit for the prosthesis. Next, the sutures in the left coronary sinus are tied in a counterclockwise manner. Finally, the sutures in the right sinus are secured in a clockwise direction (Figure 26 D). In cases of a small aortic annulus, an alternative technique is used for the pledget-reinforced stitches. Here, the pledgets are placed below the annulus in the left ventricular outflow tract. A mattress stitch with a central pledget is created using a double-needle suture, which is passed from beneath the annulus and up through the prosthesis. This allows for a larger prosthesis to be securely positioned above the annulus (Figure 26 E).

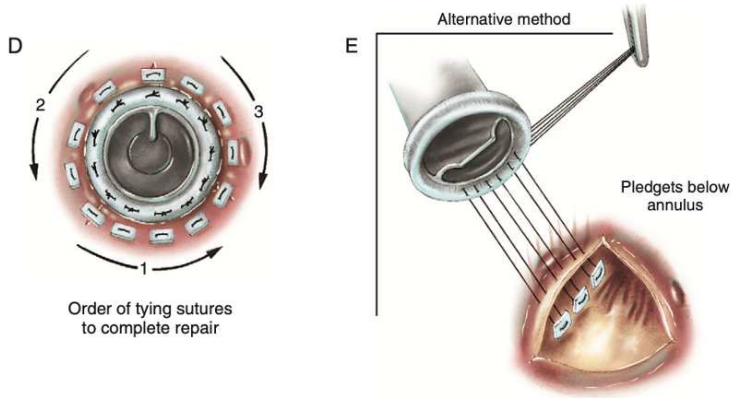

Figure 26 | *Order of sutures in the interrupted suture technique.*

3.5 Stentless Porcine Xenograft: Subcoronary Valve Replacement

Glutaraldehyde-preserved porcine xenograft aortic valves are commonly used for aortic valve replacement. These valves can either be stented, allowing for standard continuous or interrupted suturing techniques, or stentless, relying on the patient's aortic root for support. Stentless xenografts offer significant hemodynamic advantages, especially in patients with smaller valve diameters, as they provide more flexibility and potentially longer durability[46].

Various manufacturers produce stentless porcine xenograft aortic valves, each providing sizers to help select the appropriate valve size. During preparation, the sinus aorta is removed from the graft in the right and left sinuses of Valsalva. The lower edge of the graft's aortic root is covered with Dacron fabric to facilitate implantation and prevent graft shrinkage when the surrounding myocardium is absorbed (Figure 27 A). The aortic valve is excised as usual, ensuring all calcifications are cleared from the aortic annulus. The suturing begins at the interleaflet triangle below the commissure between the left and right sinuses, penetrating the Dacron fabric for secure attachment (Figure 27 B).

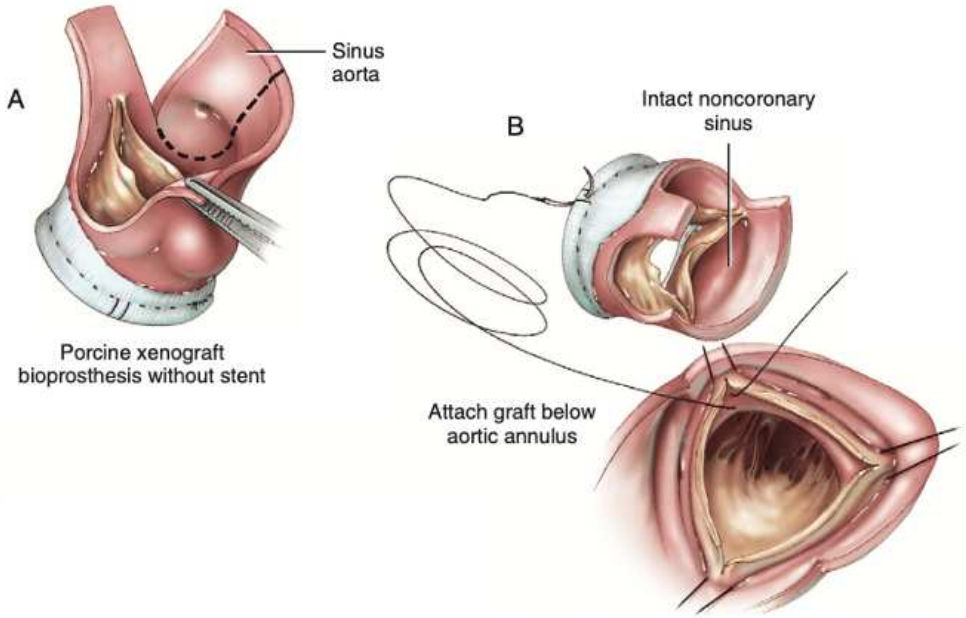

Figure 27 | *Porcine aortic valve implantation method.*

The valve is kept away from the annulus while the suture loops are placed. A heavy silk suture is threaded around every third loop to serve as a tension-adjusting suture

(Figure 28 C). Suturing begins below the right sinus and moves toward the commissure between the right and noncoronary sinuses, then to the left coronary sinus below the commissure with the noncoronary sinus. Tension loops are added at every third stitch. The valve is then seated in the aortic root by sequentially pulling on the tension loops, bringing the valve fabric closer to the aortic annulus (Figure 28 D).

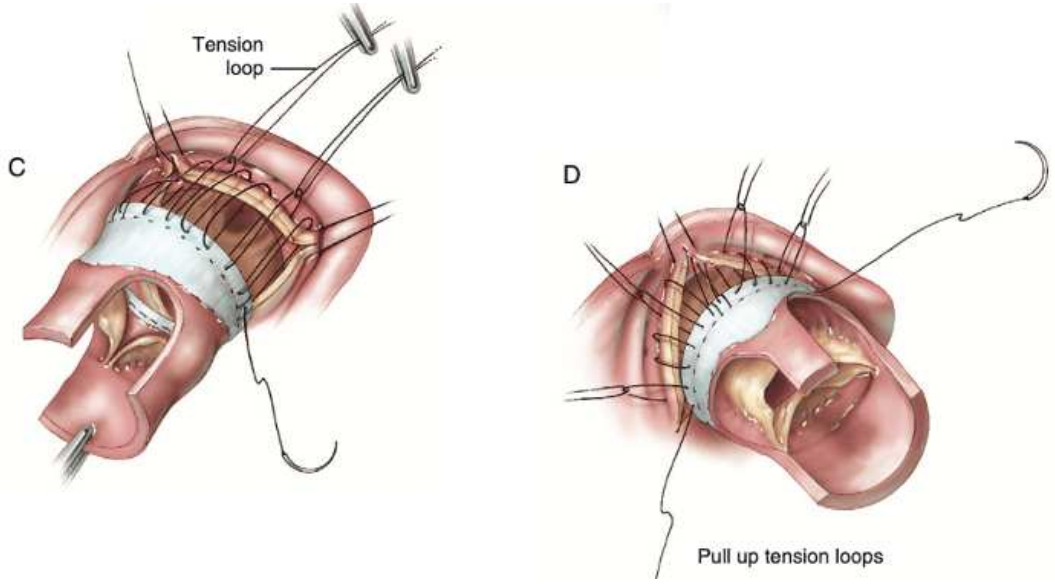

Figure 28 | *Suture of the porcine aortic valve to the aortic annulus.*

The tension loops are removed one by one after final adjustments to the proximal suture line below the left and right coronary sinuses (Figure 29 E). The noncoronary sinus repair follows next (Figure 29 F). The graft's sinus aorta is attached to the patient's sinus aorta using continuous stitches. A mattress stitch is placed in the host's sinus aorta just below the coronary ostia. This step differs from the aortic allograft technique because glutaraldehyde-preserved xenograft tissue is stiff and maintains its shape, requiring careful approximation to the host aorta without distortion. Allograft tissue, in contrast, can be easily folded. The suture line is positioned close to the coronary ostia to ensure a proper fit of the xenograft tissues. Special attention is given to the right coronary sinus of the graft, ensuring the commissure between the right and left sinuses is accurately located to prevent distortion. Suturing continues to the top of the remaining two commissures, leaving the intact noncoronary sinus of the graft to be repaired later (Figure 29 G). This technique emphasizes the close placement of the suture line to the right coronary

ostium, which is a unique feature of the stentless xenograft technique (Figure 29 H). If there is enough space in the sinus to accommodate the graft without distortion, the noncoronary sinus can be repaired through direct closure of the host aortotomy.

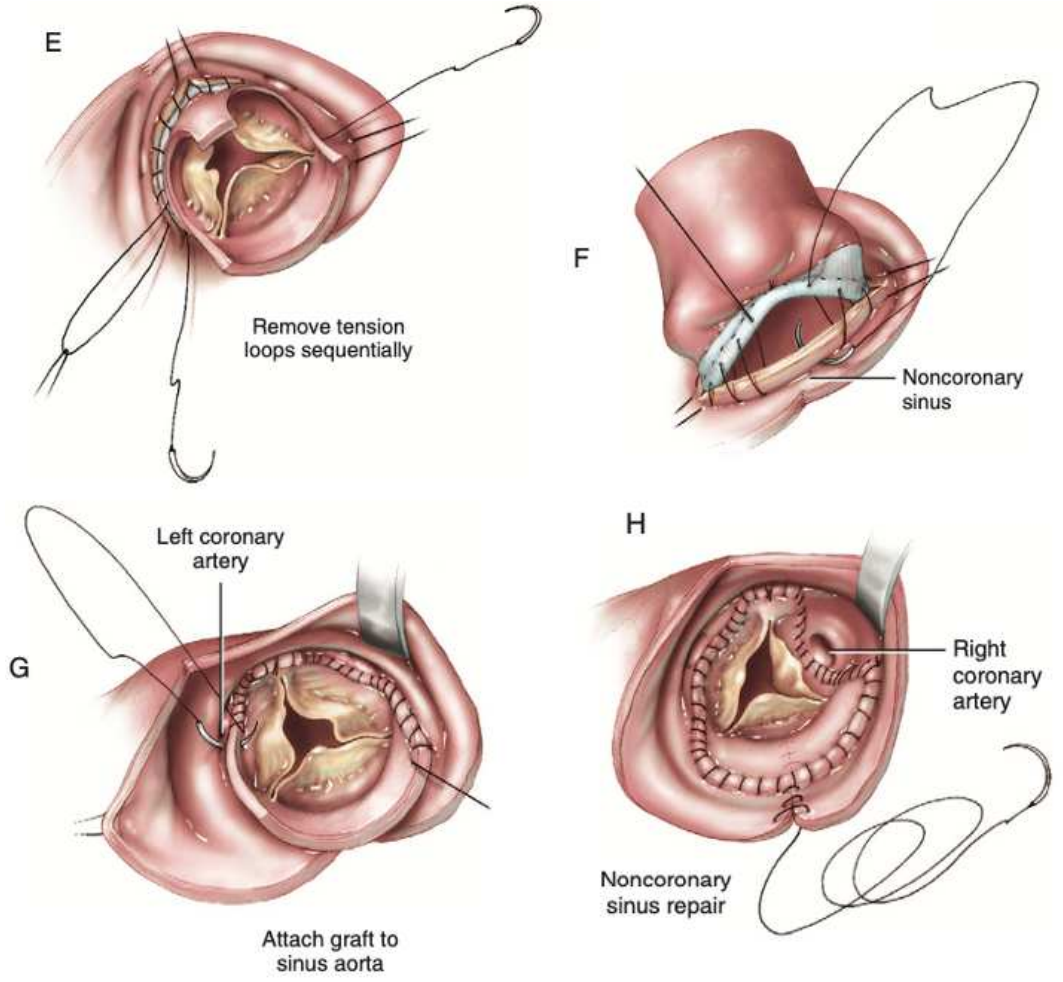

Figure 29 | *Valve replacement with porcine valve completed.*

Operative photograph of a completed subcoronary aortic valve replacement with a porcine xenograft. After considerable experience, it became apparent that the preferred approach to the aortic valve is through the divided aorta and the intact aortic root. This method provides excellent exposure while preserving the noncoronary sinus. The xenograft fits into the intact aortic root in nearly all cases, allowing the noncoronary sinus aorta to be trimmed at the level of the host aorta. This enables direct approximation by continuous suture at the edges. The aortic anastomosis is secure and reinforces the repair of the noncoronary sinus[46].

4. 3D technology

4.1 3D segmentation and Computer-Aided Design (CAD)

Medical images are usually represented in grayscale, a form of black and white or gray monochrome, composed exclusively of shades of gray. The contrast varies from black at the weakest intensity to white at the strongest. To fully understand how these images are constructed, we must start with the concept of radiodensity. "Radiodense" substances are those that do not allow X-rays or similar radiation to pass through, while those that allow passage are called "radiolucent." The Hounsfield scale is a scale of units used to quantitatively describe radiodensity.

To generate a 3D model from medical imaging, a suitable technique is tomographic imaging (CT, MRI), in which a contiguous series of image slices are captured non-invasively. Each slice represents a cross-section of the scanned structure with a particular thickness[47]. Slice thickness is an important factor influencing image quality. To achieve a 3D reconstruction of the desired structure, the region of interest (ROI) must be identified in each slice of the image sequence and then interpolated. Consequently, the ability to reconstruct smaller structures depends on the image resolution, which is determined by the slice thickness: thinner slices result in higher resolution. The thickness is determined by the collimator settings, and its values are set by the operator based on the clinical examination requirements, typically ranging from 0.625 to 10 mm[48, 49]. CT scans commonly utilize slice thicknesses within this range to strike a balance between spatial resolution (better in thin slices) and scan time for a particular area (shorter in thicker slices)[50, 49]. In thin slices, the partial volume artifact decreases while the patient dose, image noise, and scan time increase. Conversely, the thicker the slices, the more photons are available, improving the signal-to-noise ratio (SNR)[49, 51, 52]. For cardiac segmentations, a minimum thickness of 1.5 mm is typically required, with an optimal thickness ranging from 0.5 to 1 mm.

The pixels within each image slice are represented by scalar values that can be interpreted as intensity values[47]. Therefore, the difference in radiodensity allows us to distinguish different regions within a single slice. The method of digital image processing that enables this distinction is called segmentation. Segmentation is the

process of assigning a label to each pixel in an image. Pixels with the same label share certain characteristics, such as color, intensity, or texture. More specifically, in CT image processing, the X-ray absorption rate is measured and normalized to the water absorption rate, expressed in Hounsfield units (HU). Through image segmentation, all pixels with the same HU can be selected, and with the help of interpolation algorithms, a 3D reconstruction can be obtained[47].

There are many techniques for segmenting grayscale images, and regardless of the method, the goal is always to find all regions of an image within a certain range of gray values. This method allows us to select every pixel within a certain range of Hounsfield units (HU) in a CT scan and isolate a specific region of interest (ROI). Typically, pixels with the same HU value belong to regions that are anatomically continuous in the CT scan, allowing us to isolate a single anatomical component. The same principle cannot be applied to MRI scans, as the gray levels are highly dependent on the sequence and the type of weighting applied. However, with bright blood sequences, the result is quite similar to normal contrast CT scans and can be processed in the same way.

For example, two of the most widely used segmentation methods in the medical field are the thresholding method and histogram-based methods.

The simplest segmentation method that can be applied to medical imaging is the thresholding method. This method is based on a threshold value, which transforms a grayscale image into a binary image. The key to this method is selecting the correct threshold value to achieve good segmentation. There are also so-called "adaptive thresholds," which allow for different thresholds in different regions of the image.

Histogram-based methods are very useful in medical imaging. In this technique, a histogram of all the pixels in the image is calculated, and the peaks and valleys in the histogram are used to locate clusters in the image. Each peak in the histogram represents a cluster of pixels with similar HU values. For optimal segmentation, the threshold should be set in a valley, ensuring maximum separation between the selected pixels and the rest.

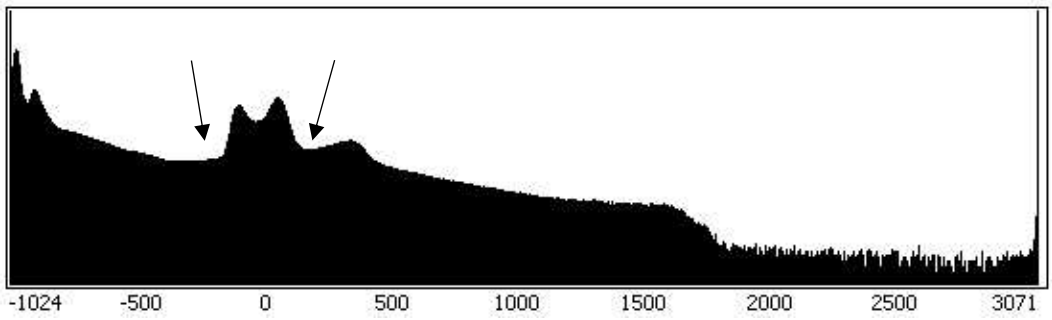

Figure 30 | *Histogram-based methods analyze the distribution of pixel densities by showing the relative frequency of pixels with varying intensities. The horizontal axis is measured in Hounsfield Units (HU). Each peak represents a cluster of pixels with similar HU values. For optimal segmentation, the threshold should be placed in the valley (indicated by the arrow) to achieve maximum separation between the clusters*.

Computer-aided design (CAD) is the use of software to facilitate the creation, modification, analysis, or optimization of a design. It is a technology that enables engineers and architects to design and produce technical documentation in 2D or 3D using modeling software. After segmenting the image, this post-processing step is required using CAD software. There are several CAD programs; in our case, CAD software such as Meshmixer™ (Autodesk Inc, San Rafael, CA, USA) was mainly used to refine the heart model for the printing process by correcting small errors, smoothing surfaces, cutting models, and defining wall thickness.

There are several ways to mathematically describe a 3D object, and one of the most common is through the use of triangular meshes. In this approach, an object is represented as a three-dimensional surface divided into small two-dimensional triangles formed by three elements: vertices, edges, and triangles.

4.2 3D Printing

Additive manufacturing (AM), or 3D printing technologies, creates three-dimensional parts from CAD models by adding multiple overlapping layers of material until the piece is complete. This technology was developed in 1986 by Chuck Hull, who invented and patented the first form of 3D printing, known as stereolithography. Additive printing technologies have been around since the 1980s and have had a significant impact on the biomedical field from the start, with the first documented uses in dentistry and maxillofacial surgery as early as 1994.

However, this sector gained significant attention only after 2010, thanks to the development of new materials, improved software, and reduced costs, making it accessible to a wide range of applications. The main areas of medicine in which 3D printing is currently applied and researched include dentistry, regenerative medicine, tissue engineering, drug production, prosthesis design, and the production of custom-made devices and anatomical models for teaching or preoperative planning[53, 54].

The workflow of the 3D printing process is illustrated in Figure 31. First, the CAD model is created, followed by the generation of a standard tessellation language (.stl) file from the CAD model. The .stl file is then imported into a model slicing software, in our case PreForm™ (Formlabs Inc., Somerville, MA, USA), which creates a tool path for the 3D printer. At this stage, the 3D model is translated into 2D slices containing the cross-sectional information.

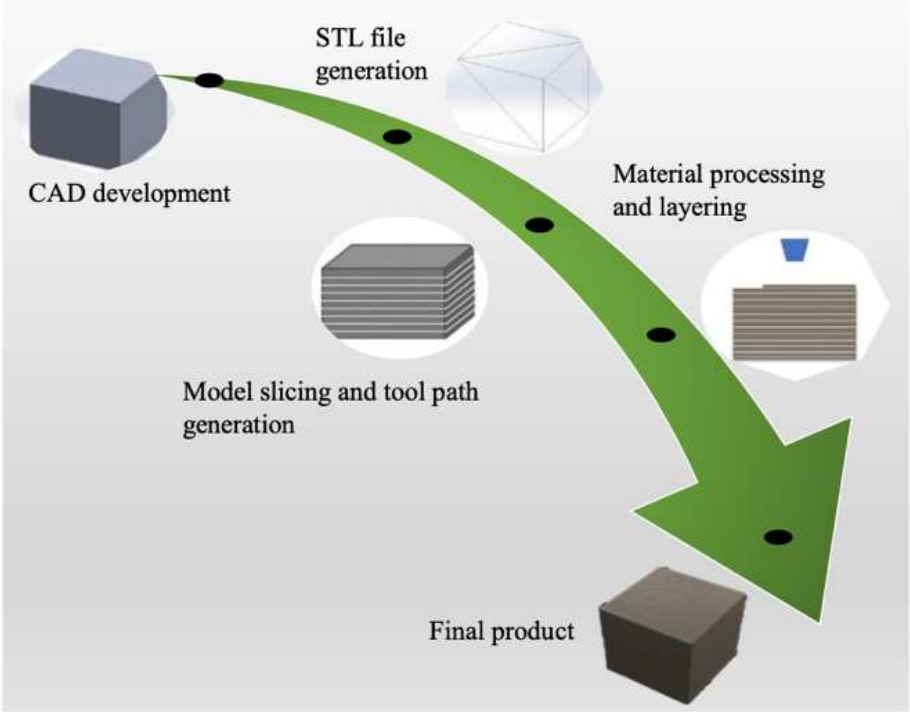

Figure 31 | *3D printing process workflow*[55].

A variety of additive manufacturing (AM) methods are available to 3D print a wide range of materials. The additive manufacturing process can be divided into three categories based on the type of base material used: solid-based, powder-based, and liquid-based. Our team works with liquid-based materials.

The 3D printers owned by the Department of Cardiac, Thoracic, Vascular, and Public Health Sciences at the University of Padua include the Formlabs Form2™, Formlabs Form3L™ (Formlabs Inc., Somerville, MA, USA), and the Sisma Everes Uno™ (Sisma SpA, Vicenza, VI, Italy). All these printers use a technology based on vat-photopolymerization, with the main difference being the light source.

The Formlabs™ Form3L™ uses stereolithography (SLA) technology and features a print engine called Low Force Stereolithography (LFS)™, a type of short-wavelength laser introduced by Formlabs in 2019. In simple terms, the Form3L™ consists of a container filled with liquid resin, a movable lifting platform inside the container, an ultraviolet laser with beam-focusing optics, and a system of deflector mirrors to control two lasers. Using the photopolymerization technique, the printer transforms the liquid resin into a high-precision model by adding each thin layer of resin onto the previous one. The process starts from the edges of the layer and moves inward (unlike DLP printers, which solidify an entire layer at once). When the layer is cured, the lifting platform descends a defined distance, typically a layer thickness of 0.1–0.5 mm, immersing the model into the liquid resin. A sweeper smooths the surface and levels the resin. Then, a new layer of liquid is applied, and the process continues, building the model layer by layer.

The polycarbonate resin tank holds up to 1 liter of resin, and the resin level is automatically maintained. By simply inserting two resin cartridges, the machine automatically refills the tank. The bottom of the tank is flexible, allowing the polymerized part to detach, drastically reducing the forces exerted on the parts during the printing process. The build platform measures 33.5 × 20 × 32 cm, with a print area of 670 cm^2. It moves along the Z-axis, and its movement determines the thickness of each layer, which can range from 25 to 300 microns.

The core of the printer is represented by its two Light Processing Units (LPUs). These units are characterized by their optical architecture, which includes components such as lasers, beam splitters, modulators, and photodetectors. These elements work together to manipulate and control the laser beams. The proper functioning of the LPUs is essential for the efficiency and performance of the printer, as they are responsible for the synchronization of light waves, a property called coherence. Each LPU contains a 405 nm violet laser (maximum power 250 mW) with a beam width of 85 microns. The printer has two lasers, with each laser

responsible for photopolymerizing the resin on half of the build platform. Therefore, it is crucial that the lasers work in sync, which depends on the correct functioning of the two LPUs.

Before printing, the .stl file must be loaded into PreForm™, software that allows you to adjust settings such as resin type, layer thickness, and support structure layout. The software also automatically generates supports to prevent hanging or delicate parts from collapsing during the printing process, though these supports can still be manually modified.

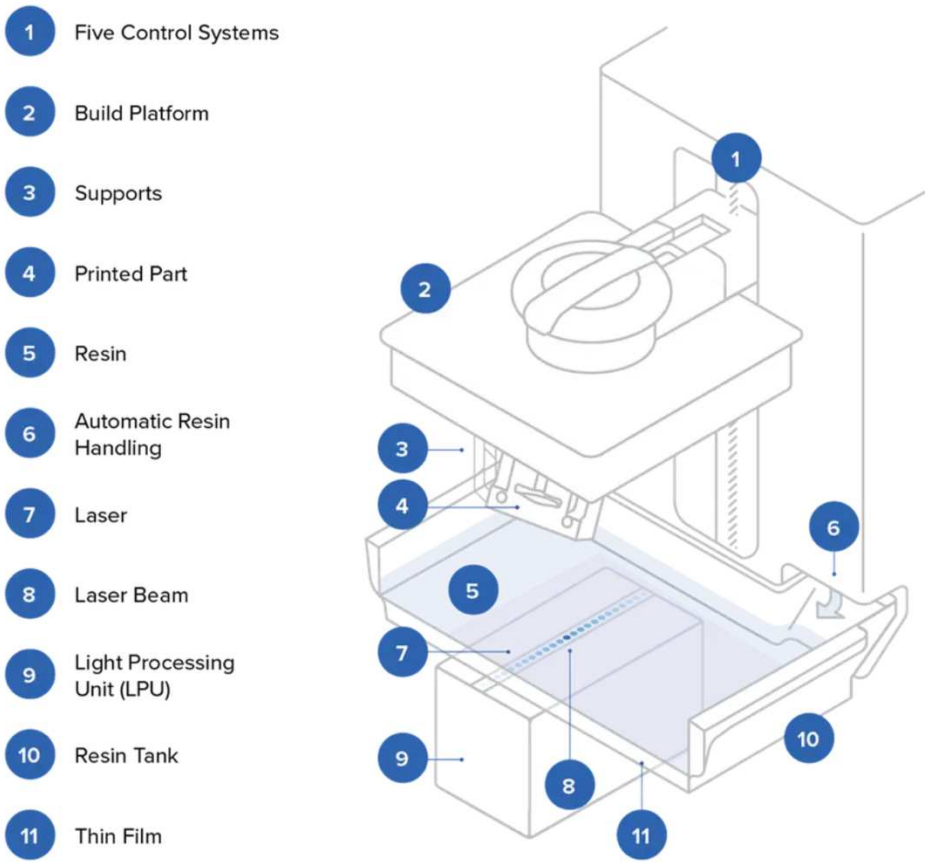

Figure 32 | *Summary diagram of the components of a stereolithography (SLA) printer.*

The Sisma™ Everes Uno™ printer uses technology based on digital light processing (DLP). DLP 3D printers utilize a light source (UV LED with high power at 405 nm) that reflects onto a projector called a Digital Micromirror Device (DMD), a microchip covered with millions of mirrors that move independently and accurately represent each pixel of the image. The coordinates at which the liquid resin is polymerized within each layer are determined by the rapid switching of

these tiny mirrors between lenses that direct the light toward the bottom of the resin tank. Since the projector functions as a digital screen, the image of each layer is composed of square pixels, resulting in the creation of a three-dimensional layer made up of small rectangular cubes called voxels. The printer has a print surface of 124.8 × 70.2 mm, and its projector can polymerize an entire layer at once. However, the resolution of DLP 3D printers decreases as the print volume increases because projectors with significantly more pixels are not yet available. The accuracy of DLP printers is often limited by pixel distortion at the edges of the printed part, where micromirror devices must project light further from the light source.

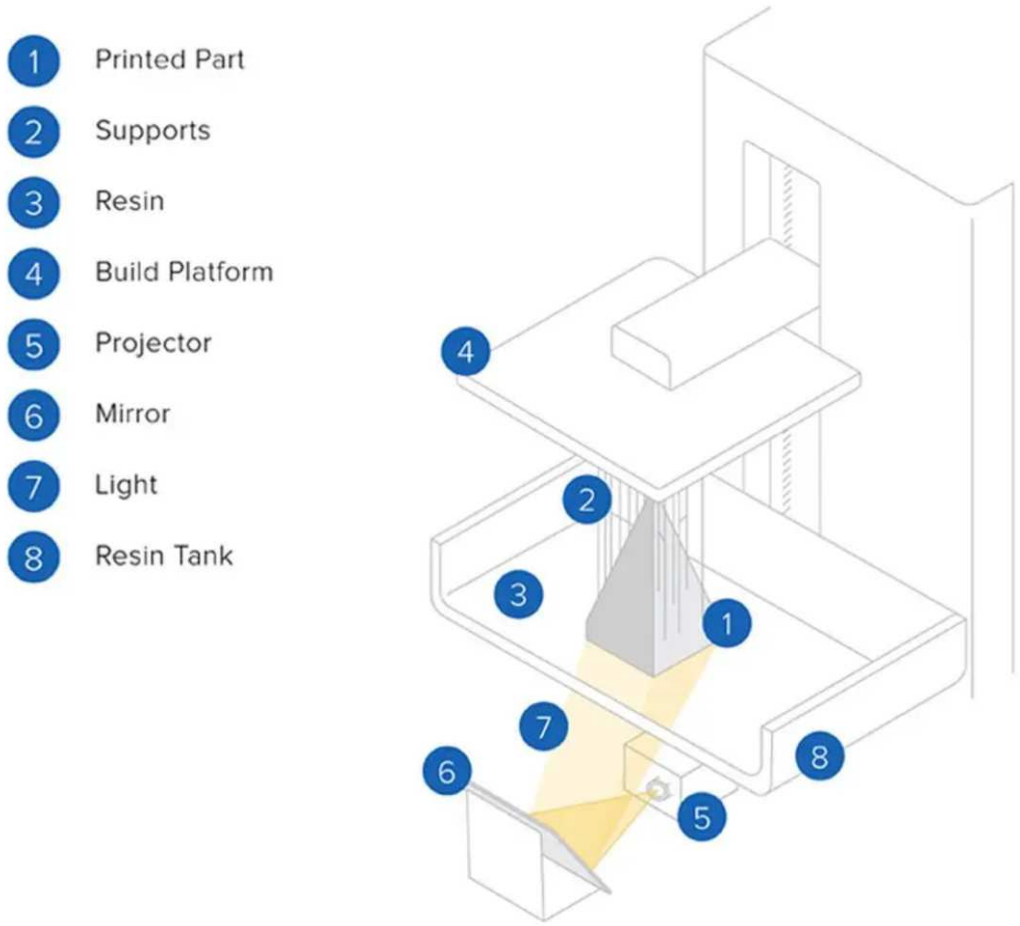

Figure 33 | *Summary diagram of the components of a digital light processing (DLP) printer.*

Figure 34 | (A) *our SLA 3D printer, a FormLabs™ Form3L™*; (B) *our DLP 3D printer, a Sisma™ Everes Uno™.*

Photopolymers are special resins used in all Vat-photopolymerization techniques as printing materials. When exposed to specific wavelengths of light, these photopolymers undergo a process called photopolymerization, in which they bond together, transforming from a liquid into a solid. However, photopolymers tend to degrade or deform over time. To address this issue, a post-curing process is performed after printing. This process includes a solvent wash to remove any unpolymerized resin, followed by a photothermal treatment to complete the polymerization and enhance the printed object's mechanical properties and durability.

4.3 3D Printing Applications

3D printing in the medical field currently finds application in four main categories:

- **Diagnostic tool**: in some complex cases, realistic 3D models can be much more effective than standard 2D images. This is very helpful especially with congenital heart disease. In addition to a correct diagnosis, prenatal and postnatal counseling is fundamental to help parents understand the

congenital heart disease of the fetus, making them more aware of the condition and of all procedures needed after birth.

Figure 35 | *Example of a 3D printed TOF model made with Clear Resin™.*

- **Surgical planning and training**: in very complex surgeries, patient-specific anatomical models can help the surgical team in morphological understanding and surgical planning. 3D printed models reduce operating time and radiological risk, in fact, they can also be used to verifying the compatibility of the size and shape of the device with the specific anatomy of the patient. Surgeons can leverage patient-specific 3D models to meticulously plan complex procedures, exploring various surgical techniques and potential complications in a risk-free virtual environment. This not only improves surgical precision but also helps reduce potential errors. Some studies that demonstrate how surgeons who trained with a 3D model for a specific procedure before actually doing it on the patient have better skills and result in comparison to others who didn't have this opportunity[58]. Furthermore, in 2021 a surgical simulator called 'TrainHeart' (deposit number IT102021000031058) was developed and patent- ed under

the aegis of the University of Padua with the aim of reproducing the operating field and the position of the surgeon and the different surgical accesses for the treatment of congenital and acquired heart disease[59].

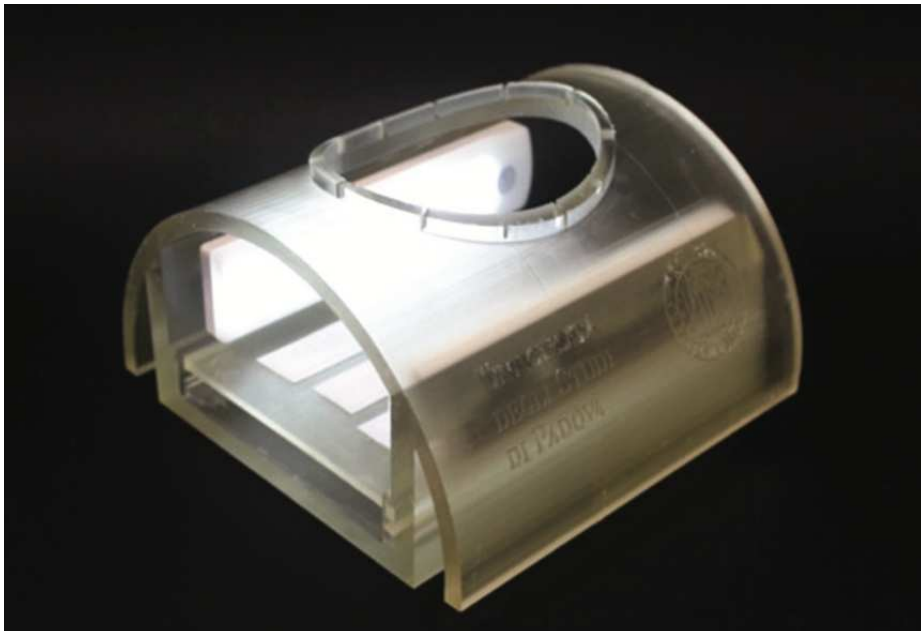

Figure 36 | *3D-printed surgical simulator (TrainHeart).*

- **Custom device manufacturing**: 3D printed models can be used as templates to create devices, test them in a patient-specific environment, or even print them directly. For example, it is possible to produce tissue scaffolds in relatively short times. These scaffolds are used in transplant studies, tissue and disease research.

- **Interactive teaching tool**: numerous studies have demonstrated the great educational potential of 3D printed models. 3D model-based training has improved the understanding of anatomical structures because the models provide better spatial and structural visualization without the drawbacks of rarity, biological risks, or perishability. Also, the Augmented reality (AR) and Virtual Reality (VR) are utilized in our center for teaching purposes for both undergraduate and cardiac surgery/cardiology residents. In our center, we developed in 2021 an app called “Congenital heARts” which contains 50 CHD heart models divided into three categories: Preoperative anatomy (30 models), Status post-surgery (10 models), and fetal (10 models). This

app allows all users to explore the anatomy of a specific heart visualizing the model in the smartphone or tablet or using AR.

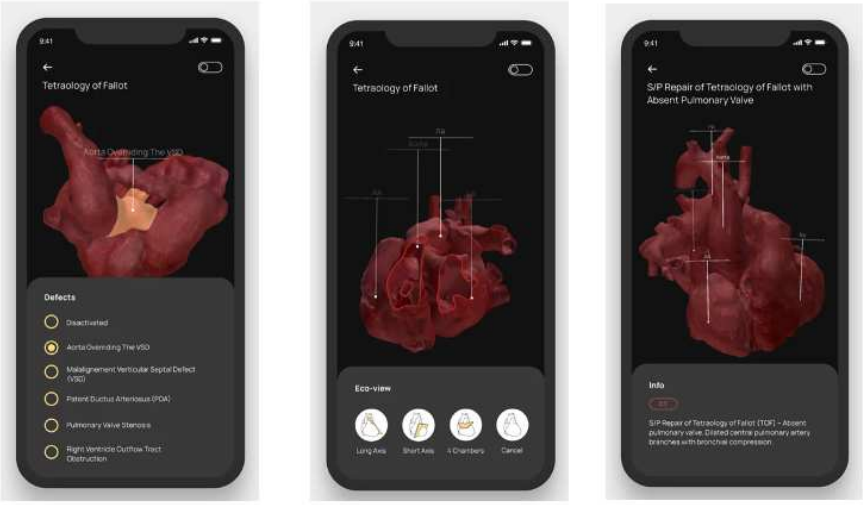

Figure 37 | *Some of the "Congenital heARts" app features*.

In our cardiac surgery center, the use of 3D technology is highly developed and is used in all the areas listed above. In addition, the proposal for the construction of a Regional Center for 3D Reconstruction in the Clinical Setting is in the approval phase. This center aims not only to involve different operating units of the Company, but also to open the doors to collaboration between various U.O.C. in the hospital centers of the Veneto region. This collaboration will allow the hospital centers to access the services offered by the laboratory for clinical and medical research purposes, thus promoting innovation and development in the field of diagnostics and patient care in the region. All departments can access this center and therefore the reconstruction of detailed anatomical models can be addressed and standardized. The 3D Laboratory will also offer opportunities for medical research, such as studies of new surgical techniques. The 3D center is based on the model of the 3D centers present at the Sick Children's Hospital (SickKids) in Toronto with which our unit has already been collaborating for years.

II. AIM OF THE THESIS

5. Rationale of the study

The traditional educational approach relies on medical imaging data, such as CT, MRI, and echocardiography, along with textbooks. However, this method can be challenging for medical students to conceptualize and visualize. Randomized controlled trials have shown that trainees provided with 3D images were significantly better at identifying key anatomical features and responded more quickly compared to those using 2D images across various specialties[60]. Additionally, several studies have detailed the broad potential of 3D imaging[61]. This evidence paves the way for a new teaching method for medical students, while also offering young surgeons an effective tool for surgical training.

Several studies conducted in the urological field have demonstrated that simulations using models that provide a realistic suturing experience can significantly enhance surgical skills[62]. In our unit, the development of the training program in cardiac surgery and congenital heart surgery has demonstrated how training can improve surgical practice by reducing the time required for simulations and increasing overall performance[59].

6. Purpose of the Study

The goal is to develop 3D models of heart valves that, using various resins and/or silicones, closely resemble human valves. Specifically, we focused on creating a pathological model of an aortic valve, selecting a highly prevalent condition in the population, as discussed in the epidemiology section: aortic stenosis. These 3D models can be used to accurately simulate and plan preoperative surgical procedures, particularly enabling the simulation of various surgical techniques for aortic valve replacement, as well as helping medical students better understand the pathophysiology.

In summary, this thesis aims to: (A) apply a low-cost fabrication method using CT scans, computer-aided design (CAD) software, UV resins, and platinum-cured silicones to develop aortic valve models with mechanical properties that are as

realistic as possible, facilitating realistic suturing; (B) preliminarily assess the usefulness and value of these models for cardiothoracic surgeons as training tools.

III. MATERIALS AND METHODS

For the realization of our project, we used two types of 3D printers, as previously described, along with different types of resins and silicones. In this chapter, we will first describe the process of acquiring and processing the medical images from which the 3D models were obtained and printed. After that, we will focus on the materials used to create the various models, and finally, we will discuss the steps that led to the creation of the most innovative aortic valve model produced by our department.

7. Image acquisition

The acquisitions from which the models were created were derived from contrast-enhanced cardiac CT scans. These scans were performed in the early angiographic phase, with a slice thickness ranging from 0.5 to 2 mm and a field of view covering the diaphragm and the supra-aortic arterial trunks. Several CT scans archived as Digital Imaging and Communications in Medicine (DICOM) files were used, and for each scan, a specific anatomical part was selected to standardize the model as much as possible. Therefore, the 3D model does not originate from a single CT scan but incorporates anatomical parts from different scans.

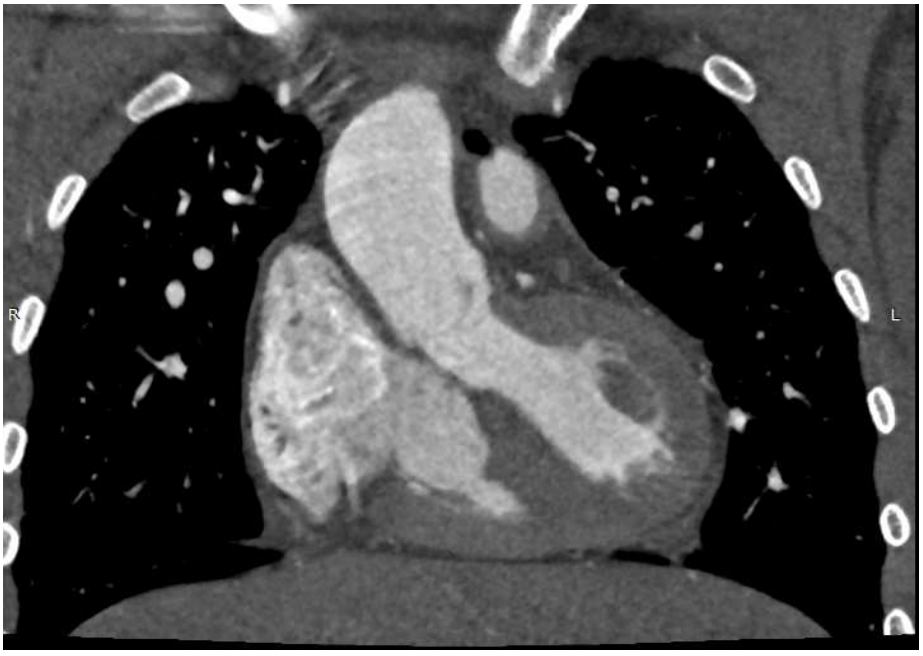

Figure 38 | *Coronal view of a CT scan during the acquisition process*.

During this phase, it is crucial to ensure that data acquisition is performed correctly; otherwise, all subsequent steps will be compromised. For instance, the presence of electron-dense materials, such as metal objects inside or outside the patient, can exceed the limit of 3,071 HU. This poses a problem because most CT scanners use standard images with a depth of 12 bits and a range from −1,024 HU to 3,071 HU. This range is typically sufficient to distinguish various tissues under normal conditions. If foreign objects are present during acquisition, it becomes necessary to use 16-bit CT images. However, this solution compresses the dynamic range of low-density anatomical structures, leading to a loss of resolution.

Another essential element in this process is the contrast agent. The segmentation process requires the maximum possible contrast between the region of interest (ROI) and everything else; therefore, insufficient administration of the contrast agent can severely compromise quality. Conversely, if the contrast agent is administered too early or too rapidly, some parts of the ROI may exhibit excessive contrast, creating artifacts, while others may have insufficient contrast, making them impossible to segment.

In summary, correct image acquisition, appropriate use of the contrast agent, and histogram analysis are crucial for effective segmentation and reconstruction of CT images.

The next step involves slicing the various acquisitions into separate images, all parallel to the same plane (usually the axial plane) and at fixed intervals. Finally, all images must be exported in uncompressed TIFF format and imported into the software for final reconstruction.

8. Image processing and printing

The software used for image processing is Mimics inPrint 3.0™ (Materialise, Leuven, Belgium), a tool for visualizing and segmenting medical images from CT and MRI scans, as well as rendering 3D objects. Materialise's Interactive Medical Image Control System ("Mimics") processes series of 2D images from various formats, including DICOM 3.0, BMP, TIFF, JPG, and more. Once processed, these images can be utilized for 3D design and printing. Mimics inPrint includes several post-processing tools that allow for small corrections, cuts, measurements, the

addition of artificial structures, and hollowing out the model to prepare it for printing. The final output of the program can be either a 3D PDF file or an STL file, which is the industry standard for 3D printing applications.

The software is modular; in the basic version, only the bone module is available. However, this module contains all essential functions, such as the segmentation tool, which allows for the reconstruction of various body parts when used correctly. Additionally, users have the option to purchase the "Heart module," which accelerates the heart reconstruction process.

The workflow is divided into five steps, made simple and accessible by the intuitive program interface: the segmentation occurs in the first two phases; the third phase, called “Add Part,” transforms the freshly segmented ROI into a “Part” (a triangulated surface); the last two phases prepare the reconstructed 3D volume for 3D printing.

Figure 39 | *Creating the ROI through threshold segmentation*.

Figure 40 | *Editing the ROI using different tools*.

Figure 41 | *Add Part panel*.

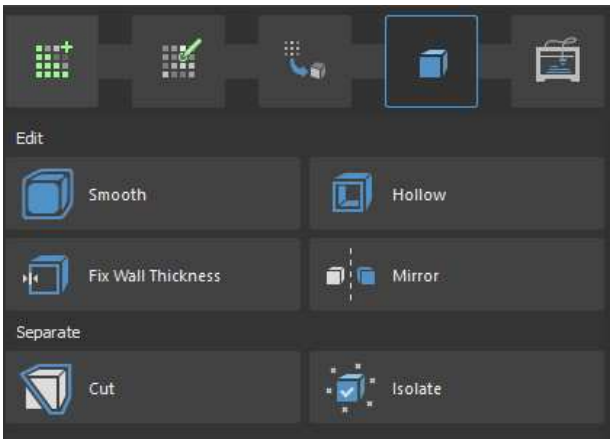

Figure 42 | *Edit part panel*.

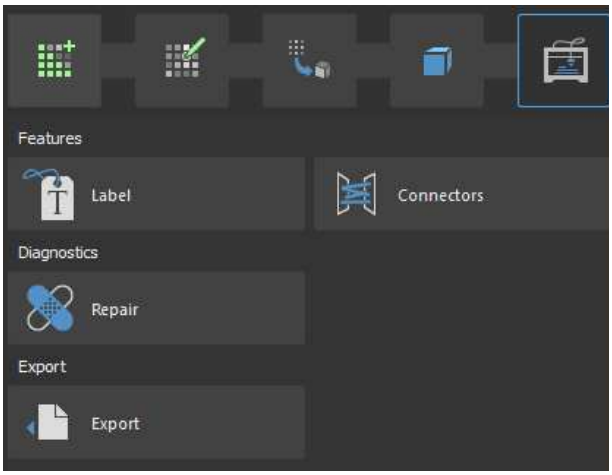

Figure 43 | *Preparing the print*.

The first step in the program is to crop the segmentation window to focus exclusively on the heart, set the threshold range, and select the region of interest (ROI). Every pixel with an HU value within the threshold range becomes part of the newly created ROI, or segment. The selected pixels are then incorporated into what is referred to as a "mask," which the software displays by overlaying a colored filter on the images in the 2D viewports.

Multiple masks with different thresholds can be generated to segment various ROIs within the same set of images. After establishing the threshold, the user can utilize the two modules located in the upper left corner of the main window: the “Edit tool group” and the “Create part” module.

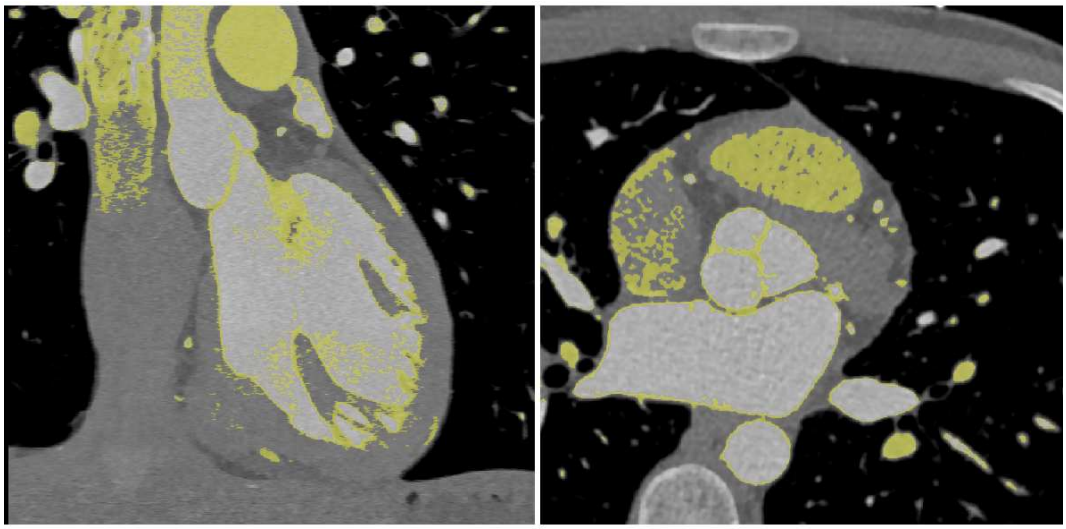

Figure 44 | *Sagittal and axial view of a CT scan during the segmentation process. Using a threshold, only the pixels within a certain range were selected, corresponding approximately to the density of endocardial tissue. The pixels corresponding to the endocardium and valves are therefore highlighted (in yellow).*

The masks can be modified with different tools present in the second panel. The main editing tools are: “Isolate”: deletes any pixel not spatially connected with the selected mask. This tool removes all unconnected parts from the main one and this is very useful because unconnected parts cannot be printed with standard 3D printing techniques; “Split”: allows for more precise separation between the ROI and the background. This tool is useful to precisely remove whatever remains of the ribcage and the vertebrae from the ROI; “Brush”: remove or add pixels to the mask in a single slice. This tool can also add and subtract pixels directly from the 3D model preview. These features make this tool the most precise way to edit the mask, but also the slowest one; “3D Interpolate”: allows the user to edit an existing ROI by only marking a few slices in Brush or Lasso Mode due to the presence of advanced interpolation algorithms that fill in the missing information. The user can manually edit only 5% of the total images obtaining results comparable to a completely manual segmentation; “Lasso”: the user draws a free-form curve and the selected area inside this shape can be added or deleted. It is used to refine the

mask directly in the 3D viewport, but it can also be used in the 2D viewport. This tool is very useful for quick modification and refinement of the model; “Fill”: based on user-defined parameters, it fills all empty spaces and cavities within the ROI.

In the third panel, called "Create Part", we can generate a solid figure of our mask that we have finished modifying. This is possible thanks to the "Solid Part" button. It is important to note that in the following panels each modification will be made on this solid figure and not on the original mask obtained from the segmentation process and modified in the second panel.

Once the solid figure has been created, it is possible to modify it in the fourth panel. There are two fundamental operators that allow us to improve and complete the 3D model: "smooth" and "hollow". As you can guess from the name, the "smooth" option allows us to smooth and soften any protrusions present in the solid model making it more uniform and regular. The "hollow" option is very important, without the use of this option our 3D model would not have cavities or internal walls. It would only represent the external anatomy but not the internal one. This option allows us to adjust the wall thickness in two ways: outward and inward. In other words, it creates a second surface translated by a fixed value along the normal to the surface, both inside the model (inward) and outside (outward). This value becomes the final thickness of the hollow model. The wall thickness value can be as low as 1.0 mm. Lower values can create printing problems and to ensure that the wall thickness is uniform throughout our model and not less than 1.0 mm, there is a tool called "Fix Wall Thickness" that automatically analyzes and highlights areas with a thickness different from the one set.

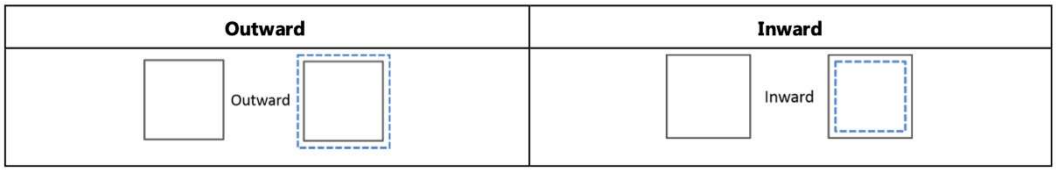

Figure 45 | *Schematic image of the “Hollow” mechanism.*

The last tools in this section are: "Cut", which allows us to open windows inside the model by removing parts of the external surface and therefore allows us to observe the model inside; "Mirror", which allows us to create a mirror image of our model;

"Isolate" has the same function as the tool with the same name present in the second panel only that it operates on the solid model and not on the mask.

The fifth panel, called “Prepare Print,” allows you to export the model as an STL file. This STL file is then loaded into Meshmixer™ (Autodesk Inc., San Rafael, CA, USA), a CAD post-processing software that offers various tools for refining the model. Additionally, if necessary, the wall thickness can be reduced to less than 1 mm. This step was crucial in the creation of our aortic valve model, as it posed a significant challenge to achieve a thickness that was both thin and durable. Once the adjustments are complete, the model is prepared for the printing process, which follows the mechanisms outlined in the previous section where we analyzed the characteristics of the printers available in our department.

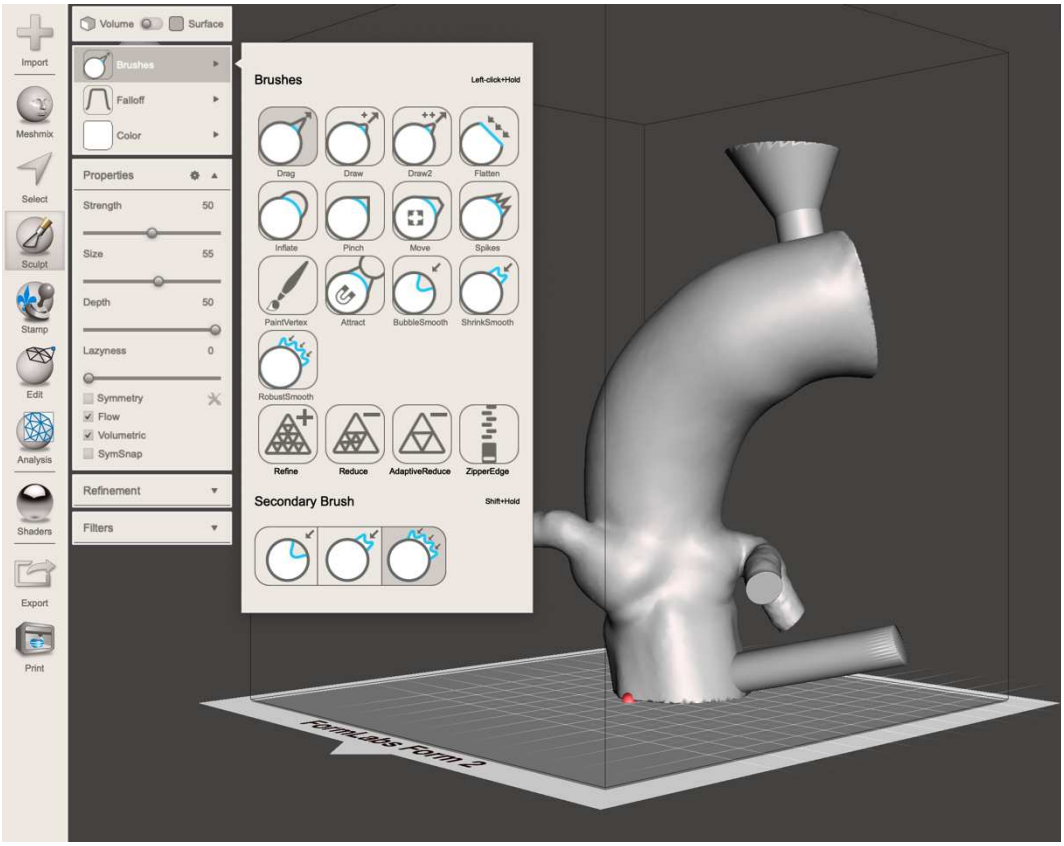

Figure 46 | *A selection of editing tools available in MeshMixer™.*

9. Resins and silicones

For the creation of the aortic valve models, we used both the FormLabs™ Form3L™ printer and the Sisma Everes Uno™ printer. These printers utilize resins

with different chemical and physical characteristics. Over time, we have tested several of these resins in an effort to create a model with consistency and elasticity as similar as possible to real tissues. Of course, our experimentation was not limited to aortic valve models; many models of congenital heart disease have been reconstructed over the years with excellent results. Additionally, we managed to fabricate a high-quality model of the mitral valve. However, the most satisfactory results have currently been obtained with the aortic valve, as this is the first time in our department that we have used a new method and new materials for creating 3D models. Specifically, we employed a platinum silicone rubber gel with a Shore hardness of 00-20 to develop the first 3D model at the University of Padua with anatomical and mechanical characteristics that closely match real anatomy.

The materials used to create the models, in chronological order of use, were: Formlabs Clear Resin™, Formlabs Elastic Resin™, Loctite IND475™, Formlabs Grey Resin™, Smooth-On Mold Star 15 Slow™, and Smooth-On Ecoflex Gel™.

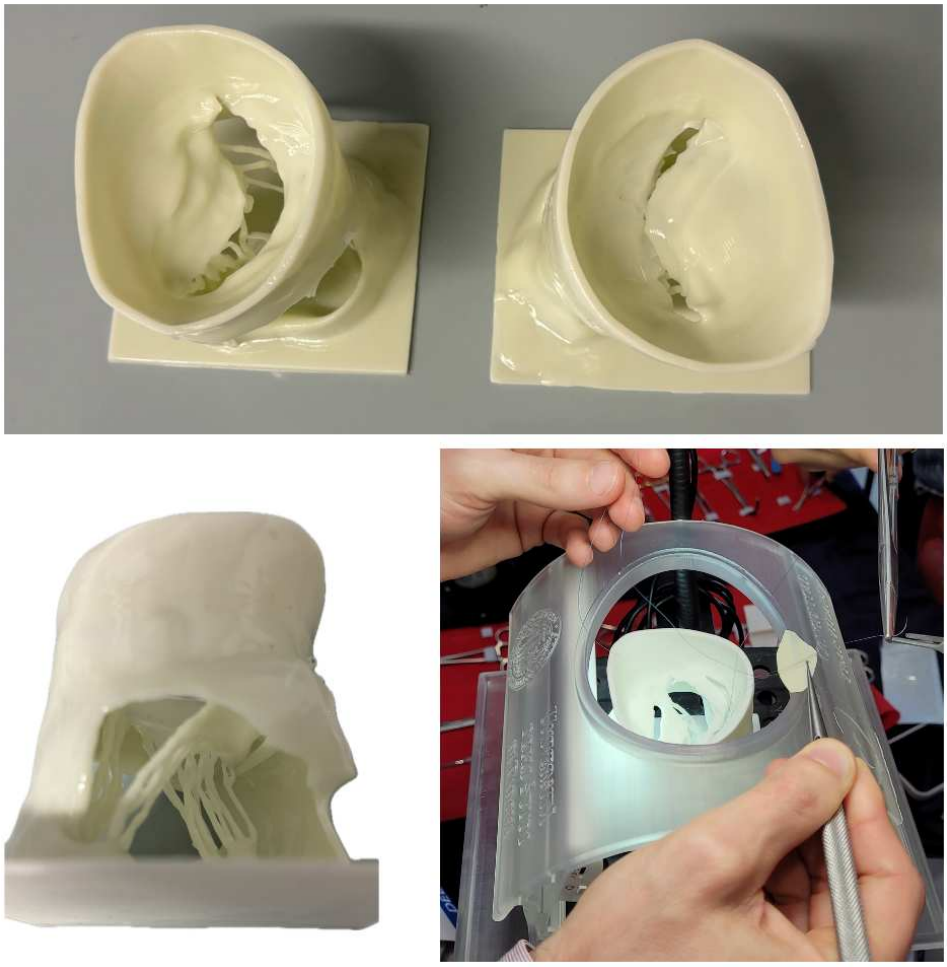

Figure 47 | *A selection of editing tools available in MeshMixer™.*

Before describing the individual models created with the different materials, it is important to introduce the concept of material hardness. Hardness can be defined as a material's resistance to permanent indentation. Among the various hardness scales, one was developed by Albert F. Shore, who in 1920 created a device to measure the hardness of materials such as polymers, elastomers, and rubbers. Hardness is determined using a Shore durometer, which measures the depth of indentation made by a penetrator inside a material under a certain force. This depth depends on the material's hardness, its viscoelastic properties, the shape of the penetrator, and the duration of the test.

There are several types of Shore hardness scales, each suited for materials with different properties. There are 12 types of Shore scales. The most used are the Shore A scale (for soft plastics), the Shore D scale (for harder plastics), and the Shore 00 scale (for very soft rubbers and gels). Each scale has a measuring range from 0 to 100, with higher values indicating greater hardness in the material being measured.

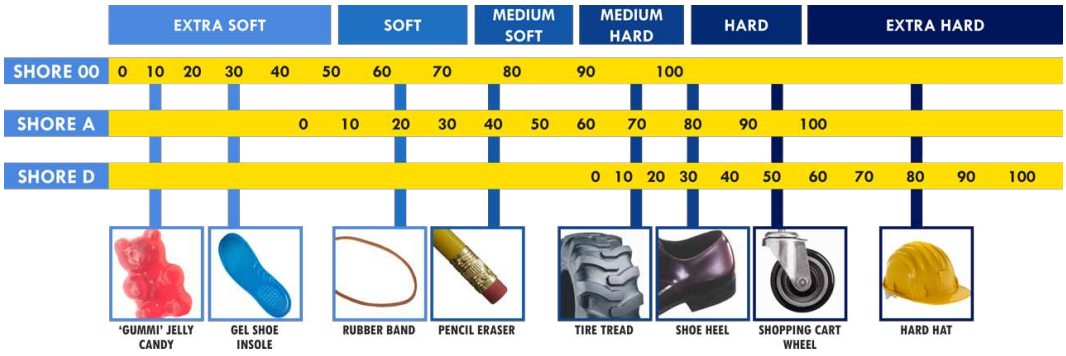

Figure 48 | *Shore scale, scale that measures the hardness of plastic and rubber materials.*

IV. RESULTS

10. 3D Resin Models

Formlabs Clear Resin™ is a rigid, neutral-colored 3D printing resin that offers an optimal balance between high print speed, high dimensional accuracy, and a presentation-ready appearance. When properly cured, it is very strong, with a maximum tensile strength of 60 MPa and an elongation at break of 8%. However, it is not suitable for surgical training and simulation, as it does not have a texture similar to real tissue. The details of the models are clearly visible, making it a good choice for creating pre-operative training and consultation models. The first aortic valve model was printed using this resin as an experiment to evaluate the accuracy of segmentation and processing of the 3D model.

Figure 49 | *3D model of aortic valve in Formlabs Clear Resin™.*

Formlabs Grey Resin™ is a versatile general-purpose resin, offering an optimal balance of fast print speed, strong mechanical properties, and an easy, reliable workflow. It has an elongation at break of 13% and an ultimate tensile strength of 62 MPa. It's a very resistant resin, capable of an impact resistance greater than 30%. For this reason, we used this resin to create the models to be used as "mold cores".

Formlabs Elastic Resin™ is an elastomer designed to print soft, flexible parts. It was long Formlabs' softest engineering resin but has now been surpassed by the new Flexible 80A Resin™. The elastic resin has a Shore hardness of 50A and an elongation at break of 160.0%. This resin is typically used for parts that bend, stretch, compress, and withstand repeated cycles without tearing. This resin was used to print the first aortic valve models for surgical simulation and pre-operative planning.

Figure 50 | *3D model of aortic valve in Formlabs Elastic Resin™.*

In a study to evaluate the effect of design/geometry (model) and material (resin) on model accuracy, it was found that the type of resin significantly influences model accuracy. The accuracy of a model is defined by the error between the physically measured dimension and the predicted dimension. The results of the study are that

Formlabs Elastic Resin™ shows lower accuracy than Formlabs Clear Resin™, which, although clinically insignificant at the 1 mm threshold, still requires special attention when 3D printing in medicine[63].

This discrepancy has also been highlighted in our experience with 3D cardiac models. This has led us to explore new soft materials that can still maintain high accuracy.

Loctite 3D IND475™ is a single-component, industrial-strength UV resin that cures to a soft, elastomeric material. IND475 is suitable for applications that require resilience, elasticity, and tear resistance, such as lattice structures and functional prototyping. It is the main resin type we use on our Sisma Everes Uno™ printer. The resin has a Shore hardness of 62A, a strain at break of 160%, and an elastic return of 55%. We have achieved good results using this resin. The models were very similar to those printed with Formlabs Elastic Resin™. However, for the same reasons listed above when discussing Elastic Resin™, we thought about using a new method for creating the 3D model.

Figure 51 | *3D model of aortic valve in Loctite 3D IND475™ with a biological valve.*

We presented the Loctite 3D IND475™ aortic valve 3D model during the Hands-On in Pediatric and Congenital Cardiac Surgery (3D Simulation) at the World

Summit for Pediatric and Congenital Heart Surgery 2024. Cardiac surgeons from around the world tested aortic valve replacement on this model. We received excellent feedback, which encouraged us to continue our research on new materials to further enhance the accuracy and consistency of the models.

Figure 52 | *3D model of aortic valve in Loctite 3D IND475™ with a biological valve.*

After conducting various printing experiments, our research shifted to a field we had never previously explored: elastomers. Silicone elastomers can be formulated to exhibit low elastic modulus, high extensibility and toughness, excellent thermal and oxidative stability, and chemical inertness[64, 65].

For the creation of our first silicone 3D model, we chose to use Smooth-On Ecoflex™ GEL (Smooth-On, Macungie, PA, USA). This is an extremely soft platinum silicone rubber gel with a Shore hardness of 00-20 and an elongation at break greater than 1000%. It is translucent, allowing for infinite color effects by adding silicone pigments. Ecoflex™ GEL is mixed in a 1A:1B ratio by weight or volume. The molds were created using Smooth-On Mold Star™, easy-to-use platinum silicones that are mixed in a 1A:1B ratio by volume with a Shore hardness of 15A.

11. 3D silicone model: first time at University of Padua

There are several steps involved in creating the definitive Smooth-On Ecoflex™ silicone model of the aortic valve. We will briefly summarize these steps in this section and then analyze each one individually:

- Processing of medical images and printing of the 3D model
- Creation of the mold with Smooth-on Mold Star™
- Degassing the Smooth-On Ecoflex™ silicone
- Introducing the Smooth-On Ecoflex™ silicone into the mold
- Extracting the Smooth-On Ecoflex™ silicone model from the mold

In total, we created three 3D prototype models. In this chapter, we will analyze the various steps involved and the motivations that drove us to improve the first two prototypes to arrive at the third and final version.

The acquisition and processing of medical images were discussed extensively in the previous section. It is important to reiterate that our aortic valve model does not originate from a specific CT scan of a particular patient. Instead, we assembled the different anatomical parts that make up the aortic valve by acquiring slices from various CT scans. This approach aimed to create a model that is as standardized as possible. As mentioned earlier, the 3D models used as molds for creating the final

mold were made from Formlabs Grey Resin™ and Formlabs Clear Resin™. Because these resins are non-soft, they maintain their shape, allowing for the creation of a mold into which the silicone was subsequently poured.

11.1 Prototype 1

The 3D models used as casts for the mold were made from Formlabs Gray Resin™ (Figure 53). We first created a 3D model of the ascending aorta and coronary arteries, which was placed in a container and completely covered with Smooth-On Mold Star™ (Figure 54 A). The plan was to create the aortic valve separately using the same manufacturing method and then adhere it inside the annulus.

As shown in Figures 54 A and 54 C, the 3D model included thin resin cylinders that extended to the bottom of the container. These cylinders serve as vents, allowing air to escape when the silicone is poured.

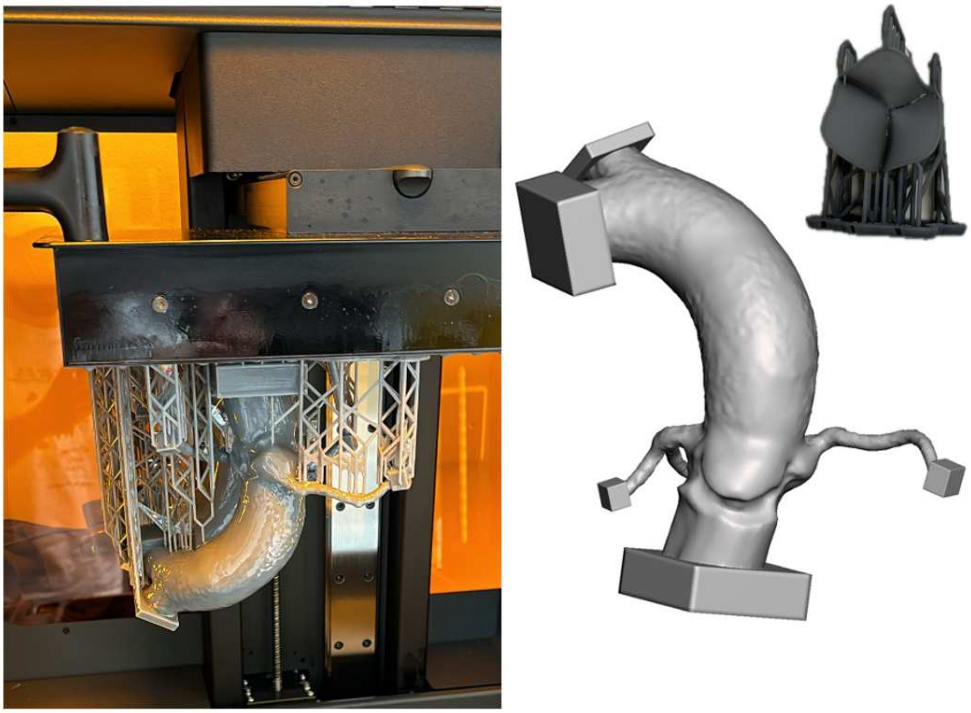

Figure 53 | *On the right, a picture of the freshly printed Gray Resin™ 3D model; on the left, a 3D CAD software screenshot of the same 3D model before printing.*

Once the Mold Star™ had cured, we extracted the Mold Star™ block containing the first 3D model in Gray Resin™ from the container (Figure 54 B). We then turned the Mold Star™ block upside down and opened it by cutting it into wedges;

however, we did not cut the wedges completely, stopping about halfway through the block (Figure 54 C). This technique allowed us to extract the first 3D model in Gray Resin™ that was inside (Figure 54 D). An interesting property of Mold Star™ is that it always returns to its original shape, so making cuts in the appropriate positions does not deform the structure of the mold.

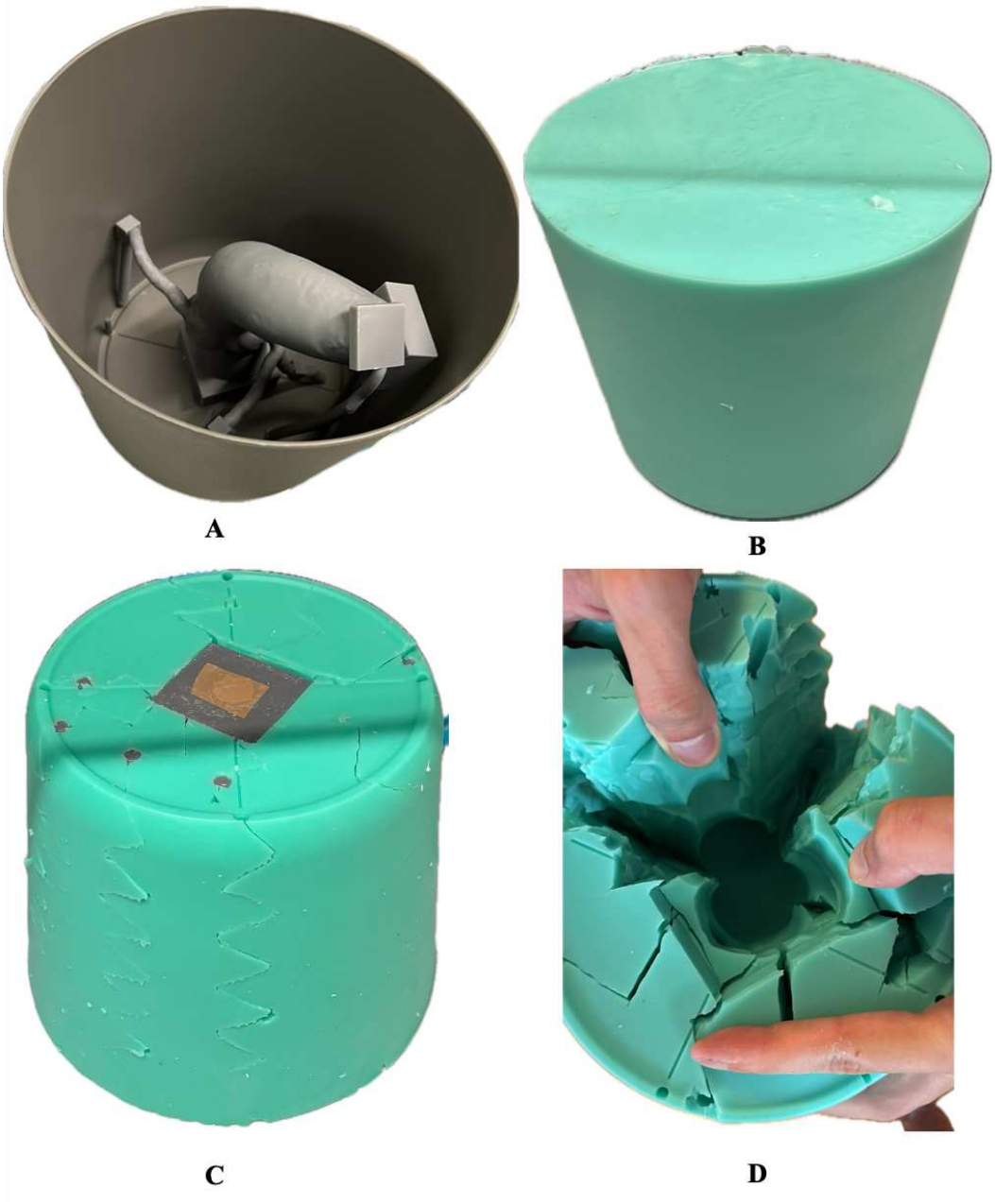

Figure 54 | *(A) first Gray Resin™ 3D model inside the container before pouring the Mold Star™ silicone to create the mold; (B) Mold Star™ silicone mold reticulated and removed from the container with the first Gray Resin™ 3D model inside; (C) Mold Star™ silicone mold turned upside down with the first Gray Resin™ 3D model still inside; (D) Mold Star™ silicone mold opened and first Gray Resin™ 3D model removed.*

Once the first Gray Resin™ 3D model was extracted, what remained was the cast of the first model inside the Mold Star™ block. Our plan was to create a second Gray Resin™ 3D model that was 2 mm smaller than the first. We then inserted the second Gray Resin™ model into the Mold Star™ mold, as its shape matched that of the cast left by the first model (Figure 55 A). Since the second model was 2 mm smaller, this created a 2 mm gap between the Mold Star™ cast and the wall of the second Gray Resin™ model (highlighted by the red arrow in Figure 55 A). We then sprayed Smooth-On Universal™ Mold Release, a release agent, inside the mold. This agent facilitates the removal of mold rubbers from prepared models and helps release a variety of casting materials. After applying the release agent, we poured Smooth-On Ecoflex™ silicone into the gap (Figure 55 B), ensuring that the wall thickness of the ascending aorta and coronary arteries was 2 mm.

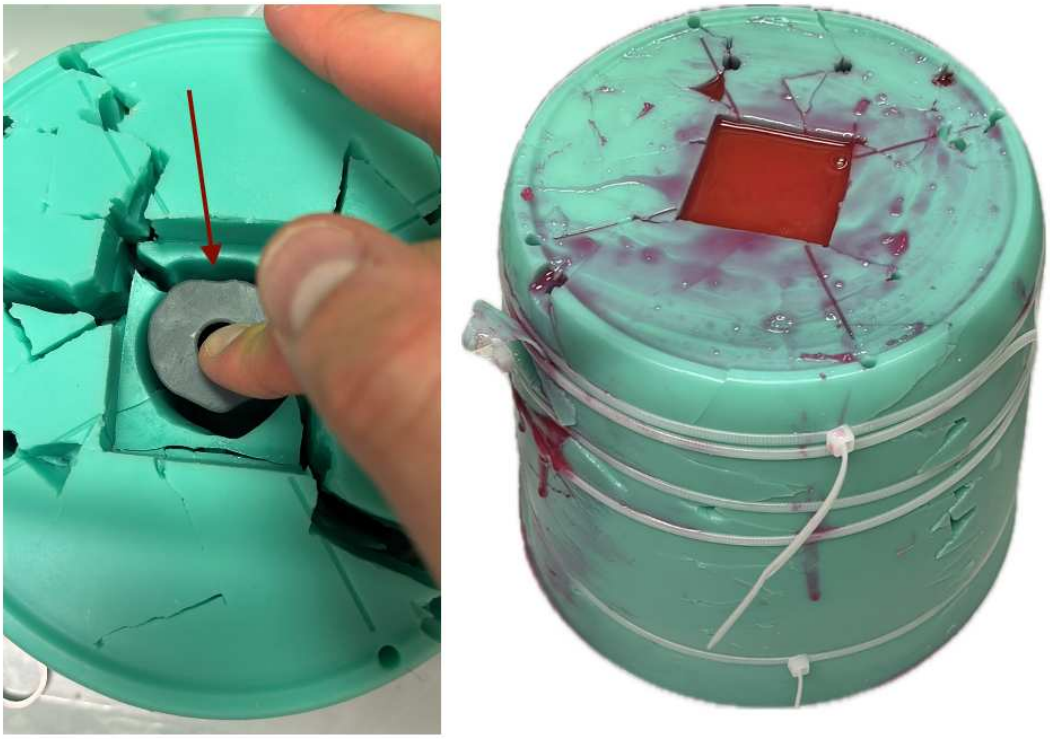

A **B**

Figure 55 | *(A) second 3D model in Gray Resin™ (2 mm smaller than the first model) positioned inside the cast of the first 3D model inside the Mold Star™ mold with red arrow highlighting the cavity in which to pour the EcoflexTM silicone; (B) Ecoflex™ silicone poured inside the cavity waiting for it to reticulated.*

After several attempts with this method, we identified some critical issues that needed to be addressed. The first problem was the complex shape of the Gray

Resin™ 3D model used to create the cast. The coronary arteries were very long, thin, and curved, which often led to breakage when we extracted the Smooth-On Ecoflex™ silicone from the mold. To address this, we aimed to optimize the shape of the Gray Resin™ model.

Additionally, we noticed that the Ecoflex™ silicone trapped a significant amount of air, resulting in many bubbles that weakened the structure and made it fragile. To tackle this, we began degassing the silicone.

The final issue was with the method of pouring the Smooth-On Ecoflex™ silicone into the mold. Pouring it into the 2 mm gap (highlighted by the red arrow in Figure 55 A) proved ineffective, as the silicone was not distributed evenly, leading to waste. To resolve these problems, we completely redesigned our approach, resulting in the creation of prototype 2.

Figure 56 | *Final result with the presence of air bubbles inside the silicone highlighted.*

11.2 Prototype 2

For prototype two, we completely revised the initial project. Instead of creating two Gray Resin™ 3D models offset by 2 mm, we decided to create a single hollow 3D model that already contained the aortic valve (Figures 57 and 58 A, B). This approach allowed us to eliminate the step of inserting a second Gray Resin™ model into the Mold Star™ mold.

In this new design, the Gray Resin™ model is hollow (unlike the 3D models used in prototype one) and features predefined thicknesses for both the wall of the ascending aorta and the cusps of the aortic valve. Additionally, we implemented a system to inject the Smooth-On Ecoflex™ silicone directly into the mold using a syringe. The cylinder at the bottom, visible in Figures 57 and 58, serves this purpose and can be easily cut with scissors from the Ecoflex™ silicone model at the end of the production process. The same applies to the cone-shaped air intake located at the top of the model.

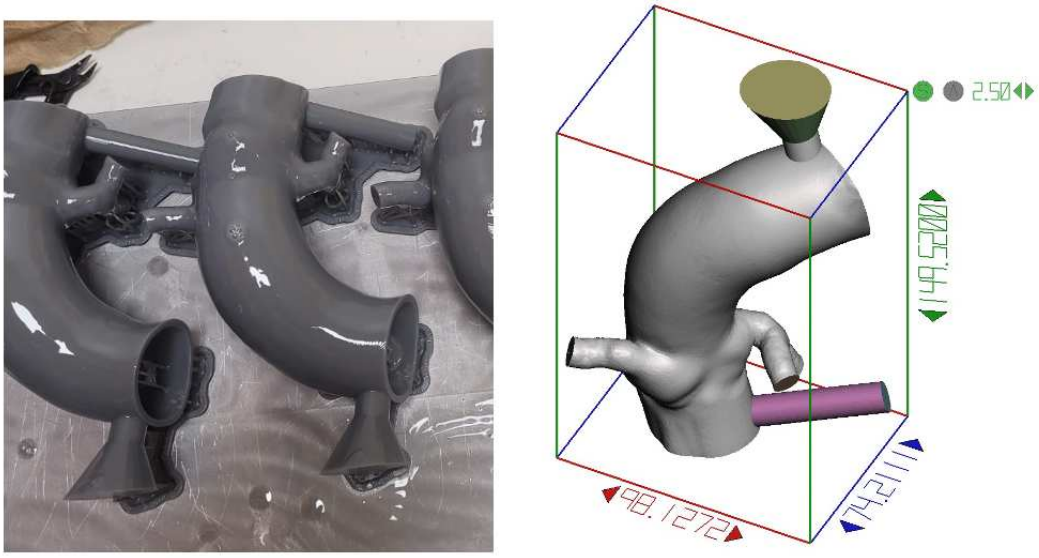

Figure 57 | *On the right, a picture of the Gray Resin™ 3D model not yet subjected to post-print treatment; on the left, a 3D CAD software screenshot of the same 3D model.*

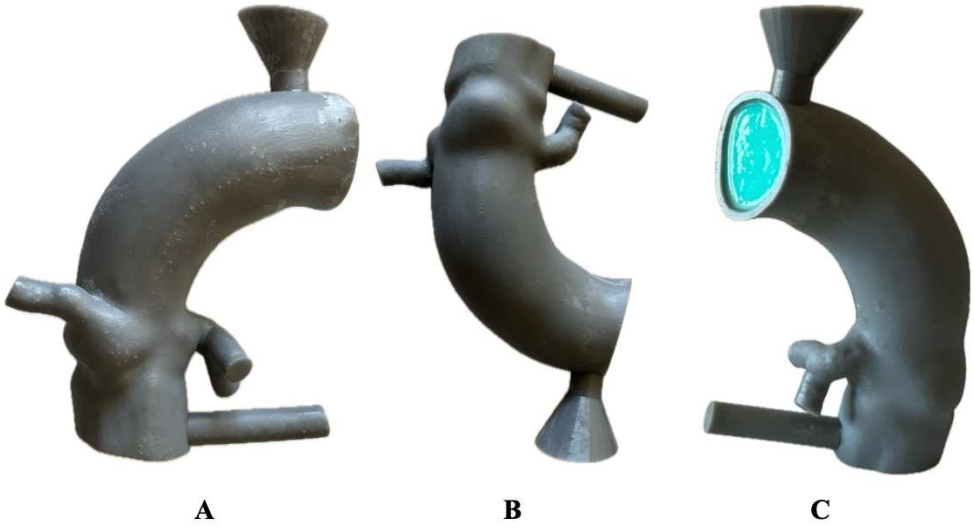

Figure 58 | *(A) Anterior view of the Gray Resin™ 3D model; (B) Posterior view of the Gray Resin™ 3D model turned upside down; (C) Posterior view of the Gray Resin™ 3D model with ascending aorta filled with Mold StarTM silicone.*

Unlike prototype 1, which was placed directly in a container filled with Mold Star™ silicone to create the mold, in this case, the ascending aorta must first be filled individually with Mold Star™. This is feasible because the aortic valve inside has sealed cusps, which will need to be opened with a scalpel on the final Ecoflex™ silicone model (Figure 58 C).

The ascending aorta is filled first because the model is placed inside the container upside down, using the air intake at the top as a base for attachment (a light layer of vinyl glue is sufficient to secure the model and prevent movement while pouring the Mold Star™ silicone). Since the model is upside down, there's a risk that the area between the coronary arteries and the upper portion of the aortic valve remains unfilled with Mold Star™ silicone when it's poured in. To address this, we pre-fill this area with Mold Star™ silicone, allow it to dry for about three hours, and then glue the Gray Resin™ model to the bottom of the container to proceed with creating the mold (Figures 58 C and 59 A). An interesting property of these silicones is that even if part of them has already polymerized, adding unpolymerized silicone still bonds to the polymerized portion. This ensures that the Mold Star™ silicone fills all cavities, effectively creating the cast of the Gray Resin™ model (Figures 59).

A **B** **C**

Figure 59 | *(A) 3D model in Grey Resin™ glued to the bottom of the container; (B) start of the process of filling the container with Mold Star™ silicone; (C) start of the process of filling the container with Mold Star™ silicone.*

After that, the Mold Star™ mold is opened, as described for prototype 1, and the Gray Resin™ model is extracted. We turn the mold upside down so the model regains its correct anatomical position (recalling that the 3D model was initially placed with the ascending aorta facing down during the mold creation).

Next, the Ecoflex™ silicone is degassed for about five minutes in a vacuum chamber to remove any trapped air. Before introducing the silicone into the mold, we spray Smooth-On Universal™ Mold Release, a release agent, inside. Then, we use a syringe to inject the Ecoflex™ silicone directly through the special cylinder at the bottom of the Mold Star™ mold (this cylinder will appear as a hole on the mold's external surface). Once the Ecoflex™ silicone reaches the correct level in the mold, it will overflow from the cone at the top.

Figure 60 | *On the left, reticulated Mold Star™ silicone mold removed from the container; on the right, Mold Star™ silicone mold turned upside down.*

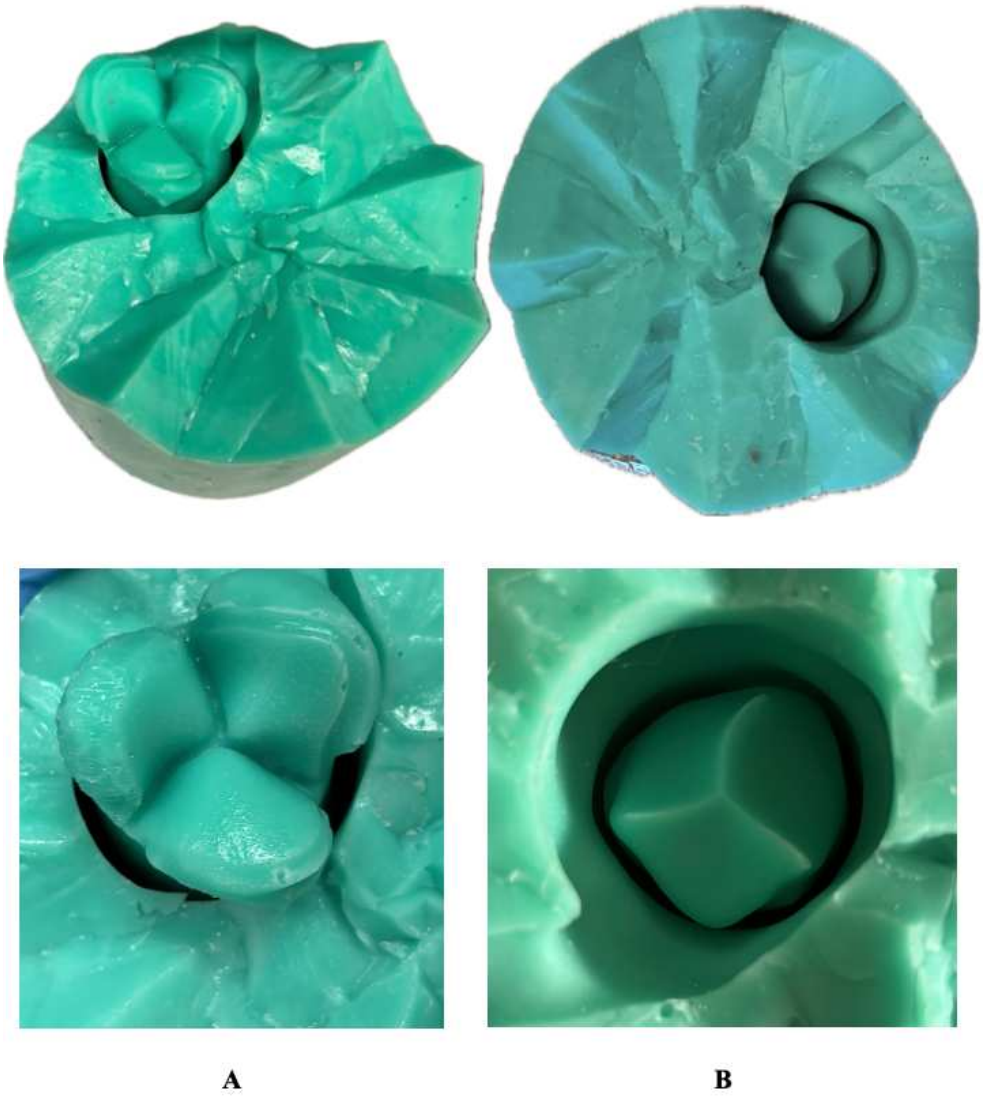

Figure 61 | *Mold Mold Star™ silicone open close to the aortic valve. (A) detail of the upper part of the mold; (B) detail of the lower part of the mold.*

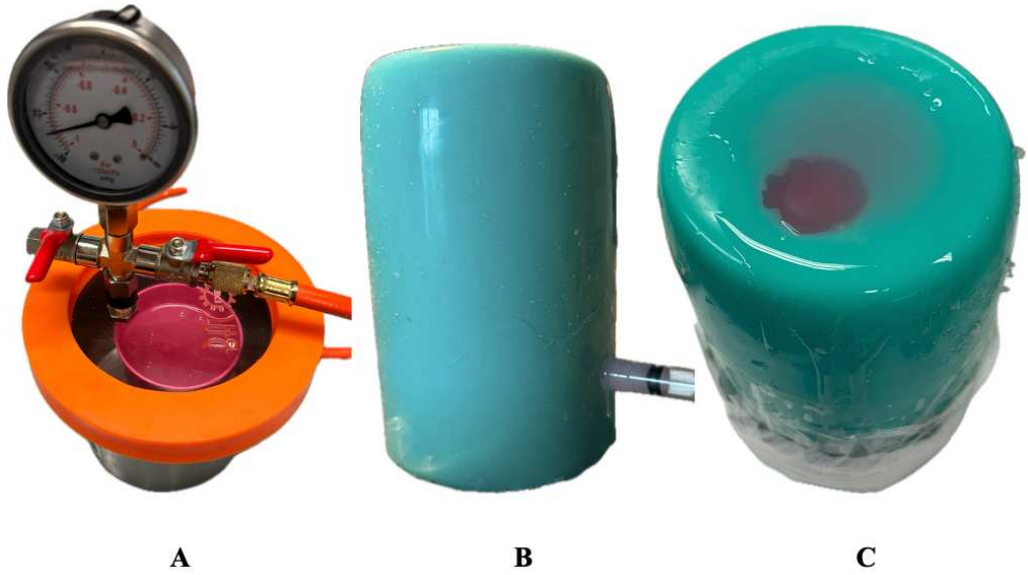

Figure 62 | *(A) degassing phase of Ecoflex™ silicone with vacuum machine; (B) injection with syringe of Ecoflex™ silicone inside the mold; (C) mold filled with Ecoflex™ silicone.*

After allowing the Ecoflex™ silicone to cure for at least four to five hours, we can open the mold and extract the Ecoflex™ silicone aortic valve model.

Figure 63 | *Details of Ecoflex™ silicone 3D models extracted from the mold at the end of the curing process.*

While we were pleased with the second prototype, our regular surgical training sessions in the U.O.C. revealed areas for further improvement. Firstly, the patency of the coronary arteries needed enhancement; in the second prototype, the origins of the coronary arteries were not patent, limiting the range of simulated interventions with the silicone aortic valve model (highlighted by the red arrow in Figure 64). Secondly, we aimed to refine the method for securing the model to our chest wall simulators. As a result, we developed the third prototype.

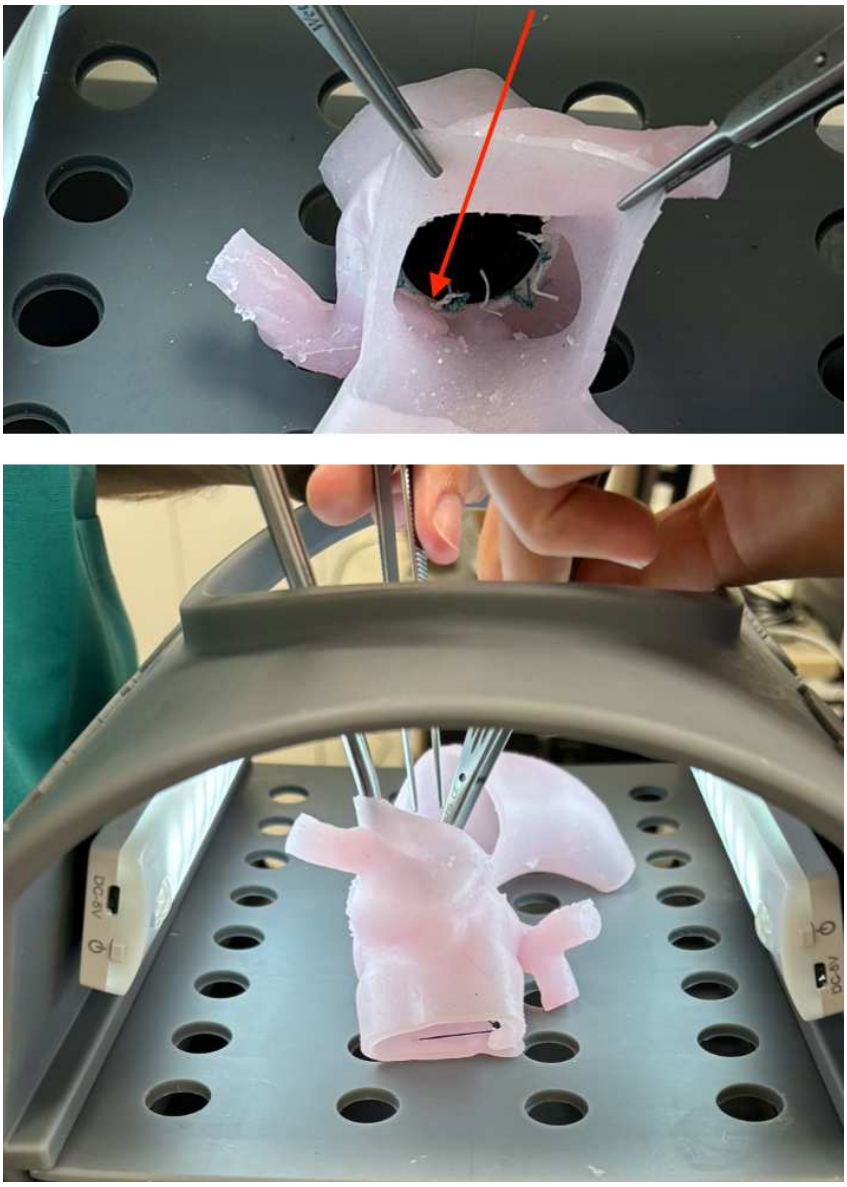

Figure 64 | *Elements to improve in prototype 2. Above, the occluded coronary ostium that bothers the surgeon during training; below, the lack of an anchoring system on the 3D-printed surgical simulator (TrainHeart).*

11.3 Prototype 3

The third prototype retains the same manufacturing process as prototype 2 but features a new 3D model from which the mold was created. This model was printed in Formlabs Clear Resin™, which has characteristics similar to Grey Resin™ but includes open beginnings for the coronary arteries and silicone pins that fit into the holes of our chest wall simulators. These modifications enhance the model's stability, allowing surgeons to perform precise procedures. Additionally, we reintroduced a portion of the atrium below the valve, similar to the 3D models of the aortic valve previously printed in Elastic Resin™ and Loctite IND475™. The models will also be presented during the Hands-On at the 38th EACTS (European Association for Cardio-Thoracic Surgery) Annual Congress in Lisbon, Portugal, from 09/10/2024 to 12/10/2024.

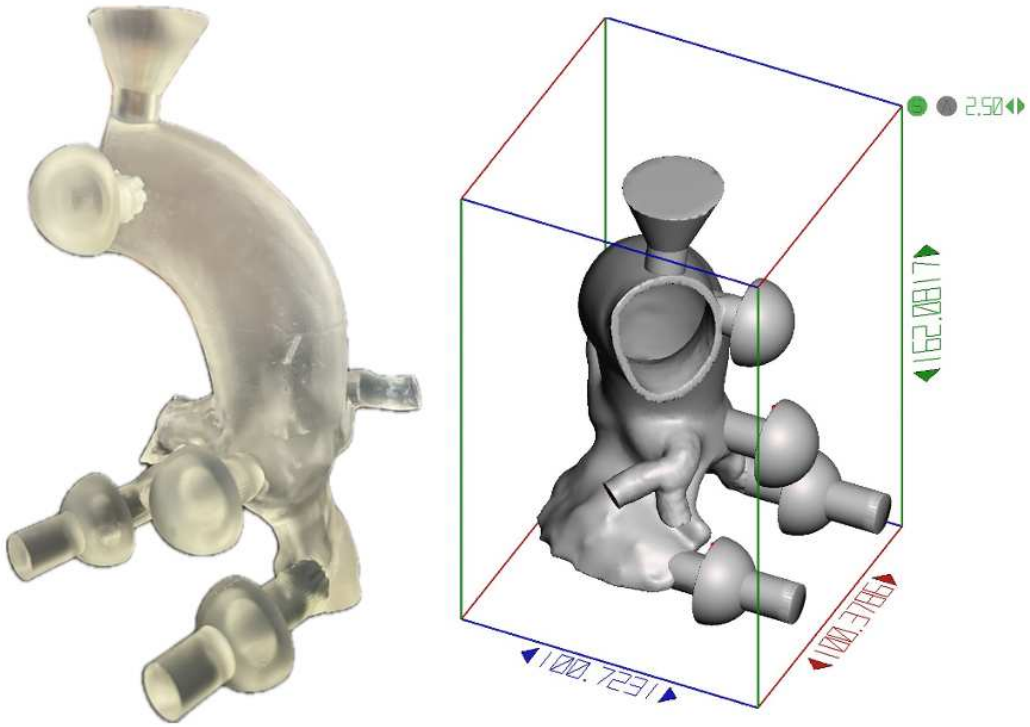

Figure 65 | *Details of the Clear Resin™ 3D model and a 3D CAD software screenshot of the same 3D model.*

Figure 66 | *Details of the Clear Resin™ 3D with focus on the aortic valve.*

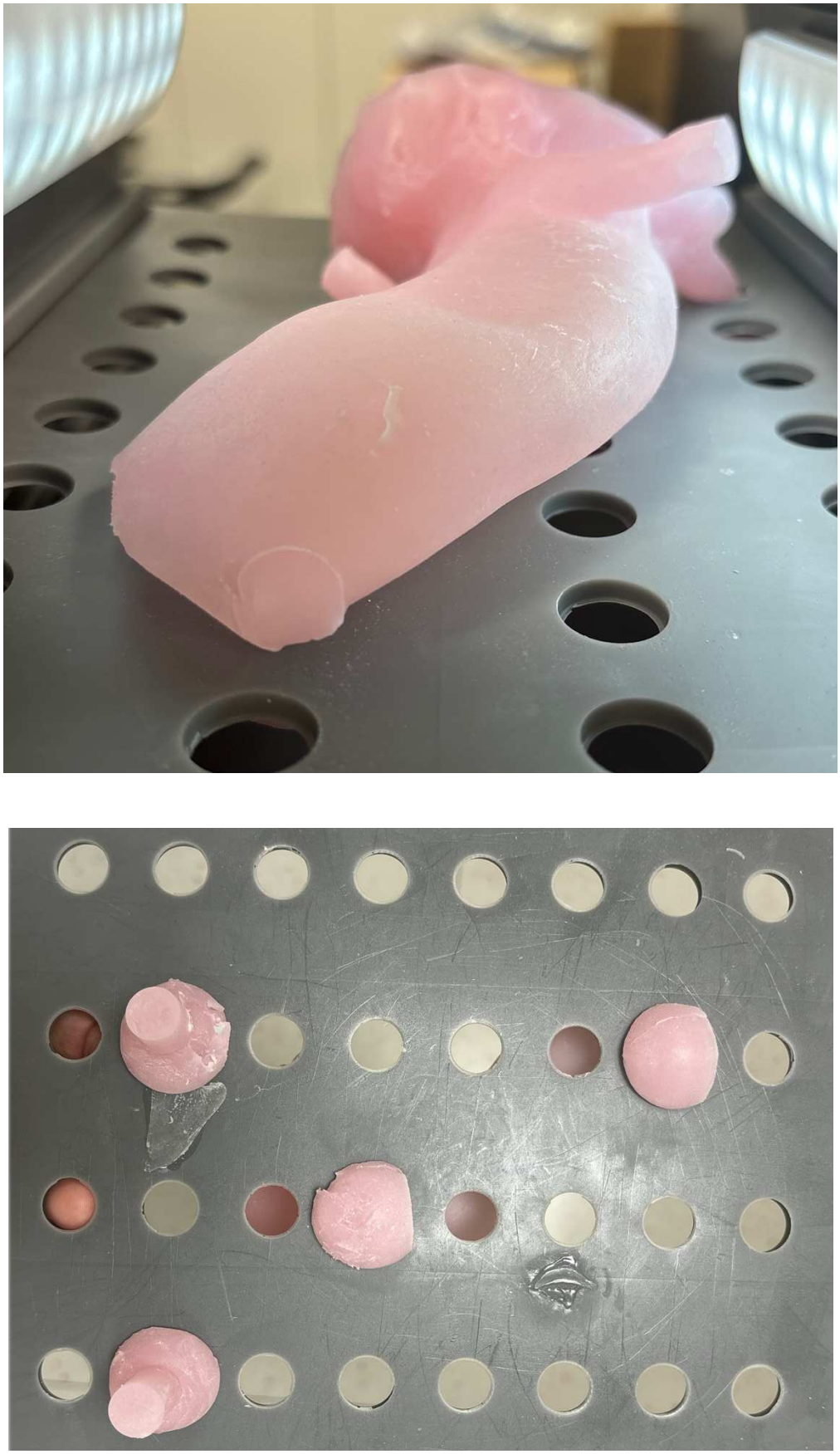

Figure 67 | *Details of Prototype and the anchoring system to the Train Heart.*

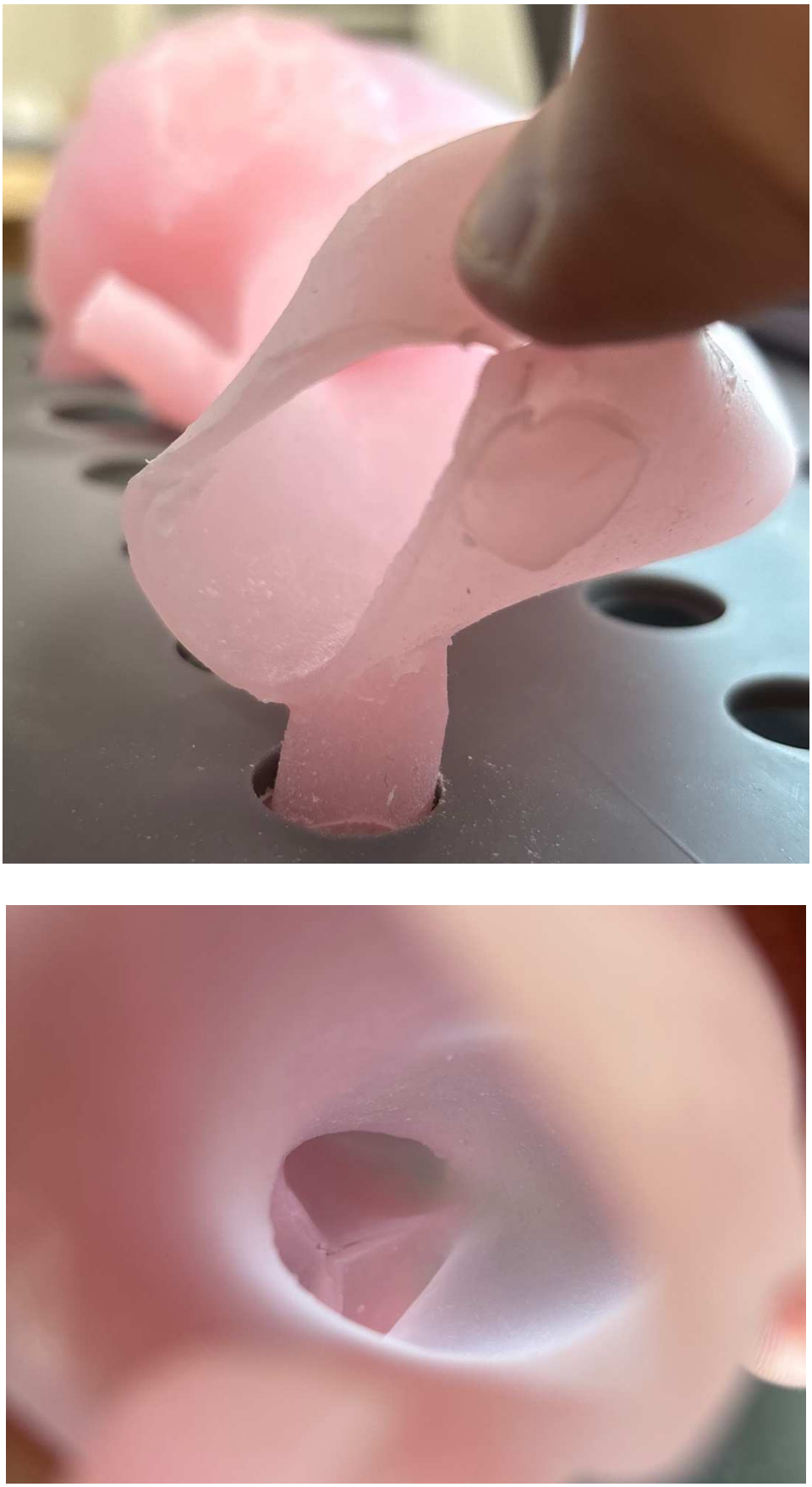

Figure 68 | *Internal details of the ascending aorta.*

Figure 69 | *Details of the valve with stenotic cusps.*

Figure 70 | *Focus on the patent coronary ostia, characteristic of Prototype 3.*

12. Surgical procedures on the 3D silicone model

We tested our second prototype during a surgical exercise, where a valve excision was performed on the model, followed by the implantation of a mechanical valve using the continuous suture technique. The detailed steps of the surgical procedure are explained in paragraph 3.

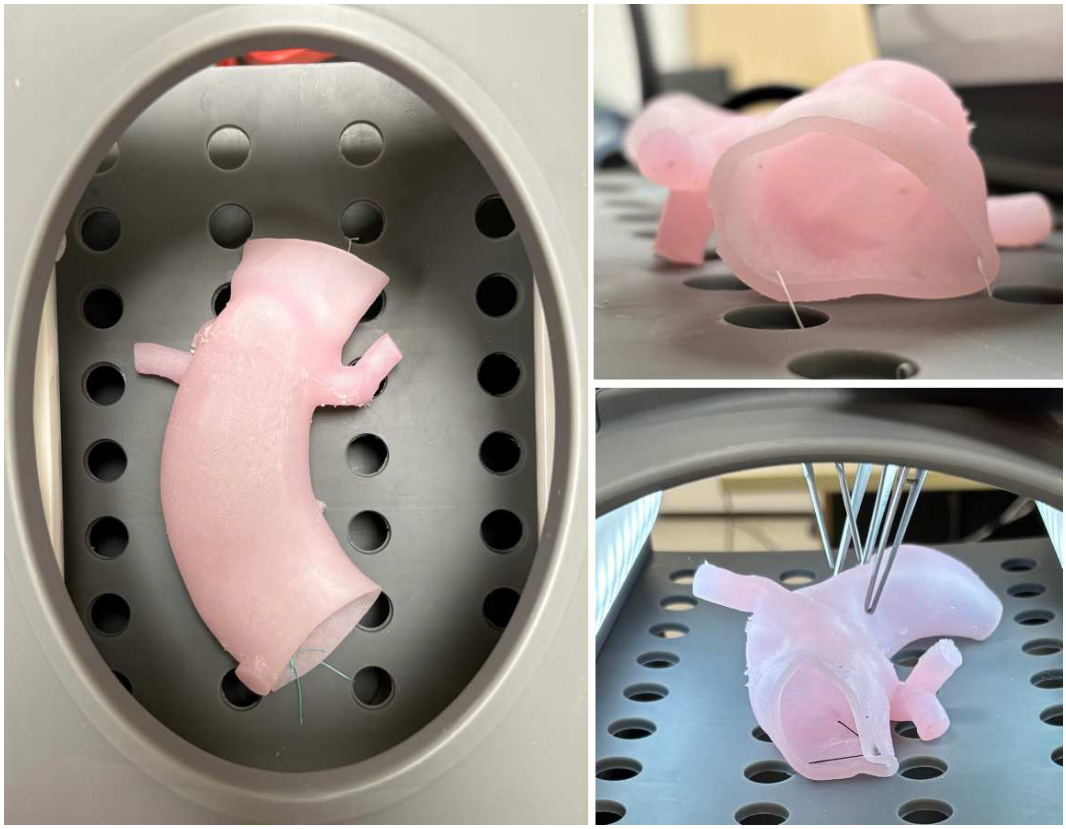

Figure 71 | *3D silicone model inside the Train Heart.*

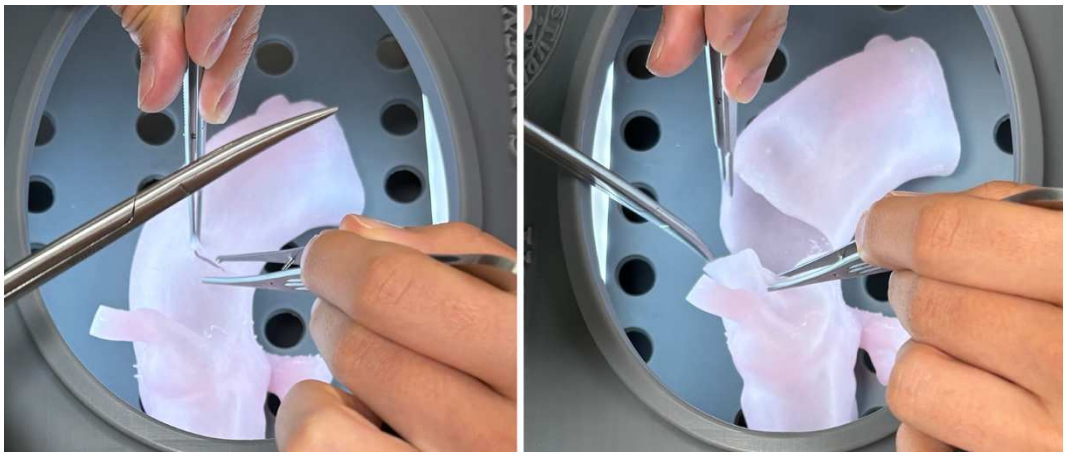

Figure 72 | *Transverse incision is made in the ascending aorta and extended into the noncoronary sinus of Valsalva.*

Figure 73 | *Cusp excision.*

Figure 74 | *Prosthetic valve is sutured to the aortic valve annulus.*

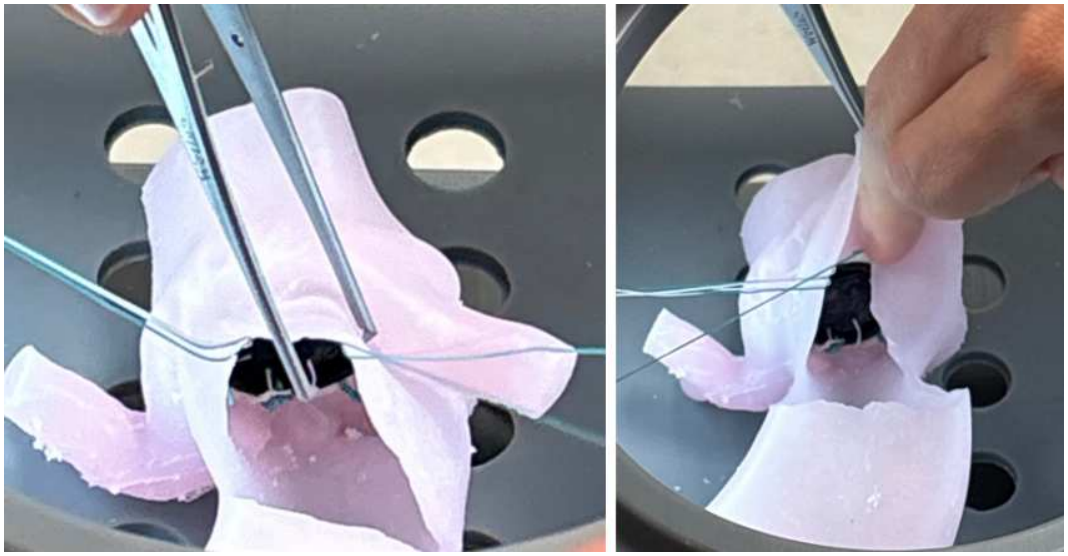

Figure 75 | *Prosthesis is placed in the aortic valve ring and the sutures are tied.*

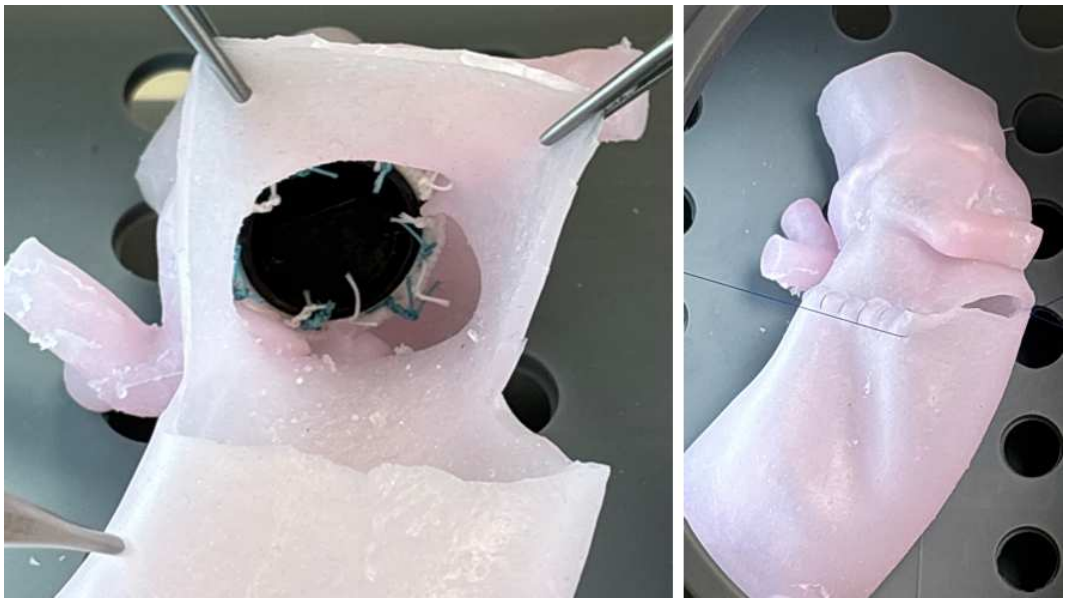

Figure 76 | *Detail of completed valve replacement and closure of the ascending aorta.*

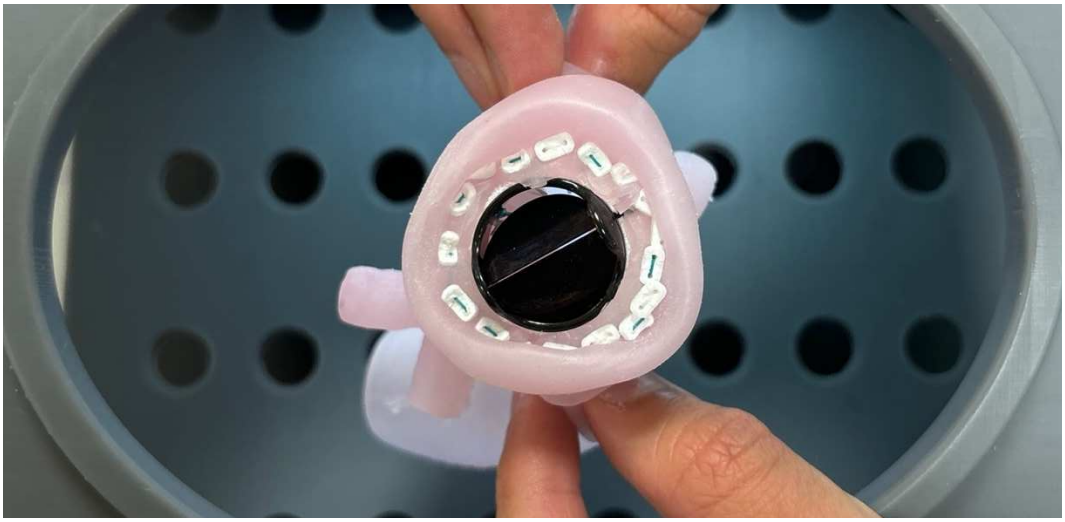

Figure 77 | *Detail of completed valve replacement seen from left ventricle.*

Other procedures were performed by different operators, and for this reason, we decided to administer a survey to the trainees to evaluate their level of satisfaction with the silicone model and identify any defects that need improvement.

We administered the survey to 10 surgeons and obtained interesting results that lay the foundation for a future Prototype 4. Each vote has been entered into the graph. The y-axis shows the votes assigned to the elements represented on the x-axis.

The questions we asked were:

- How closely do you think the 3D silicone model replicates human anatomy? [Ratings range from 1 (Very different) to 5 (Very similar)].

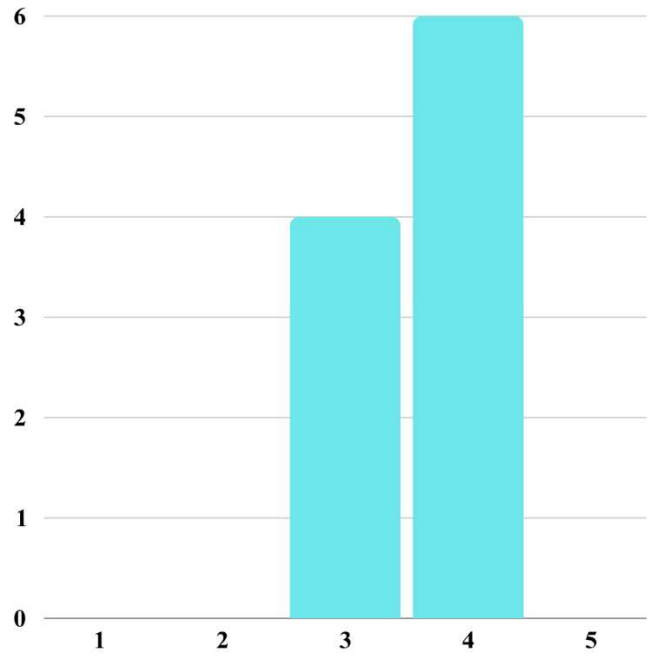

Figure 78 | *Bar graph of anatomical verisimilitude between 3D model and reality.*

- Which part or parts of the 3D silicone model are most accurate in replicating real human anatomy?

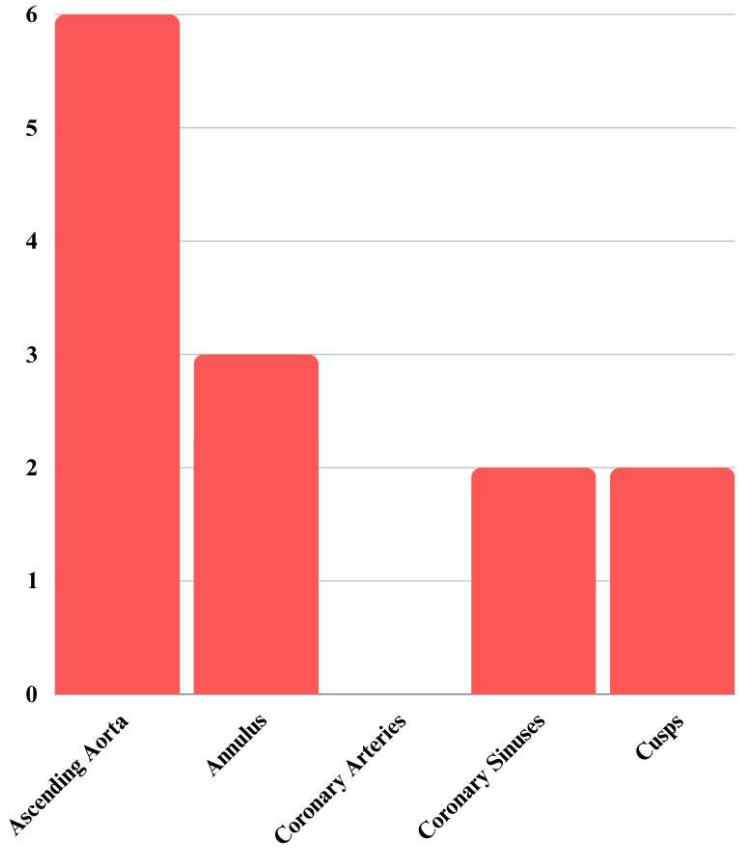

Figure 79 | *Bar graph of the anatomical components of the silicone model that are most similar to the real anatomical components.*

- Compared to the 3D resin models used for surgical training, how would you rate the superiority of the 3D silicone model? [Ratings range from 1 (Very different) to 5 (Very similar)].

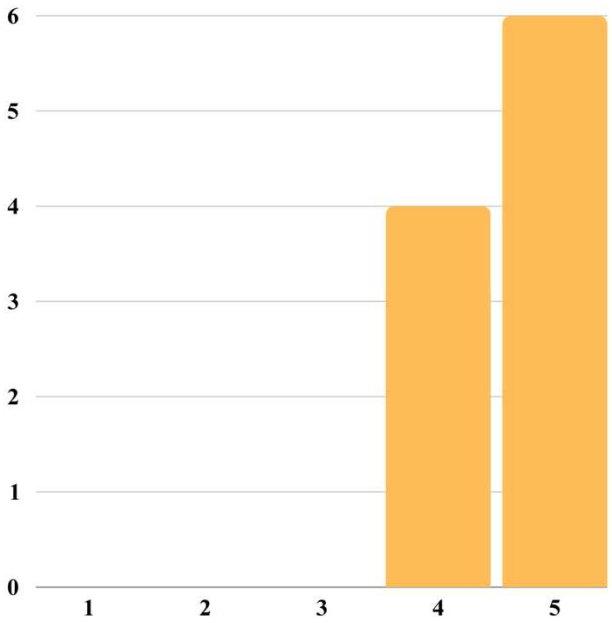

Figure 80 | *Bar chart of comparison between silicone and resin 3D models.*

- What are the things that you would change or improve about this 3D model?

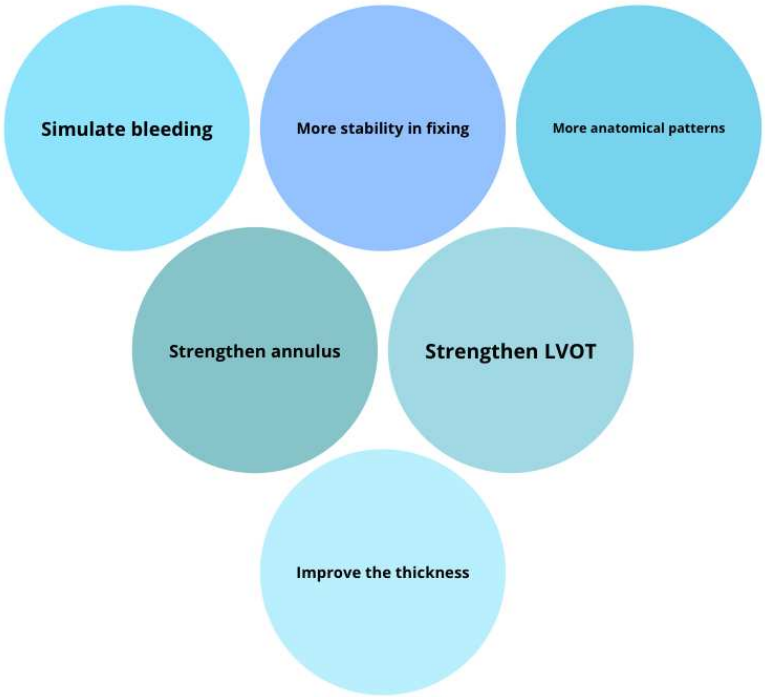

Figure 81 | *Some ideas proposed by surgeons who tested the model.*

V. DISCUSSION

13. Real human anatomy vs 3D silicone model

In this section, we compare the thickness of real human cusps and the ascending aorta with those of prototypes 2 and 3 (both have the same thickness).

The thickness of the cusps of the third 3D silicone prototype measures 1.51 mm.

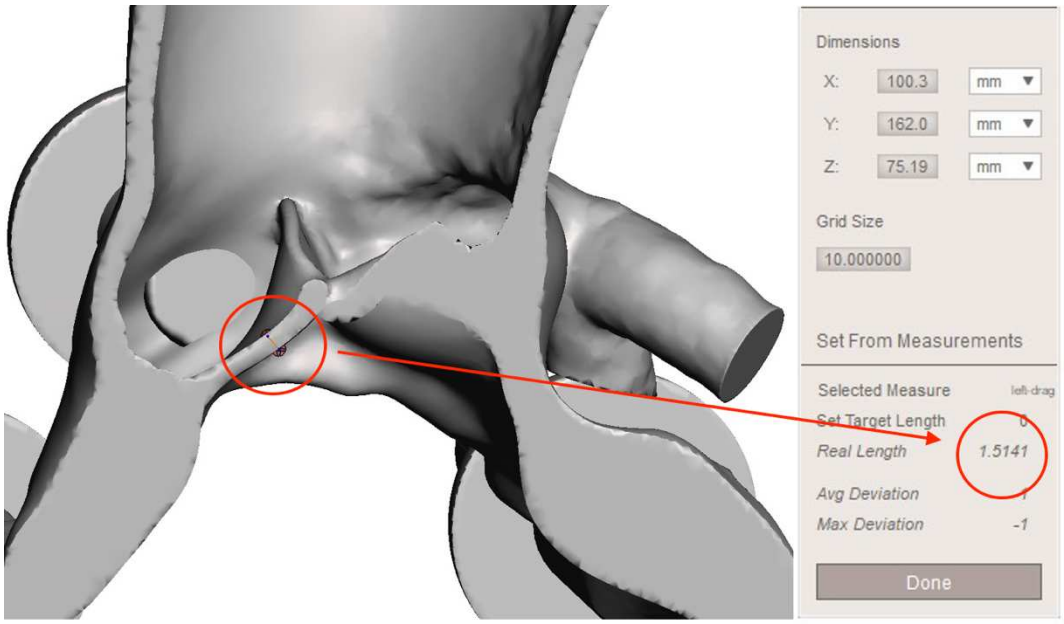

Figure 82 | *3D CAD software screenshot with focus on 3D model cusp thickness.*

The Formlabs™ Form3L™ printer offers a resolution ranging from 25 to 300 µm, meaning that a single layer can theoretically be as thin as 25 µm (~0.025 mm). Like any other manufacturing technique, certain considerations must be made when designing a part to optimize it for 3D printing. Key factors to account for include the part's dimensions relative to the build platform, the intended print orientation and how it might affect mechanical properties (for example, reinforcing features with fillets or chamfers), avoiding unsupported minima, and incorporating drain holes to prevent hollow sections from filling with resin during printing.

Formlabs™ provides recommended dimensions for common geometries based on the use of Clear resin. According to the guidance provided in figure 83, the cusps of the 3D model can be assimilated to a unsupported wall rather than an unsupported overhang, as they are fused together in the model. Consequently, the cusps on the

3D silicone model will also be fused (since the silicone model is an exact cast of the 3D resin model). They can be separated later with a scalpel on the silicone model. However, because this is a model of aortic stenosis, optimal separation of the cusps is not necessary. Therefore, the minimum cusp thickness we can theoretically aim for is 0.6 mm.

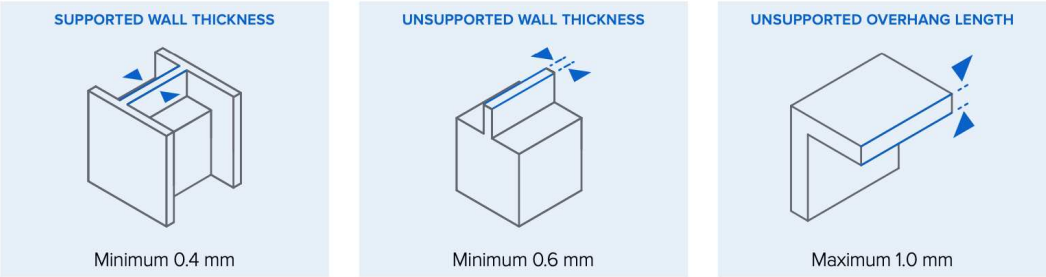

Figure 83 | *Indication of the thicknesses of the Formlabs™ Form3L™ printer.*

Ultrasound micro-imaging produces high-resolution, three-dimensional (3D) images that allow for the distinction of the three histological layers of the cusp: the fibrosa, spongiosa, and ventricularis. However, analyzing the thickness of human cusps is complex for several reasons, including the unknown speed of sound in the sample during ultrasound micro-imaging and the hydration state of the cusps in vivo. Thickness data for aortic valve cusps show substantial variability between studies. For example, Lu et al. (2000)[69] found a mean thickness ranging from 0.57 mm at the tip to 1.20 mm at the base in healthy human specimens using scanning acoustic microscopy. McDonald et al. (2002)[70] analyzed digitized histological slices of normal human aortic valves and reported mean thicknesses ranging from 1.0 mm at the base to about 0.4 mm in the region between the base and the middle of the cusp.

The observed dependence of cusp thickness on the coupling fluid was consistent across several studies, which demonstrated that variations in the mass of the cusp were influenced by fluid exposure. Specifically, exposure to high-concentration dextran solutions decreased the mass of the specimens, while exposure to low-concentration solutions increased tissue mass. These findings indicate that aortic valve cusps readily gain or lose fluid volume by osmosis. Ultrasound images suggest that much of this fluid volume change occurs in the spongiosa. This is likely due to an osmotic gradient caused by the high concentration of glycosaminoglycans (hydrophilic polysaccharides) present in the extracellular matrix of the spongiosa.

Therefore, the hydration level of aortic valve cusps has a significant impact on their mechanical properties[71].

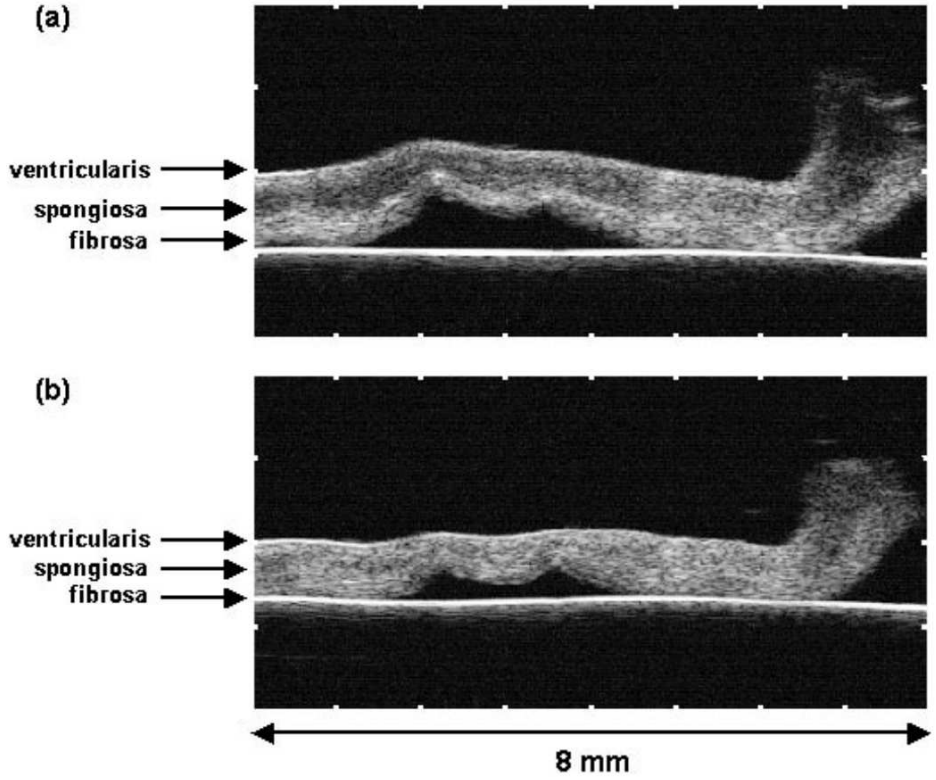

Figure 84 | *Ultrasound images of the same cross-sectional plane through valve: (a) cusp imaged while submerged in distilled water; (b) same cusp imaged after submersion in Hanks physiologic solution. Focus on thickness changes depending on hydration level.*

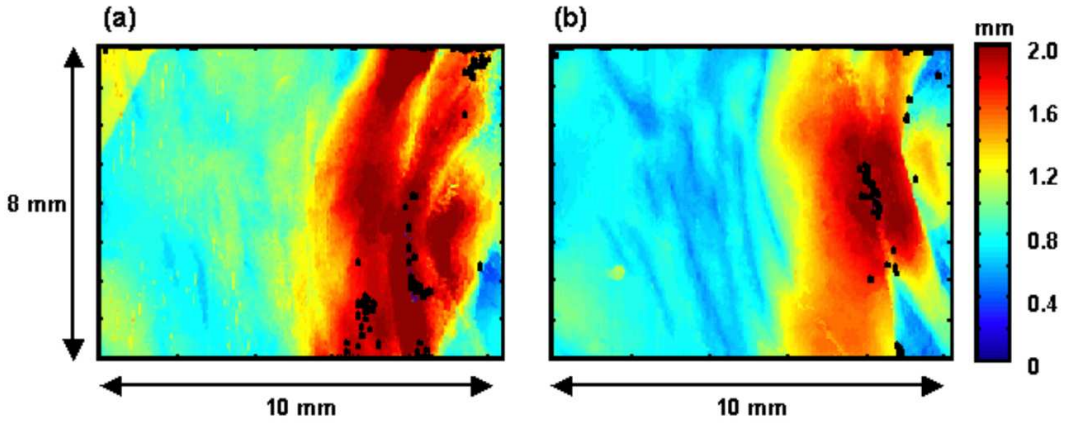

Figure 85 | *Thickness maps estimated from the images of valve. Thickness is displayed on a linear scale ranging from 0 to 2 mm as indicated by the colour bar. Locations of suspect thickness estimates are coloured black. (a) Cusp submerged in distilled water. (b) Same cusp submerged in Hanks physiologic solution.*

The thickness of the cusps tends to increase significantly in aortic stenosis, particularly when the stenosis is caused by calcific degeneration. As illustrated in Figure 86, thicker valve leaflets correspond to a greater degree of valve calcification, confirming the relationship between leaflet thickness and calcification in aortic stenosis. Consequently, our 3D model made of Ecoflex™ silicone is likely to closely resemble the average thickness of pathological cusps[72].

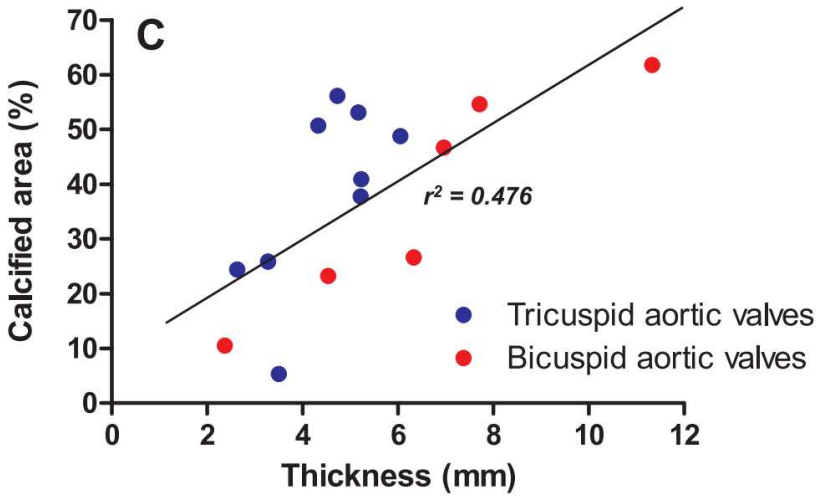

Figure 86 | *Correlation between calcified area and thickness of the aortic valve leaflets[72].*

The thickness of the ascending aorta in Ecoflex™ silicone prototypes measures 2.40 mm.

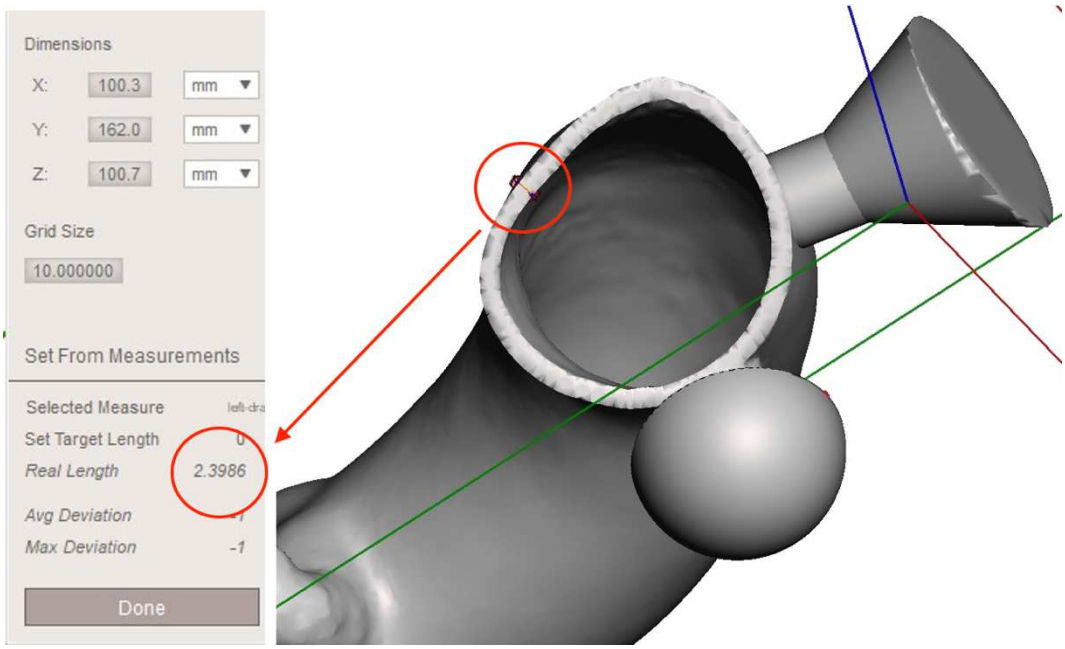

Figure 87 | *3D CAD software screenshot with focus on ascending aorta thickness.*

As illustrated in Figure 88, from the data of the study conducted by Choudhury et al (2009) we note how the thickness of our 3D prototype is in range with the average thicknesses of

the four regions of the healthy ascending aorta[73]. In healthy tissue, the medial quadrant (inner curvature) was significantly thicker than the lateral quadrant (outer curvature). Instead, the thickness of the 3D prototype is the same in all regions of the ascending aorta.

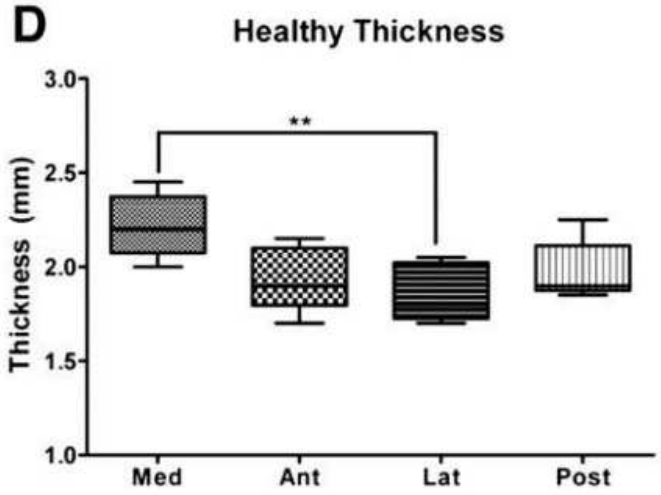

Figure 88 | *Variations in thickness of the healthy ascending aorta[73].*

14. Our experience

During my two years in Prof. Vida's "3D Bioprinting" laboratory, we produced numerous 3D models, not only for the cardiovascular system but also for other organs, commissioned by different medical units. Our museum now features over 50 3D printed models related to the cardiovascular system, a number that reflects the diverse materials and specific versions created for various purposes. The 3D silicone model represents the latest cutting-edge achievement of our team.

Figure 89 | *Section of our 3D museum.*

Regarding surgical training, our team developed a comprehensive program in cardiac and congenital heart surgery, consisting of 12 sessions per year with a total of 40 procedures performed. Two different types of programs were created: a "basic simulation program" for residents in their first and second years of training, and an "advanced simulation program" for surgical residents in their remaining three years. Trainees demonstrated improvements in both time and quality of their performance, with 91% of residents (10 out of 11) showing enhanced surgical quality. The median score from the simulation assessments was significantly higher during the second simulation (83%, IQR: 82-91%) compared to the initial simulation (65%, IQR: 61-70%; $P<0.001$), highlighting a marked improvement in technical performance[59].

Beyond surgical training, another crucial element is surgical planning, which is the process of outlining the necessary steps to correct a specific pathology before surgery. At our center, since 2019, patient-specific 3D models created from CT or MRI scans have been used to enhance surgical planning. These models are typically printed using clear resin and are instrumental in determining the optimal surgical approach. In some cases, instead of printing the model, Virtual Reality (VR) is employed to visualize the anatomy. Both 3D printing and VR technologies assist surgeons in gaining a clearer understanding of the patient's unique anatomy, ultimately improving surgical preparation. For patients undergoing a second surgery, 3D reconstructions are particularly valuable in assessing the relationship between the sternum and critical cardiac structures, such as the right ventricle or great vessels. In these cases, entering the mediastinum through a median sternotomy can be more challenging and hazardous due to scar tissue and adhesions, which can alter the original positioning of underlying structures.

This approach is a vital step towards personalized medicine, a key focus across all research fields today. By producing patient-specific 3D models, even highly experienced surgeons can simulate complex procedures before performing them on the patient. This is especially beneficial for rare congenital heart diseases, which often feature unique anatomical variations. In such cases, rehearsing the procedure on the model helps surgeons familiarize themselves with each step, increasing the likelihood of success and reducing the duration of surgery, which in turn minimizes the risks associated with prolonged cardiopulmonary bypass.

For example, we created a 3D model of a complex case involving Dextro-Transposition of the Great Arteries (D-TGA) with multiple associated defects and double-looping coronary arteries, a rare condition accounting for only 3% of all D-TGA cases[67]. This reconstruction was exceptional because it allowed for a detailed evaluation of coronary artery anomalies using a CT scan. To facilitate preoperative assessment, a 3D model cut to showcase the coronary artery was printed.

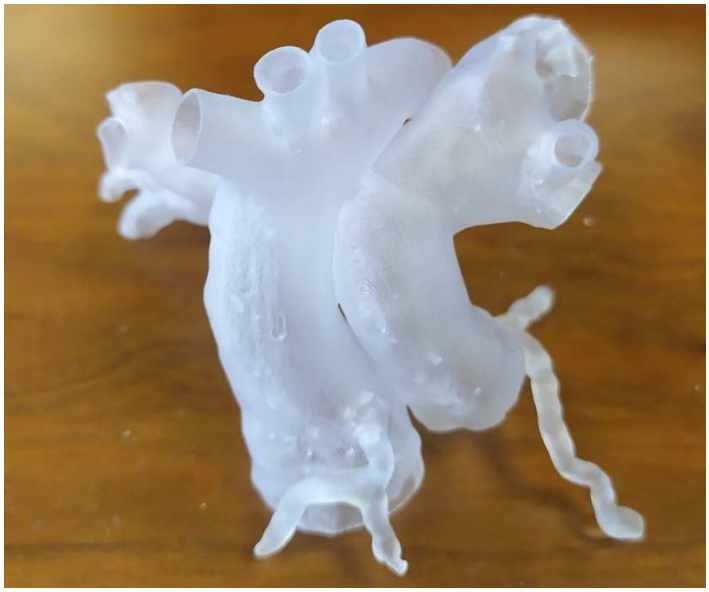

Figure 90 | *Clear Resin™ 3D model of D-TGA with double-looping coronary arteries.*

15. Advantages

In general, 3D printed models serve as valuable tools for pre-operative planning, enhancing patients' understanding of their conditions and strengthening the communication between doctors and patients. They can also function as educational resources, enabling students to study and comprehend anatomy and pathophysiology using models that accurately reflect the actual dimensions and details of real organs and tissues. Moreover, by incorporating enlargements or customized modifications such as openings and incisions, these models facilitate understanding by allowing doctors, patients, or students to visualize internal structures that would otherwise be hidden. During my time in the "3D Bioprinting" laboratory, we produced multiple 3D models designed for these purposes.

The primary benefit of using 3D printed models in a clinical setting as surgical aids lies in their nearly perfect alignment with a patient’s anatomy. Having an accurate

depiction of a patient's internal morphology prior to surgery is invaluable for planning complex procedures. In this context, 3D models created from soft resins provide a notable advantage, as they allow for the simulation of specific interventions on anatomical models that accurately reflect the individual patient's anatomy. Additionally, the opportunity to practice new techniques on these models significantly enhances surgical proficiency. As noted in the previous section, our training program in cardiac and congenital heart surgery within our U.O.C. has demonstrated clear improvements in both the quality of procedures performed and a reduction in surgical times. Furthermore, suturable 3D printed models offer an excellent alternative to traditional animal training methods.

Creating the 3D silicone prototype posed a considerable challenge for our team, as we had never previously worked with this type of model production. In comparison to resin-printed models, silicone prototypes exhibit mechanical properties that more closely resemble human tissue. In fact, in terms of mechanical properties, the evaluation by Illi et al. (2023) demonstrates that the tested Smooth-On silicone blends of Dragon Skin and Ecoflex exhibited elastic moduli comparable to porcine tissues. Moreover, they showed minimal or no compression during unloading, like porcine tissues[74]. This result highlights how silicone blends can accurately replicate the biomechanical behavior of human tissues. Achieving this requires extensive experimentation to determine the correct proportions of each silicone component.

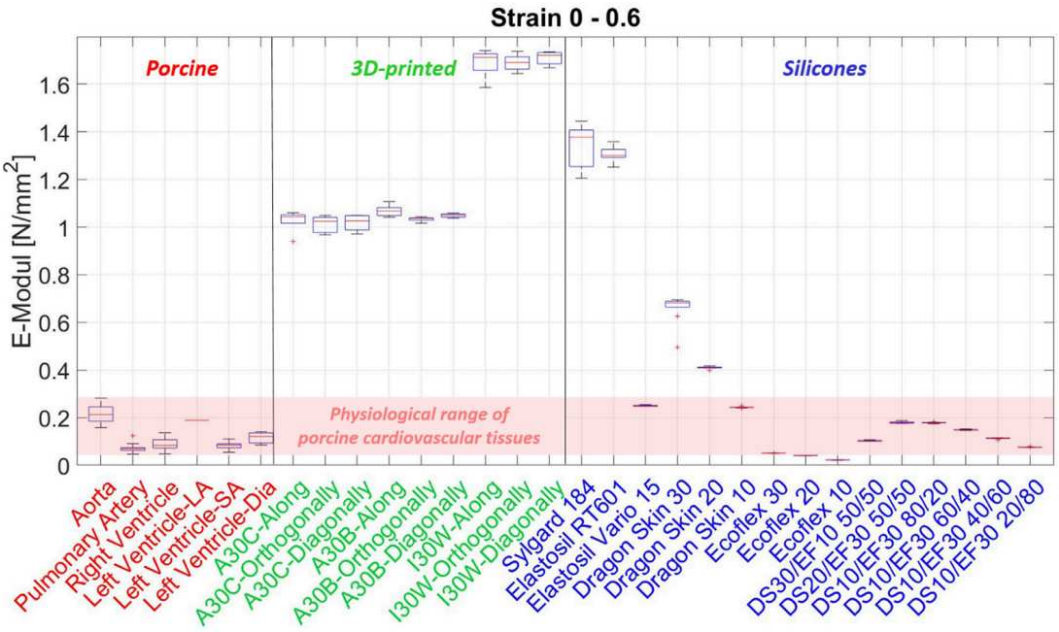

Figure 91 | *Boxplots of all tested materials for the total strain range of 0–0.6 strain*[74].

This is a very important aspect because, until now, our team has focused primarily on achieving an almost perfect correspondence between the 3D model and the patient's anatomy. With this new model, however, we are aiming to achieve a material consistency comparable to that of human tissues. This is particularly significant, as although we have been producing patient-specific 3D models since 2019, the materials we have used so far have been excellent for pre-operative planning and teaching. However, in some cases, the discrepancy between the consistency of human tissue and the resin used for the models has been evident, especially for surgical training.

One of the advantages of silicone models is that, once a mold is created using Mold Star silicone, it can be reused multiple times to produce an unlimited number of models in Ecoflex silicone, significantly lowering production costs.

Moreover, this is a field of research that is continuously growing. In 2021, the global market consumed over 2,900 kilotons of medical elastomers, and demand is expected to grow steadily at a compound annual growth rate of 6.5% from 2022 to 2027 (Mordor Intelligence Inc., 2022). Additionally, the global 3D printing elastomer market reached USD 151 million in 2021 and is expected to grow by 22.5% from 2022 to 2030, reaching USD 1,389 million by 2030 (Report Ocean, 2022). This market research highlights the increasing significance of elastomeric 3D printing for medical applications in the coming years. Therefore, researchers are exploring different techniques to establish functional and reliable AM processes based on elastomers[75]. Furthermore, given the excellent results obtained by different research groups who have created abdominal aortic aneurysm models[76], ascending aorta[77], perineal models[78], meniscus models[79], etc. Another important research that has strongly encouraged us to delve into this field is the additive manufacturing approach for digital fabrication of tissue-like aortic heart valves with customizable geometry and leaflet architectures resembling those of native valve tissue. Using biocompatible silicones with tunable mechanical properties, the heart valves have been fabricated by combining additive manufacturing processes[80]. These are just some of the many medical applications of elastomers. In the future, our research group will focus on improving the current prototype and developing new models using the same method. We are currently working on a silicone mitral valve model, with faithful reproduction of the chordae tendineae.

16. Disadvantages and Limitations

A significant limitation of resin 3D models is the material they are made of. The FormLabs Elastic™ resin we are currently using allows the models to be cut, retracted, and sutured, but its consistency doesn't closely resemble that of cardiac tissues. As a result, even though the model is anatomically precise, the tactile experience for the surgeon during surgery is different from what they would encounter in real life, reducing the fidelity of the simulation.

We are aware of this limitation, and while we believe the primary goal of our simulator is to help surgeons gain a deeper understanding of the steps involved in a procedure, we are actively seeking new materials that better meet our needs. For these reasons, we have begun using elastomers to produce our 3D models. However, it is important to acknowledge that no artificial material currently available can perfectly replicate the physiological properties of tissues within the normal deformation range. Additionally, the mechanical behavior of cardiovascular tissues is heavily influenced by their dynamic nature and inherent mechanical activity. While we can create a mixture of silicones that closely approximates the mechanical properties of human tissues, it will never exactly match them. The silicone 3D model has proven to be a valuable tool for surgical training, but it is still a prototype, and its development is ongoing.

One limitation concerns the production process, which is both complex and time-consuming. Creating a new 3D model can take several hours, depending on the complexity of the anatomy and the quality of the imaging. Once the .stl file is prepared, it must first be printed to ensure there are no inconsistencies in the model. The process of creating the mold from the Mold Star™ silicone model is lengthy, as the silicone must be degassed before being poured into the container, followed by a cross-linking period of about eight to ten hours. Extracting the mold from the container is not easy and splitting it in two with a scalpel is also a delicate task. One of the most challenging steps is removing the resin 3D model from inside the Mold Star™ silicone mold, as the silicone adheres tightly to the resin model, forming an exact cast. This step requires at least two operators and several hours of work.

Furthermore, there is a risk of damaging the Mold Star™ silicone mold when extracting the resin model. For instance, if the scalpel cuts too deeply, it could create

a defect in the silicone mold, which would then also appear in the Ecoflex™ silicone 3D model, as it is an exact replica of the cast. Any imperfection in the Mold Star™ silicone mold will thus be replicated in the Ecoflex™ model. This has been a significant challenge, as we had to remake several molds before achieving one that was free of defects caused during the resin model extraction. Lastly, Ecoflex™ silicone requires an additional ten hours to cure. Altogether, these steps can take several days, if not weeks, to complete, making it difficult to produce more than one model at a time. Each model can only be used for one exercise, so producing enough models for a single session requires a considerable amount of time.

In addition, the varying consistencies of different anatomical structures must be considered. Not all anatomical structures have the same composition; some have a greater fibrous component, while others are more elastic. Thus, using the same material for every structure in a 3D model is not realistic. Currently, the only way we can simulate the differing consistencies of various structures is by adjusting the thickness of certain areas. We can make one region thicker or thinner, but we cannot alter the material composition in specific areas. For example, at "SickKids Hospital" in Toronto, Canada, each part of the heart, including the valvular and subvalvular structures, is produced separately using 3D-printed molds filled with polyvinyl alcohol (PVA), which are then assembled. While this method produces a more realistic texture for the model’s structures.

17. Cost analysis

The first cost to consider is the software for segmentation, anatomical analysis, planning, and design. We used the Mimics inPrint 3.0 software (Materialise NV, Leuven, Belgium) for the reconstruction. There are various licensing plans available, and we chose a three-year plan that costs around 10,000 euros.

The second cost involves the 3D printers and the accessories necessary for their operation. Our Form3L SLA printer from Formlabs (Formlabs, Somerville, USA) has a nominal cost of around 11,000 euros, while our Everes Uno™ DLP printer by Sisma™ costs around 9,000 euros. Additionally, the Anycubic Wash and Cure Plus (HongKong AnyCubic Technology Co., Hong Kong, China), essential during the curing phase as it functions both as a washing machine and polymerization unit,

costs around 250 euros. Printers also have consumable parts that need replacement after a certain number of uses, such as resin tanks.

The cost of resins varies depending on the type: Clear and Grey Resin™ cost approximately 135 euros per liter, Elastic Resin™ costs around 200 euros per liter, and Loctite 3D IND475™ costs around 200 euros per liter. The cost of silicones is about 40 euros per liter for Smooth-On Mold™ Star and around 42 euros per liter for Smooth-On Ecoflex™.

Additionally, producing silicone 3D models requires considering the cost of containers to hold the mold, as well as a vacuum chamber and pump to degas the silicone. We opted for a Bacoeng vacuum chamber™ with a pump, which cost around 300 euros.

To create a single 3D silicone model, approximately 180 mL of Clear or Grey Resin™, 1,800 mL of Smooth-On Mold Star™, and 220 mL of Smooth-On Ecoflex™ are needed, resulting in a total cost of 106 euros. The advantage is that the same mold can be reused to produce multiple models, meaning the cost for each subsequent model will be only around 9 euros.

VI. CONCLUSIONS

The creation of this silicone 3D prototype signifies the peak of our expertise in the realm of 3D printing. It offers trainees an innovative and affordable educational resource that effectively supports the extensive training necessary to develop the skills of a cardiac surgeon. With its low production cost and closer resemblance to human tissue, this model is far more realistic than earlier resin 3D models. Additionally, the capability to produce patient-specific models has proven advantageous for experienced surgeons during surgical procedures. This silicone model serves as a foundation for utilizing new innovative materials and advanced techniques in our "3D Bioprinting" laboratory.

Bibliography

1. Anatomia Umana. Volume 1: Atlante / G. Anastasi, P. Castano, S. Castorina, O. Cremona, R. De Caro, E. Gaudio, G. Macchiarelli, M. Rende, D. Ribatti, C. Sforza, C. Tacchetti; [a cura di] G. Anastasi, C. Tacchetti. - Milano: Edi.Ermes, 2013. - ISBN 9788870513486.

2. Tao, G.; Kotick, J.D.; Lincoln, J. Heart valve development, maintenance, and disease: The role of endothelial cells. Curr. Top. Dev. Biol. 2012, 100, 203–232.

3. Hinton, R.B.; Lincoln, J.; Deutsch, G.H.; Osinska, H.; Manning, P.B.; Benson, D.W.; Yutzey, K.E. Extracellular Matrix Remodeling and Organization in Developing and Diseased Aortic Valves. Circ. Res. 2006, 98, 1431–1438. [CrossRef]

4. Stella J.A., Michael S. Sacks M.S. On the Biaxial Mechanical Properties of the Layers of the Aortic Valve leaflet J. Biomech. 2007, Vol. 129; DOI: 10.1115/1.2768111

5. Hinton, R.B.; Yutzey, K.E. Heart Valve Structure and Function in Development and Disease. Annu. Rev. Physiol. 2011, 73, 29–46. [CrossRef]

6. Aikawa, E. Calcific Aortic Valve Disease; IntechOpen: London, UK, 2013.

7. Karthik M. Kodigepalli, Kaitlyn Thatcher, Toni West, Daniel P. Howsmon, et al. Biology and Biomechanics of the Heart Valve Extracellular Matrix. J. Cardiovasc. Dev. Dis. 2020, 7, 57; doi: 10.3390/jcdd7040057

8. Hsu C.D., Hutcheson J.D., Ramaswamy S. Oscillatory Fluid-Induced Mechanobiology in Heart Valves with Parallels to the Vasculature. Vascular Biology. February 2020. DOI:10.1530/VB-19-0031

9. Buchanan, R.M.; Sacks, M.S. Interlayer micromechanics of the aortic heart valve leaflet. Biomech. Model. Mechanobiol. 2013, 13, 813–826. [CrossRef] [PubMed]

10. Rego, B.V.; Sacks, M.S. A functionally graded material model for the transmural stress distribution of the aortic valve leaflet. J. Biomech. 2017, 54, 88–95. [CrossRef]

11. Rabkin, E.; Aikawa, M.; Stone, J.R.; Fukumoto, Y.; Libby, P.; Schoen, F.J. Activated Interstitial Myofibroblasts Express Catabolic Enzymes and Mediate Matrix Remodeling in Myxomatous Heart Valves. Circulation 2001, 104, 2525–2532. [CrossRef]

12. Rabkin-Aikawa, E.; Farber, M.; Aikawa, M.; Schoen, F.J. Dynamic and reversible changes of interstitial cell phenotype during remodeling of cardiac valves. J. Heart Valve Dis. 2004, 13, 841–847. [PubMed]

13. Helske-Suihko, S.; Kupari, M.; Lindstedt, K.A.; Kovanen, P.T. Aortic valve stenosis: An active atheroinflammatory process. Curr. Opin. Lipidol. 2007, 18, 483–491. [CrossRef]

14. Anstine, L.J.; Bobba, C.; Ghadiali, S.N.; Lincoln, J. Growth and maturation of heart valves leads to changes in endothelial cell distribution, impaired function, decreased metabolism and reduced cell proliferation. J. Mol. Cell. Cardiol. 2016, 100, 72–82. [CrossRef] [PubMed]

15. Sacks, M.S.; Merryman, W.D.; Schmidt, D.E. On the biomechanics of heart valve function. J. Biomech. 2009, 42, 1804–1824. [CrossRef] [PubMed]

16. Dutta, P.; Lincoln, J. Calcific Aortic Valve Disease: A Developmental Biology Perspective. Curr. Cardiol. Rep. 2018, 20, 21. [CrossRef] [PubMed]

17. Coffey, S.; Harper, A.R.; Cairns, B.J.; Roberts, I.S.; Prendergast, B. Clinical information has low sensitivity forpostmortem diagnosis of heart valve disease. Heart 2017, 103, 1031–1035. [CrossRef] [PubMed]

18. Yadgir, S.; Johnson, C.O.; Aboyans, V.; Adebayo, O.M.; Adedoyin, R.A.; Afarideh, M.; Alahdab, F.; Alashi, A.; Alipour, V.; Arabloo, J.; et al. Global, Regional, and National Burden of Calcific Aortic Valve and Degenerative Mitral Valve Diseases, 1990–2017. Circulation 2020, 141, 1670–1680. [CrossRef]

19. Iung B, Vahanian A. Epidemiology of valvular heart disease in the adult. Nat Rev Cardiol 2011;8:162-72.

20. Marangou, J.; Beaton, A.; Aliku, T.O.; Nunes, M.C.P.; Kangaharan, N.; Reményi, B. Echocardiography in Indigenous Populations and Resource Poor Settings. Heart Lung Circ. 2019, 28, 1427–1435. [CrossRef] [PubMed]

21. Roth, G. A. et al. Global burden of cardiovascular diseases and risk factors, 1990–2019. J. Am. Coll. Cardiol. 76, 2982–3021 (2020).

22. Chang AS, Smedira NG, Chang CL, et al. Cardiac surgery after medi- astinal radiation: extent of exposure influences outcome. J Thorac Car- diovasc Surg 2007; 133:404-13.

23. Bhattacharyya S, Schapira AH, Mikhailidis DP, Davar J. Drug-induced fibrotic valvular heart disease. Lancet 2009; 374:577-85.

24. AHA, Heart Disease and Stroke Statistics—2003 update, 2002, American Heart Association, Dallas, TX.

25. Iung B, Baron G, Butchart EG, et al. A prospective survey of patients with valvular heart disease in Europe: The Euro Heart Survey on Valvular Heart Disease. Eur Heart J 2003; 24:1231-43.

26. Iung B, Baron G, Tornos P, et al. Valvular heart disease in the community: a European experience. Curr Probl Cardiol 2007; 32:609-61.

27. Nkomo VT, Gardin JM, Skelton TN, et al. Burden of valvular heart diseases: a population-based study. Lancet 2006; 368:1005-11

28. Merryman, W.D.; Youn, I.; Lukoff, H.D.; Krueger, P.M.; Guilak, F.; Hopkins, R.A.; Sacks, M.S. Correlation between heart valve interstitial cell stiffness and transvalvular pressure: Implications for collagen biosynthesis. Am. J. Physiol. Circ. Physiol. 2006, 290, H224–H231. [CrossRef]

29. Tao, G.; Kotick, J.D.; Lincoln, J. Heart valve development, maintenance, and disease: The role of endothelial cells. Curr. Top. Dev. Biol. 2012, 100, 203–232.

30. Tibazarwa KB, Volmink JA, Mayosi BM. Incidence of acute rheumatic fever in the world: a systematic review of population-based studies. Heart 2008; 94:1534-40.

31. Rizvi SF, Khan MA, Kundi A, et al. Status of rheumatic heart disease in rural Pakistan. Heart 2004; 90:394-9.

32. Carapetis JR. Rheumatic heart disease in Asia. Circulation 2008;118: 2748-53.

33. Iliceto, Sabino e Razzolini, Renato. Manuale di Cardiologia, s.l., Piccin – Nuova libraria, 2019 - ISBN 9788829929740

34. Otto CM: Calcific aortic stenosis - time to look more closely at the valve. New Engl J Med 359:1395, 2008.

35. Vahanian A. et al. 2021 ESC/EACTS Guidelines for the management of valvular heart disease: Developed by the Task Force for the management of valvular heart disease of the European Society of Cardiology (ESC) and the European Association for Cardio-Thoracic Surgery (EACTS). European Heart Journal, Volume 43, Issue 7, 14 February 2022, Pages 561–632, https://doi.org/10.1093/eurheartj/ehab395

36. Monin JL, Lancellotti P, Monchi M et al.: Risk score for predicting outcome in patients with asymptomatic aortic stenosis. Circulation 120:69, 2009.

37. Rosenhek R, Zilberszac R, Schemper M et al.: Natural history of very severe aortic stenosis. Circulation 121:151,2010.

38. lung B, Delgado V, Rosenhek R, Price S, Prendergast B, Wendler O, De Bonis M, Tribouilloy C, Evangelista A, Bogachev-Prokophiev A, Apor A, Ince H, Laroche C Popescu BA, Pierard L, Haude M, Hindricks G, Ruschitzka F, Windecker S, Bax J, Maggioni A, Vahanian A, EORP VHD II Investigators. Contemporary presentation and management of valvular heart disease: The EURObservational Research Programme Valvular Heart Disease Il Survey. Circulation 2019;140:1156 -1169.

39. Sambola A, Tornos P, Ferreira-Gonzalez I, Evangelista A: Prognostic value of preoperative indexed end systolic left ventricle diameter in the outcome after surgery in patients with chronic aortic regurgitation.

40. Otto CM, Bonow RO: Valvular heart disease. Elsevier, Philadelphia, 2014.

41. Weyman AF: Assessment of mitral stenosis. Role of real-time 3D-TEE. J Am Coll Cardiol Img 4:589, 2011

42. Enriquez-Sarano M, Akins CW, Vahanian A: Mitral regurgitation. Lancet 373:1382, 2009.

43. Enriquez-Sarano M, Loulmet DE, Burkhoff D: The 3conundrum of functional mitral regurgitation in chronic heart failure. J Am Coll Cardiol 51:187, 2008

44. Carabello-BA: The current therapy for mitral regurgitation. J Am Coll Cardiol 52:319, 2008.

45. Gaasch WH, Meyer TE: Left ventricular response to mitral regurgitation. Implications for management. Circulation118:2298, 2008.

46. Donald B. Doty, John R. Doty. Cardiac Surgery: Operative Technique, Saunders, 2° edizione (24 maggio 2012) – ISBN 978-1416036531

47. Zachow S, Zilske M, Hege HC. Konrad-Zuse-Zentrum für Informationstechnik Berlin ZIB-Report 07-41 (Dezember 2007) 3D reconstruction of individual anatomy from medical image data: Segmentation and geometry processing. 2007.

48. Sato T, Takagi T. Validation of the influence of CT slice thickness on the quantitative accuracy and image quality of single photon emission computed tomography. Asia Ocean J Nucl Med Biol. 2021;9(2):148. doi: 10.22038/aojnmb.2021.57698.1432

49. Nashwan K. A., Shereen I. H. et al. Investigating the slice thickness effect on noise and diagnostic content of single-source multi-slice computerized axial tomography. J Med Life. 2023 Jun;16(6):862-867. doi: 10.25122/jml-2022-0188.

50. Monnin P, Vallecilla C, Baisero A. Optimal slice thickness for object detection with longitudinal partial volume effects in computed tomography. J Appl Clin Med Phys. 2017;18(1):251-259. doi: 10.1002/acm2.12041

51. Lasiyah N, Ng KH, Ng KH. Automated procedure for slice thickness verification of computed tomography images: Variations of slice thickness, position from iso-center, and reconstruction filter. J Appl Clin Med Phys. 2021;22(7):313-321. doi: 10.1002/ acm2.13330

52. Mühler M, Nitschke M, Schulz R, Reisinger W, Wirth S. The influence of slice thickness on assessment of clavicle ossification in forensic age diagnostics. Int J Legal Med. 2006;120(1):15-17. doi: 10.1007/s00414-005-0016-3

53. Petzold R, Zeilhofer HF, Kalender WA. Rapid protyping technology in medicine--basics and applications. Comput Med Imaging Graph [Internet]. 1999 Oct; 23(5):277–84.

54. He W, Tian K, Xie X, Wang X, Li Y, Wang X, et al. Individualized Surgical Templates and Titanium Microplates for le Fort i Osteotomy by Computer-Aided Design and Computer-Aided Manufacturing. Journal of Craniofacial Surgery. 2015 Sep 1;26(6):1877–81.

55. From B. Derby, "Printing and prototyping of tissues and scaffolds," Science (New York, N.Y.), vol. 338, no. 6109, pp. 921–926, Nov. 2012, doi: 10.1126/SCIENCE.1226340

56. Lasiyah N, Ng KH, Ng KH. Automated procedure for slice thickness verification of computed tomography images: Variations of slice thickness, position from iso-center, and reconstruction filter. J Appl Clin Med Phys. 2021;22(7):313-321. doi: 10.1002/ acm2.13330

57. Mühler M, Nitschke M, Schulz R, Reisinger W, Wirth S. The influence of slice thickness on assessment of clavicle ossification in forensic age diagnostics. Int J Legal Med. 2006;120(1):15-17. doi: 10.1007/s00414-005-0016-3

58. Sekhar A, Sun MR, Siewert B. A tissue phantom model for training residents in ultrasound-guided liver biopsy. Acad Radiol. 2014

59. Cattapan C., Guariento A., Bertelli F., Galliotto F., Vazzoler C., Magagna P., Gerosa G. and Vida V. The introduction of surgical simulation on three-dimensional- printed models in the cardiac surgery curriculum: an experimental project. J Cardiovasc Med 2024, 25:165–172. DOI:10.2459/JCM.0000000000001577

60. Müller-Stich BP, Löb N, Wald D, Bruckner T, Meinzer H-P, Kadmon M, Büchler MW, Fischer L. Regular three-dimensional presentations improve in the

identification of surgical liver anatomy - a randomized study. BMC Med Educ. 2013; 13:131. doi:10.1186/1472-6920-13-131

61. Goo HW, Park SJ, Yoo SJ. Advanced Medical Use of Three-Dimensional Imaging in Congenital Heart Disease: Augmented Reality, Mixed Reality, Virtual Reality, and Three-Dimensional Printing. Korean J Radiol. 2020;21(2):133-145. doi:10.3348/kjr.2019.0625

62. Kusaka M, Sugimoto M, Fukami N, Sasaki H, Takenaka M, Anraku T et al. Initial experience with a tailor-made simulation and navigation program using a 3-D printer model of kidney transplantation surgery. Transplant Proc 2015; 47:596–9.

63. Ravi P., Chepelev L. et al. A systematic evaluation of medical 3D printing accuracy of multi-pathological anatomical models for surgical planning manufactured in elastic and rigid material using desktop inverted vat photopolymerization. Med Phys. 2021 Jun;48(6):3223-3233. doi: 10.1002/mp.14850.

64. P. J. Flory, Principles of Polymer Chemistry (Cornell Univ. Press, 1953).

65. M. Morton, Rubber Technology (Springer, 2013).

66. Hunt MF, Zhou X, Lui C, Yang SC. Educational research and training innovation in cardiothoracic surgery: a year in review. J Thorac Cardiovasc Surg 2019; 157:1722 – 1727.

67. Selke F, del Nido PJ, Swanson SJ. Sabiston and Spencer Surgery of the Chest, 9th Edition. 9th ed. (Elsevier, ed.).; 2015.

68. James C Lacefield et al. Three-dimensional visualization and thickness estimation of aortic valve cusps using highfrequency ultrasound. 2004 Physiol. Meas. 25 27. DOI: 10.1088/0967-3334/25/1/003

69. Lu X, Senda S, Mitzushige K, Masugata H, Sakamoto S and Matsuo H 2000 Evaluation of progression in nonrheumatic aortic valvular stenosis by scanning acoustic microscopy Ultrasound Med. Biol. 26 563–9

70. McDonald P C, Wilson J E, McNeill S, Gao M, Spinelli J J, Rosenberg F, Wiebe H and McManus B M 2002 The challenge of defining normality for human mitral and aortic valves: geometrical and compositional analysis Cardiovasc. Pathol. 11 193–209

71. Talman E A and Boughner D R 2001 Effect of altered hydration on the internal shear properties of porcine aortic valve cusps Ann. Thorac. Surg. 71 S375–8

72. Cheng C.L. et al. Ex vivo assessment of valve thickness/calcification of patients with calcific aortic stenosis in relation to in vivo clinical outcomes. J Mech Behav

Biomed Mater. 2017 Oct: 74:324-332. doi: 10.1016/j.jmbbm.2017.06.020. Epub 2017 Jun 22

73. Choudhury N. et al. Local mechanical and structural properties of healthy and diseased human ascending aorta tissue. Cardiovasc Pathol. 2009 Mar-Apr;18(2):83-91. doi: 10.1016/j.carpath.2008.01.001. Epub 2008 Mar 5.

74. Illi J. et al. Mechanical testing and comparison of porcine tissue, silicones and 3D-printed materials for cardiovascular phantoms. Front Bioeng Biotechnol. 2023 Dec 1:11:1274673. doi: 10.3389/fbioe.2023.1274673. eCollection 2023.

75. From B. Derby, "Printing and prototyping of tissues and scaffolds," Science (New York, N.Y.), vol. 338, no. 6109, pp. 921–926, Nov. 2012, doi: 10.1126/SCIENCE.1226340"

76. B. J. Doyle, 3D Reconstruction and Manufacture of Real Abdominal Aortic Aneurysms: From CT Scan to Silicone Model. J Biomech Eng. Jun 2008, 130(3): 034501. https://doi.org/10.1115/1.2907765

77. Alakhtar A, et al. BMJ Simul Technol Enhanc Learn 2021;7:536–542. doi:10.1136/bmjstel-2021-000868

78. Goudie C., Shanahan J. et al. Investigating the Efficacy of Anatomical Silicone Models Developed from a 3D Printed Mold for Perineal Repair Suturing Simulation. Cureus. 2018 Aug; 10(8): e3181. doi: 10.7759/cureus.3181

79. Luis E., Pan H.M. et al. 3D Printed Silicone Meniscus Implants: Influence of the 3D Printing Process on Properties of Silicone Implants. Polymers 2020, 12(9), 2136; https://doi.org/10.3390/polym12092136

80. Fergal B. Coulter et al. Bioinspired Heart Valve Prosthesis Made by Silicone Additive Manufacturing. Matter 1, 266–279, July 10, 2019. Elsevier Inc. https://doi.org/10.1016/j.matt.2019.05.013